Université de Toulouse

THÈSE

En vue de l'obtention du

DOCTORAT DE L'UNIVERSITÉ DE TOULOUSE

Délivré par *l'Université Toulouse III - Paul Sabatier*
Discipline ou spécialité : *Systèmes Automatiques*

Présentée et soutenue par *Bogdan ROBU*
Le *03.12.2010*

Titre :

Active vibration control of a fluid/plate system

JURY
M. Jean-Pierre RAYMOND, President
M. Miroslav KRSTIC, Rapporteur
M. Yann LE GORREC, Rapporteur
Mme. Lucie BAUDOUIN, Membre
M. Gildas BESANCON, Membre
Mme. Valérie BUDINGER, Membre
M. Edouard LAROCHE, Membre
M. Christophe PRIEUR, Membre

Ecole doctorale : *EdSYS*
Unité de recherche : *LAAS - CNRS*
Directeur(s) de Thèse : *M. Christophe PRIEUR, Directeur de thèse*
Mme. Lucie BAUDOUIN, Co-Directeur de thèse
Rapporteurs : *M. KRSTIC and Y. LE GORREC*

"Răbdare, răbdare, răbdare, răbdare, răbdare ...
răbdare, răbdare, răbdare, răbdare ....."
Arhim. Ilie CLEOPA

"That which does not kill you
makes you stronger."
Friedrich Nietzsche

Acknowledgments

I would first like to express my gratitude towards my advisors Mme. Lucie Baudouin et M. Christophe Prieur for their help and constant encouragement throughout these years. They provided me with freedom and support to pursue my research ideas and I am grateful I had the chance to benefit from their experience. Thank you especially for the motivation notes during the writing of the final part of the thesis.

I also like to express my thanks to M. Miroslav Krstic and M. Yann Le Gorrec for making me the honor to review my thesis and for giving me useful comments for improving it's quality. I equally thank to M. Jean-Pierre Raymond for accepting to be the president of my thesis committee. My thanks also go towards Mme. Valérie Budinger for the great help with the experimental setup and for accepting to be a member of my thesis committee. I also thank to M. Gildas Besançon and M. Edouard Laroche for their participation in my thesis committee and for their useful comments.

I also want to thank to Mme. Isabelle Queinnec, head of the MAC group, for welcoming me here at LAAS-CNRS. My gratitude goes also towards M. Denis Arzelier for guiding me during the master project and for allowing me to benefit from his experience during my thesis. I also wish to thank to all the members of the MAC group, my education has been enhanced because of your advices and presence.

I would also like to thank to all my friends, to the ones that are still next to me and to the ones that are far away. I'm glad that you entered my life, it's been a wonderful growing experience. I learned many things from each and any one of you ... I just hope that I learned all the things I had to.

A special thanks to all my high school friends. Thank you very much guys for all your help and support in the difficult moments, I could not done it without you. Thank you that after all these years we can still get together and have a great time.

Finally, my deepest and sincere thanks go to my parents and especially to my brother Cos. The best brother and the best parents that could ever exist. Thank you for always being here for me - I apologize for the times that I was not there for you. I am glad I have you and I love you very much. This thesis is dedicated to you !!!

Contents

List of Figures

List of Tables

Introduction

General context

The new generation of airplanes and space shuttles need to fly further and further away. Thus, the problem of fuel capacity has come to the attention of the scientific world. In accordance, the tanks used to stock the fuel need to be enlarged. The drawback is that larger quantities of fuel imply that a potentially larger quantity of liquid can be subject to movements if necessary preventive measures are not taken. Therefore, the question of controlling the liquid behavior has arisen and NASA started from the early '60s to concentrate on this issue. The first complete study was done by Abramson [2], based on many other studies dealing with this issue as [22], [34], [92] just to cite few of many.

The core problem with large quantities of liquid in large tanks is that, a phenomenon of sloshing occurs at low frequency. As the sloshing frequencies get lower, an interference with the control frequencies generated by pilots may occur. This may lead to a continuous excitation of the liquid which, in return, will affect the vehicle stability. Besides, this can even lead to the non-controllability and destruction of the vehicle [48]. Even if such extreme cases are not willing to occur, the liquid strange behavior can still pose serious problems [46]. As an example, [3] and [129] give a lists of airplanes that were confronted to this issue during the testing phase: Douglas A4D, Lockhead P-80, Boeing KC-135, Cessna T-37, North American YF-100. Moreover, liquid unpredictable movement also affected the NEAR spacecraft which had to interrupt his insertion burn due to large fuel reactions. Even though the fuel was finally controlled, the mission was still delayed for almost a year [138].

In order to minimize the sloshing, various methods can be used. Firstly, the containers with liquid can be divided, using baffles, in several smaller containers so that the eigenfrequencies of the sloshing modes are increased [124], [130]. Secondly, since the location of the containers also affects the damping of the structure [20], better positioning can be found. Thirdly, the use of light elements to partially cover

the liquid free surface can also increase the natural sloshing frequencies [20]. Fourthly, a control system can also be carefully chosen so that sloshing modes are attenuated or at least not excited too much. We will concentrate our work on this last method.

In order to control the sloshing, one needs to compute for each mode the natural frequency, the mode shape and then the total forces and moment that it generates. Exact solutions though, are possible only for very few special cases, such as vertical cylindrical tank or a rectangular tank [67]. Furthermore, in the case when the exact solutions exist, the coupling between these solutions and the equations of fluid motion is too computationally demanding even with super computers [48]. Based on these remarks, some approximations of the liquid sloshing have to be found. As presented in [18], a good approximation is obtained by considering each sloshing mode as a system with a single degree of freedom and representing it either as a mass-pendulum system or a spring-mass system. Even though both methods are equivalent [67], the mass-pendulum system is usually preferred due to some small advantages (his natural frequency varies with the changes in axial acceleration as the sloshing frequency does [48]). Finally, the oscillating fluid can be represented as a simple mechanical system, in which the location and the magnitude of the model variables are determined to give the same forces and moments as the liquid does.

Another characteristic of airplanes and space shuttles of the future is the increase of their size. As they become larger, in order to reduce the overall weight, the wings and tail definitely need to be lighter, thus more flexible. See [13] for the Airbus A-380 case or [137] for the NASA Active Aeroelastic Wing (AAW) concept. The study of flexible structures has captured the attention of researchers for many years and is well covered in the literature. As an example, one can check the works of [30] or [56] where the theory is presented and experimental results are given.

It is well known that, especially in the case of large airplanes, a great part of the fuel is concentrated in the wings. Thus, for some airplanes, the quantity of fuel carried in the wing tanks becomes a large percentage of the total wing mass [92]. Thus, the wing will be considerably influenced by the liquid movements.

On the other hand, due to their characteristics, smart materials have been used for many years now, especially in the field of civil engineering, for measuring and attenuating the deformations of structures [29]. Therefore, the question of how it can be useful to use them for controlling the flexible devices arose. Since the first results were promising, nowadays, the piezoelectric patches are very much used to

suppress the vibration of structures [11], [23], [45], [65], [66], [144]. However, up to our knowledge, only few works have addressed the coupling between liquid sloshing and flexible structure [79], [132]. Moreover, even fewer consider this coupling in the case of airplanes [108], [109].

The device we are working on follows these lines, the purpose being to control, using piezoelectric patches, a flexible plate connected to a tank filled with liquid. Furthermore, this device was constructed to have, in low frequency domain, the same behavior as a real plane wing [110].

Thesis outline

The manuscript is constructed as follows.

The first chapter gives a detailed presentation of the experimental device we want to model and control: a rectangular plate clamped at one of its ends, connected to a cylindrical tank at its other end. After a geometric characterization of the structure, the acquisition system is detailed and analyzed. The final part of the chapter concentrates on the presentation of actuator and sensor patches. Since they are made from piezoelectric materials, a brief description of the piezoelectric phenomenon is first given. Then, some details are given on the optimal placement of these patches. Finally, the actuator speed and his influence on the total dynamic of the system is analyzed.

Chapter 2 gathers the steps of the mathematical modeling of the device and details the computation of the structure model. Even though numerical methods are the most employed for the model computation of complex structures like ours, we choose to work with an analytical procedure. It will lead to a more tedious modeling phase, but, taking into account many mechanical considerations will show its interest during the controller computation phase. The main idea we follow for the computation of the model is first to get two separate partial differential equation (PDE) models, one for the plate and one for the tank with liquid, and second to put them together by studying the mutual influence. Thus, the model is first written using PDEs and then is approximated using the Ritz method for the plate and using mechanical analogue systems for the sloshing. Finally, the finite dimensional system is written under the shape of a state-space representation.

In Chapter 3 the theoretical bases of the Chapter 4 are set. Since the controllers we compute are based on the finite dimensional model, the issue of choosing the suitable amount of modes for the model approximation needs to be tackled. A method based on the energetic contribution of each structure mode solves this issue. Then, the theory to compute a pole placement controller coupled with a full state observer is briefly reminded. Finally, the frame of robust H_∞ control is briefly presented and more attention is given to the particularities of the method implementation in the case of infinite dimension systems.

The core problem of controlling the experimental device is treated in Chapter 4. After testing the influence of actuator dynamics, the issue of choosing the right amount of modes for the model approximation is considered. Based on technical considerations of airplanes and on the energetic contribution of each mode, a choice of the number of modes to be considered is made. Numerical simulations and experimental tests are conducted afterward. First, a pole placement controller is computed and tested. Second, a H_∞ controller, robust to external perturbations, is computed. Using the HIFOO package, reduced order controllers can also be found. Moreover, the simultaneous control problem with reduced order controllers is also considered. Simulations and tests are shown and analyzed.

The manuscript ends with a last chapter dealing with the conclusions of this work and with perspectives for further research.

Each chapter (except for the last chapter which presents the general conclusions of the manuscript) ends with a short conclusion dealing with the contribution of the chapter and its connection with the forthcoming one.

Chapter 1

Experimental device presentation

This chapter is devoted to the description of the experimental device we are working on. It is located at l'Institut Supérieur de l'Aéronautique et de l'Espace - École Nationale Supérieure d'Ingénieurs de Constructions Aéronautiques (ISAE - ENSICA) in Toulouse, France. The device is pictured in Figure 1.1 and it has been constructed to have the same behavior, in low frequencies, as a real plane wing with fuel (see [110] or [114]).

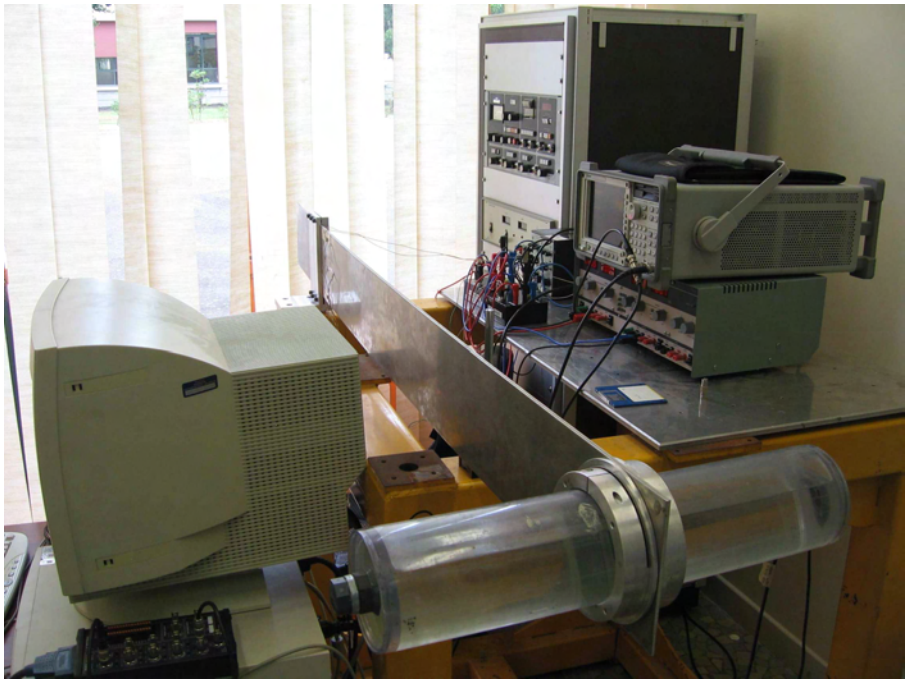

Figure 1.1: Experimental device ISAE-ENSICA

1.1 Characteristics of the experimental device

The experimental device is composed of an aluminum plate and a plexiglas tip-tank filled with liquid. The plate is rectangular, clamped at one side and free on the other three sides. At the free end of the plate, opposite to the clamped end, is connected the cylindrical tank, as it can be seen on Figures 1.2 and 1.3. The tank is in a horizontal position and it can be filled with water or ice up to an arbitrary level.

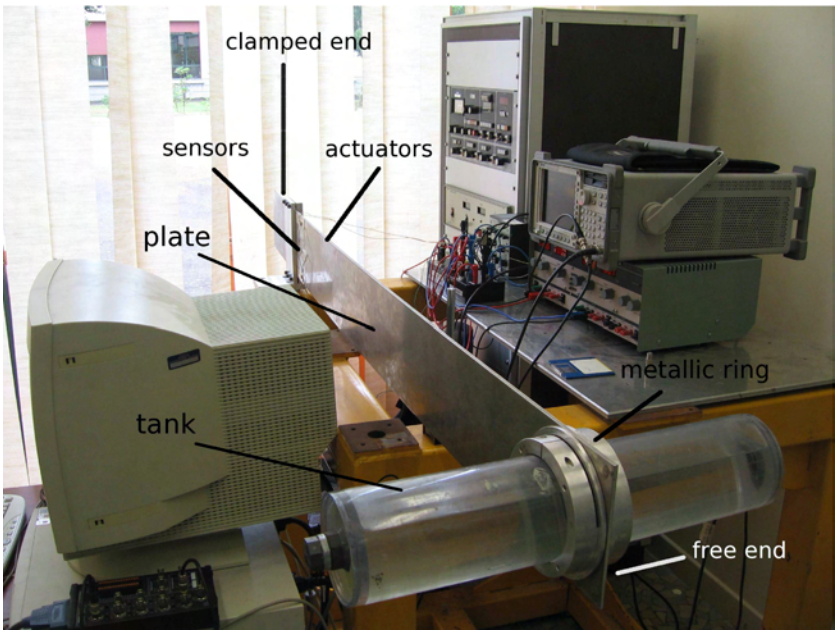

Figure 1.2: Experimental device, detailed presentation of main components

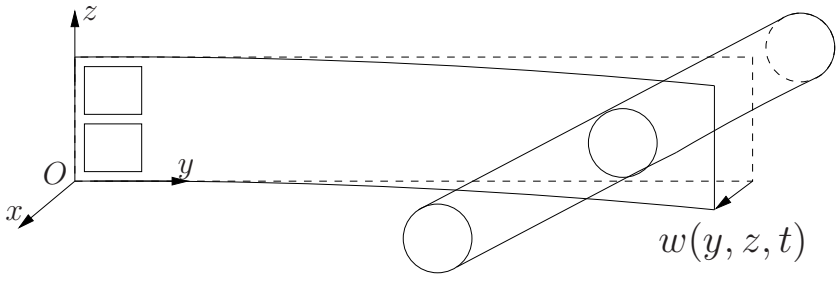

Figure 1.3: Deformation of the rectangular plate (1^{st} mode)

The length of the plate is along the horizontal axis and its width is along the vertical one (see Figure 1.3). At the clamped end, there are two actuators glued on one side and two sensors on the opposite side. The plate is constructed from

aluminium and has the characteristics depicted in Table 1.1 below. A view of the plate without the cylindrical tank can be seen in Figure 1.4.

Plate length	L	1.36 m
Plate width	l	0.16 m
Plate thickness	h	0.005 m
Plate density	ρ	2970 kg m^{-3}
Plate Young modulus	Y	75 GPa
Plate Poisson coefficient	ν	0.33

Table 1.1: Plate characteristics

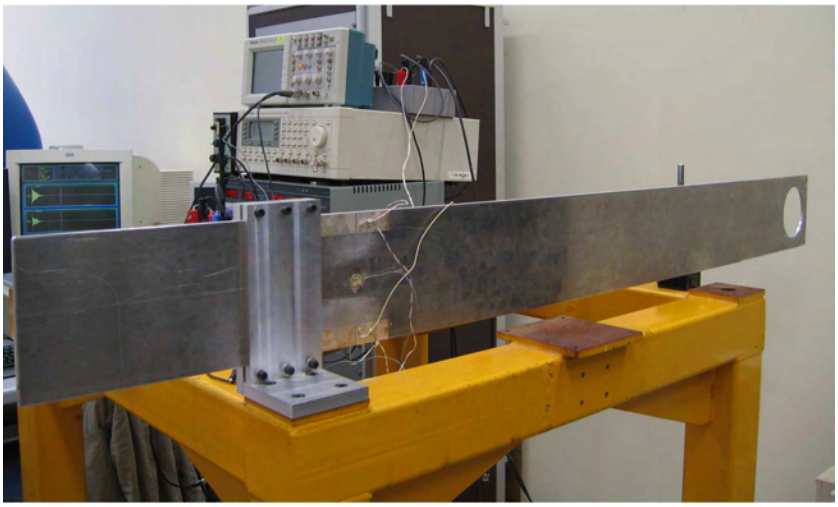

Figure 1.4: Rectangular plate without cylindrical tank

The tank is centered at 1.28 m from the plate clamped side and is symmetrically spread along the horizontal axis. Due to the configuration of the whole system, the tank undergoes a longitudinal movement when the plate has a flexion movement and a pitch movement if the plate has a torsion movement.

The geometrical characteristics of the horizontal cylindrical tank are given in Table 1.2. It can be removed or filled with ice or water. If the tank is filled with ice, it can be easily modeled by a steady mass [123] equal to the empty tank mass plus the mass of the ice.

The ratio between the liquid height and the total height of the tank gives the tank fill level, which is a good indicator of the tank behavior. When the tank fill level is close to 0 or close to 1 (the tank is almost empty or almost full), there is no sloshing behavior, and the modeling process is similar to the case of frozen water.

Tank exterior diameter	0.11 m
Tank interior diameter	0.105 m
Tank length	0.5 m
Tank density	1180 kg m^{-3}
Tank Young modulus	4.5 GPa

Table 1.2: Characteristics of the cylindrical tank

The interesting cases are when the tank fill level is between these values. In this case a sloshing phenomenon occurs, which is characterized by a periodic motion of the liquid free surface. This motion creates periodic forces and moments of force. It is in this situation that this work is placed, therefore, we will further consider only the cases for which the sloshing motion occurs. A more complete description of this phenomenon will be given later in Section 2.3.1 of Chapter 2.

The movement of the plate is generated by some piezoelectric actuators while information about plate deformation are gathered using piezoelectric sensors. Moreover, the actuators can be used as a control input or as a perturbation input. More details about the actuators/sensors geometry and behavior are given below in Section 1.3.

Let us first describe the data acquisition chain.

1.2 Data acquisition chain

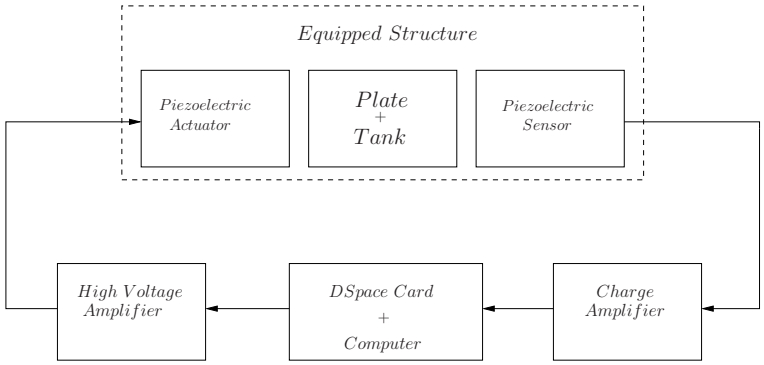

Figure 1.5: Equipped experimental setup

In order to record the information transmitted to the actuators and given by the sensors, some acquisition chain is used. A schematic representation of the experimental device with the acquisition system is depicted in Figure 1.5. In the following lines we

present the different components of the chain that make possible the implementation of numerical controllers. They are listed below starting from the signal delivered by the sensor until the voltage delivered to the actuator.

The data delivered by the piezoelectric sensor is first collected by a charge amplifier before being delivered to the DSpace© card. The charge amplifiers, one for each sensor, are of type 2635 and are made by Brüel & Kjaer [33]. Their picture along with the connections to the experimental device are presented in Figure 1.6. The principle of the charge amplifier is to set, using an operational amplifier, a null voltage between the sensor electrodes so that the eventual parasite capacitance vanishes. In this way, all the charges on the sensor electrodes are send towards a capacitance where a voltage, corresponding to the charge difference, is measured. For further details about the electric scheme of the device one can read reference [81].

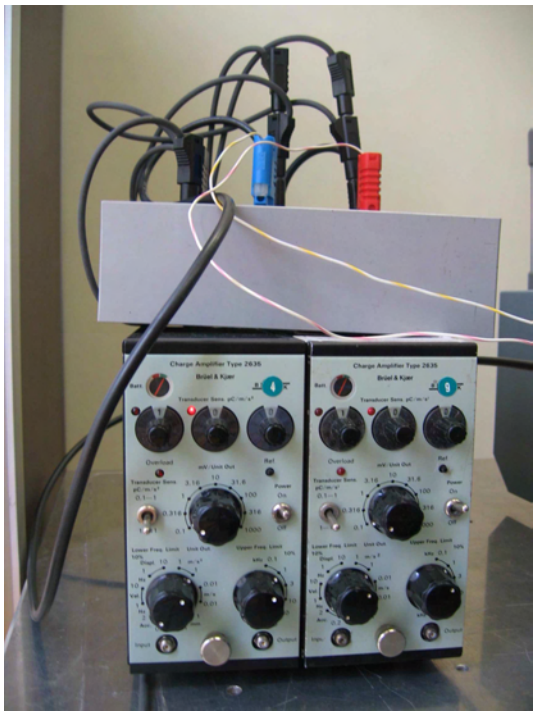

Figure 1.6: Detail view of charge amplifier

The signal delivered by the charge amplifier is sent to a computer using a DSpace card. Using the same card, the signal delivered by the computer is send to the high voltage amplifier. The control laws are implemented on the computer and executed in real time with a selected sampling time of 0.004s.

In order to manipulate the different signals, delivered to the actuators and received from the sensors, the software xPC Target from Matlab© is implemented on the

computer. It allows the real time execution of a Simulink model on the computer via an optimized real-time kernel.

The xPC Target creates a real-time testing environment for Simulink models by connecting a host computer, a target computer and the experimental device under test. Visual details of the acquisition chain are presented in Figure 1.7 where the master (computer on the left side) and slave (computer on the right side) computers, along with the DSpace© card can be seen. The master computer, on which are running xPC Target, Simulink and an C-compiler, is connected to the slave computer via a single TCP/IP communications link. The slave computer is connected to the experimental setup. Based on the Simulink model, a code is generated by Real-Time Workshop and downloaded to the target computer via the communications link. During the acquisition process, the results are stored on the slave computer and then can be uploaded to the master using Matlab© and xPC Target software.

Figure 1.7: Detail view of acquisition system and xPC Target

Finally, the voltage delivered to the plate, by the DSpace© card, is amplified by a high voltage amplifier. It has an amplifying gain of 13 and can deliver a maximum voltage of ±100V. In order to be functional, it has to be powered at ±15V and ±100V. One voltage amplifier connected to a source delivering ±15V can be seen in Figure 1.8. Although the device is home-made at ISAE-ENSICA, his characteristics are those of model PB58 from APEX Microtechnology Corporation [10].

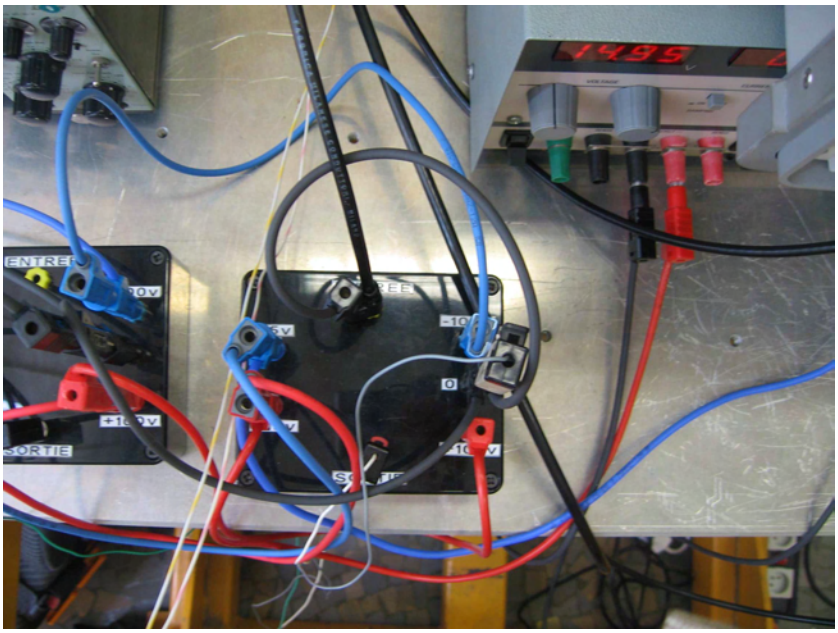

Figure 1.8: Detail view of high voltage amplifier

1.3 Actuators and sensors

As presented earlier, there are two actuators and two sensors which are glued on the plate towards the clamped side (see Figure 1.9 for the actuators and Figure 1.10 for the sensors). The actuators are glued on one side of the plate while the sensors are glued on the other side, thus there are two pairs of collocated actuators and sensors. Since they are all made from piezoelectric materials some detailed information is given in this section concerning their behavior.

The piezoelectric ceramics belong to the larger group of ferroelectric materials, that is to say, materials which are spontaneously polarized (without an electric field being applied).

The piezoelectric actuators are made from PZT (Lead zirconate titanate), model PIC 151. The material model used (PIC 151 is considered a "soft" PZT) it is the standard material used for actuators. In order to create a moment, both actuators lengthen when a voltage is applied to their electrodes. The two sensors (made from PVDF - Polyvinylidene fluoride, a relatively new class of piezoelectric materials used as sensor devices) are located on the opposite side of the plate with respect to the actuators. They deliver a voltage proportional to their deformation. The characteristics of the collocated sensors and actuators are given in Table 1.3. Both actuators and sensors are commercialized by PI Ceramic, the piezo ceramic division of Physik

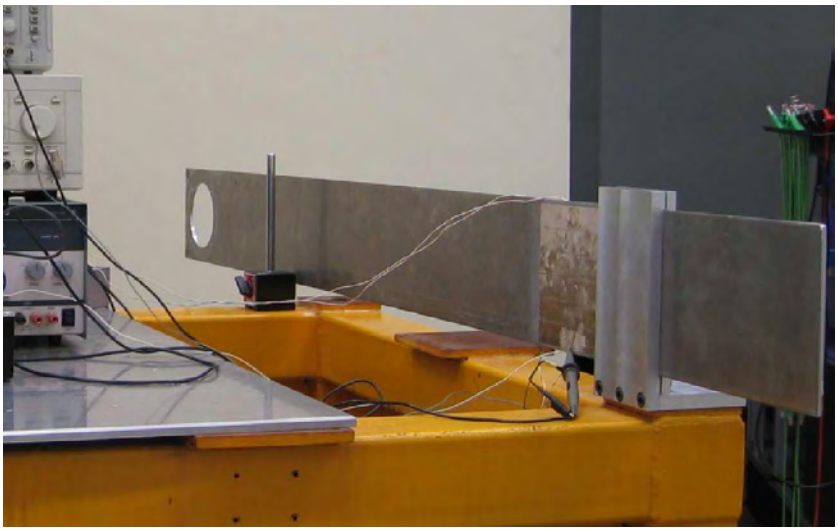

Figure 1.9: Actuators connected to the plate

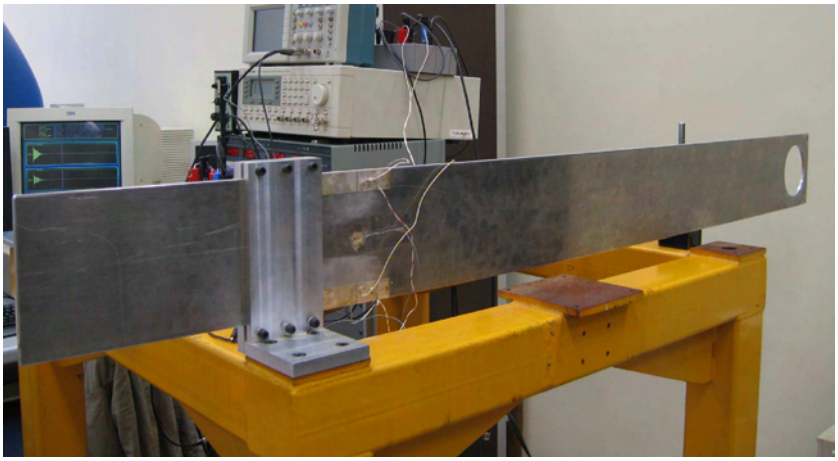

Figure 1.10: Sensors connected to the plate

Instrumente (PI) company [1].

Actuator length/width/thickness	$0.14/0.075/5e^{-4}$ m
Sensor length/width/thickness	$0.015/0.025/5e^{-4}$ m
Actuator/Sensor density	7800 kg m^{-3}
Actuator/Sensor Young modulus	67 GPa
Actuator piezoelectric coefficient (d_{31})	$-210e^{-12}$ m V^{-1}
Sensor piezoelectric coefficient (e_{31})	-9.6 C $(m)^{-2}$
Actuator/Sensor Poisson coefficient	0.3

Table 1.3: Characteristics of the piezoelectric patches

The piezoelectric materials are generally used to attenuate the vibrations and measure the deformation of structures (see [23], [29], [53] among other references for some examples). In the case of flexible structures, many studies also investigate the use of piezoelectric patches to effectively suppress the vibrations (see for instance [11], [45], [66], [140], [144]). Indeed, piezoelectric patches offer a fast response and have a large bandwidth, they are light and low cost, and have good sensing and actuating capabilities. Moreover, they are self-sensing actuators, thus they can be simultaneously used as actuators and sensors. However, only a few results are already available in the literature for fluid-structure systems (see [108] or [109]) for the same structure as ours. For other structures, one can check reference [79] which gives a recent theoretical result and [132] which validates the active control method by means of experimental results.

Despite these advantages, some precautions need to be taken. First of all, the voltage limitations of the materials should be considered. In order to avoid the depolarization of the material, the voltage applied in the opposite direction of the material polarization needs to be carefully controlled (maximum allowance for PZT material is around 500Vmm^{-1}). Second, care should also be taken when the material is exposed to very high temperatures. The limit temperature for a piezoelectric material is defined as the Curie temperature and, again in the case of a PZT material, is around 250 degrees Celsius (exceeding this limit the material is not being ferroelectric anymore thus loosing all piezoelectric properties). In our case though these considerations are respected since the ambient temperature around the experimental setup does not exceed 30 degrees Celsius, while the voltage delivered to the piezoelectric actuators is first limited by the voltage amplifier (see Section 1.2).

The structures that integrate piezoelectric actuators and sensors on a flexible system are often known as active structures or smart structures, while the control on these structures is known as active control (in contrast to the passive control where

additional materials are glued to increase the structural damping of the structure and reduce the vibrations [71], [136]). The control is active due to the fact that the equipped device is self-sensing and self-compensating, due to the piezoelectric patches.

1.3.1 Presentation of the piezoelectric phenomenon

Both actuators and sensors use the piezoelectric effect. Let us shortly describe it.

The existence of the effect was discovered in the 1880 by the Curie brothers on quartz crystals. When a stress is applied, these crystals have the property to develop a proportional electric moment. Our purpose here is not to give a complete characterization of the phenomenon but just some details that will help the reader to better understand the behavior of the actuators/sensors. The modeling will be given in Section 2.2.3.2 of Chapter 2. For a detailed description of the piezoelectric phenomenon [100], among others, gives a complete characterization.

The piezoelectric effect is twofold: the direct piezoelectric effect (also known in the literature as the generator effect) presented above and the converse piezoelectric effect. The latter is defined as the shape change of a piezoelectric crystal when an electric field is applied. Moreover, it can be seen as a thermodynamic consequence of the direct effect.

As it can be seen from the above statements, piezoelectric materials experience both electric and mechanical phenomena. Therefore, the complete piezoelectric equation is defined as a combination between:

- a mechanical phenomenon, described, for an elastic material experiencing only small perturbations, by the tensor expression of the classical Hook law connecting the strain ϵ to the stress σ by the means of the compliance tensor s [100]:

$$\epsilon = s\sigma; \tag{1.1}$$

- an electric phenomenon, described by the electric behavior of the material connecting the electric displacement D to the electric field intensity E and the electric permittivity κ [100]:

$$D = \kappa E. \tag{1.2}$$

Moreover, in the case of the polarization of a crystal produced by an electric field, (a piezoelectric crystal for instance), the last equation describing the electric behavior becomes:

$$D = \kappa_0 E + P \tag{1.3}$$

where P is the polarization charge per unit area taken perpendicular to the direction of polarization (or short polarization) and $\kappa_0 = 8.854 \times 10^{-12}\mathrm{Fm}^{-1}$ is the vacuum permittivity .

At the same time, each type of piezoelectric effect (direct or converse) is described by his own specific relations.

• On the one hand, the direct piezoelectric effect is described by a relation linking up the polarization charge P of the stress σ applied to the crystal sides:

$$P = d\sigma \tag{1.4}$$

where d is a constant value called piezoelectric modulus [100, Chapter 7];

• On the other hand, the converse piezoelectric effect is described also by a relation between the strain ϵ, responsible for the change of shape of the material, and the intensity of the electric field E [100, Chapter 7]:

$$\epsilon = dE \tag{1.5}$$

where the coefficient d is the same as in (1.4).

By combining the relations (1.1) and (1.3) with (1.4) and (1.5) we obtain the complete piezoelectric equations [75, Chapter 13]:

$$\begin{aligned} \epsilon &= s\sigma + dE, \\ D &= d\sigma + \kappa_0 E. \end{aligned} \tag{1.6}$$

These equations will be later used in Sections 2.2.3.2 and 2.2.3.3 of Chapter 2 to compute the analytical model of actuators and sensors.

1.3.2 Optimal placement of actuators and sensors

The optimal placement of actuators and sensors is a key problem in the control of flexible structures. Due to the nature of flexible structures, spatially distributed systems, the actuators and sensors can be placed in many locations. Therefore,

the study of the optimal placement is natural when some performance criteria need to be obtained. There are many references which suggest different methods for a better positioning of the actuators as [44], [52], [63], [66] or [86] by analyzing the controllability and observability matrices for a fixed amount of vibration modes or as [8] by studying the energy space of the structure. Even the thickness of the actuator can be calculated in order to have optimum values for the bending moment of the actuator. For this last issue one can check the work of [81] where the author computes the suitable thickness of a piezoelectric patch in order to have maximum values of the bending moment for a specific plate structure.

In the experimental device of this thesis, the position of actuators and sensors was already fixed and could not be changed. Thus, we do not consider the optimal position problem. We give nevertheless, in the following lines, some details about this interesting issue. In the literature, two main types of approaches can be found:

- The closed-loop approach type consists first at choosing the control law to implement on the structure and then to determine, for this specific law, the optimal placement of actuators and sensors. In this case, the location of actuators and sensors is treated as some extra design parameters in the control law computation. For more details one can read reference [141]. The greatest advantage of this method is the optimization for a specific control law but the greatest drawback of the method is also the fact that the position of sensor/actuator patches depends on this control law;

- The open-loop approach type consists in treating this problem independently from the controlled design problem. This case has the main advantage that several control laws can be tested for the same actuator/sensor positioning. For more details one can consider [61], [66], [69], [81], [95] or [96] among many others. In the following lines, we give some details concerning this method.

There are several open-loop approaches in the literature concerning the optimal placement of actuators and sensors. For example one can check [95] where the ideas of controllability and observability of actuators/sensors are employed. Another approach can be read in [66], where the actuators/sensors are collocated and placed at the location where the highest position sensitivity of each mode is experienced.

We will now explain briefly the method detailed in [95] since it is very easy to implement.

This method is based on the notions of controllability for actuator placement and of observability for sensor placement. These notions, although they are well known,

will also be briefly detailed, for the general case of a linear system, in Section 3.2 of Chapter 3. This approach seems natural if we think that, usually, actuators need to be placed where they have the highest authority to control the system while the sensors should be placed where they have the highest strength to observe the system. The method is computed separately for the piezoelectric actuators and sensors.

On the one hand, for the actuators, a difference is made between the modal controllability and the spatial controllability. The modal controllability measures the controller authority over each mode of the flexible structure while the spatial controllability measures the actuator authority only over the preselected modes (usually the first vibration modes since the low frequency modes tend to contribute more than the high frequency modes to the structure vibrations). This difference is natural since we want the actuator to have a high authority over the selected modes but, at the same time, to have a low authority over the non selected ones. This is especially true in order to prevent the spillover effect (excitation of high frequency modes). Therefore, in the case of the actuators, the optimization problem proposed by [95] is to maximize the spatial controllability measure while keeping some actuator control over all modes, thus keeping some level of modal controllability.

On the other hand, for the sensors, the optimization problem in finding their location is formulated in a similar way in reference [95] by differentiating the modal observability (observability of the sensor over all the modes) from the spatial observability (observability of the sensor over some selected modes). Finally the optimization problem is formulated in order to maximize the spatial observability while maintaining a minimum level of modal observability.

After finding the optimal position of actuator location and of sensor location separately, the inherent question is wether or not this method can be implemented for the position computation of both piezoelectric actuators and sensors. It is proven in [95] that it is easier to find the optimal placement of a collocated actuator/sensor pair by studying only the controllability or the observability and not both (which can be time consuming).

For our experimental setup, as said earlier, the position of the actuators and sensors was fixed in advance. Thus, we did not study the problem of optimal placement and use the device as it is.

1.3.3 Dynamic of piezoelectric patches

Another thing that should be considered is the inherent dynamics of actuators and sensors. This is an important issue during the modeling of the piezoelectric patches since their dynamics may modify the total dynamic of the modeled system.

As detailed earlier in Section 1.2, some high voltage amplifiers are used before the piezoelectric actuators for the control of the flexible structure. A first order dynamical model of this type of actuator, similar to the one in [131], is computed below:

$$\tau \dot{v} + v = ku \tag{1.7}$$

where u is the input voltage and v is the output delivered voltage. Moreover, the constants have the values $\tau = 4.85e^{-7}$s and $k = 1$, determined from the technical specifications in order to fix the cut-off frequency of the model at the same level as the amplifier bandwidth. Based on these issues, the minimal period of the output voltage delivered by the amplifier is $3.25e^{-5}$s.

At the same time, we need to compute the maximal response speed for the piezoelectric actuator. We remark that, if the speed of the actuator is larger than the speed of the voltage amplifier, then we do not need to take into consideration the actuator dynamics. In this case, the speed of the piezoelectric actuator response saturates after the voltage amplifier does.

According to the technical specifications from PI Ceramic catalog [1], the PZT reaches his nominal displacement in 1/3 of its resonant period, provided that the necessary current is delivered. Besides this, the resonant period is defined as $T_0 = \frac{L}{N_1}$, where L is the length of the piezoelectric actuator and N_1 is the frequency constant for the transverse oscillation of a slim rod polarized in the longitudinal direction. In our case, the length in taken from Table 1.3 while the frequency constant for the PIC 151 material is $N_1 = 1500$. Therefore, the resonant period of the piezoelectric actuator is $3.11e^{-5}$s.

As it can be seen, the maximal speed for the actuator is larger than the maximal speed for the voltage amplifier. Thus, for a given excitation, the actuator response time is much smaller than the one of the voltage amplifier. Therefore, his dynamic can be neglected since is not interfering in the response time of the total structure.

Tests regarding this issue are done in Section 4.1 of Chapter 4.

1.4 Conclusion of the chapter

In this chapter we gave a general presentation of the experimental device we are working on. The acquisition chain that will help us implement the controller for vibration attenuation is also shown. Moreover, the characteristics of the plate/tank system along with those of the piezoelectric actuators and sensors are presented. These characteristics will allow us to compute the analytical model of the device in Chapter 2.

Chapter 2

Mathematical modeling of the system

2.1 Introduction

In this chapter we detail the different steps to build the mathematical model of the fluid/structure system depicted earlier. We can find in the literature two different approaches concerning the modeling of such devices:

- A numerical approach based on finite element method (FEM). The method approximates the distributed parameter system with an unlimited number of degrees of freedom and modes by a finite dimensional discrete system. To do this, the whole structure body is divided in several subdivisions or finite elements. Finally, the finite element description of the structure is a sum of beam and lumped mass elements. Further on, the mass and stiffness matrices are found from the expression of the kinetic and potential energies for the system with finite degrees of freedom. As a result the finite element method provides a quite good approximation for the frequencies and mode shapes. For further details about the description of the method one can check for example [83] or [147]. The cases where FEM is employed during the modeling phase are numerous, as an example one can check [86], [133] for a flexible plate system or [108], [109] for a fluid plate system, among many others;

- An analytical approach which allows to find an analytical solution, of infinite dimension, for the electromechanical infinite dimension problem. For this case also, the references in the literature are numerous. Among many others, for a flexible structure system we can cite [63], [81], [107].

Usually in the literature, for " simpler " academical structures like beams or even plates with a geometry not very complicate, the preferred approach is the analytical

one which allows the computation of a simple model. While thinking of more complex structures, like the one in our case, the approach mostly employed in the literature is using the numerical modeling based on FEM method. Even though this method offers the possibility to model items with a complicated shape, their structure geometry can not change in time. To the best of our knowledge, only structures that are in a solid form (oil pipelines, plates, beams, rings of different shapes and sizes, full tanks) can be modeled, but we can not model the liquid sloshing. Nevertheless, recent advances ($\sim$ year 2006-2007) in the ANSYS© software (finite element method simulator software), show that a recent toolbox on computational fluid dynamics called FLUENT© might be able to solve this type of issue.

In our case though, this method is difficult to use. Using finite element method, the liquid, can only be modeled as a "frozen liquid" which acts as a steady mass with no sloshing phenomenon. Moreover, in our case, the sloshing behavior is of great importance since it significantly changes the system dynamics especially in low frequencies. For a study that considers the coupling between a flexible structure and a fluid one can check [98] or again [25]. In the latter, the effect of the fluid is taken into account in the FEM modeling phase by means of an added mass formulation detailed in [97].

For another example one can check the work [114] for the same structure as ours. In this work the author uses the FEM to compute the numerical model of the structure without liquid (therefore without any sloshing behavior). Even though the experiences in [114] are done for three cases: empty tank, full tank and half full tank, the controllers are computed by always considering the tank to be empty.

Therefore, we choose to go on with the analytical approach even though we think that it leads to a more complex modeling phase.

In this chapter we are going to detail the different steps that will lead us to a complete model of the disposal. Since the plate and the tank can be viewed as two separate entities coupled together, the main idea we have in mind is to compute two separate models and then to unite them. Therefore, we will first compute one model for the plate and another model for the tank with liquid. Finally, in order to have the complete structure model we study the interactions between the two models, that is to say the way the behavior of one model affects the behavior of the other.

More precisely we will first write a model for the flexible plate and another for the cylindrical tank with liquid using partial differential equations. The coupling between the two infinite dimensional models is obtained by studying the influence of the plate movement on liquid sloshing and vice-versa. We then make an approximation of the

infinite dimensional model by taking into account only a finite number of modes for the plate and liquid. Based on this, the coupling of the two finite dimensional models is also expressed in finite dimension.

2.2 Plate model

In this section we detail the construction of the model for the rectangular plate with piezoelectric actuators and sensors. The partial derivative equation (PDE) plate model is well known in the literature. For a more detailed presentation one can see for example [30] or [56].

We start from the beam equation (which is a 1-dimensional plate), for the sake of simplicity during the modeling phase. We then study the plate and compute an infinite dimensional model using partial derivative equations (we will see in the next sections that the plate model is constructed on the basis of the beam model). The objective is to give a classical state-space approximation (finite dimension) using the Ritz method to approximate the PDE model. We will get:

$$\begin{cases} \dot{X}_p(t) &= A_p X_p(t) &+ B_p u(t) \\ y(t) &= C_p X_p(t) & \end{cases} \tag{2.1}$$

where X_p is the state-space vector of the plate and A_p, B_p, C_p are respectively the dynamic, control and output matrices. $u(t)$ will be the control (input) variable (the voltage applied to the piezoelectric actuator) and $y(t)$ the output variable (the voltage delivered by the piezoelectric sensor).

2.2.1 Beam model

The beam represents the transposition of a plate in a 1-dimensional space. Since we are dealing with a beam, which is described by only one dimension as it can be seen in Figure 2.1, we deduce that only the flexion movement is possible.

The beam PDE modeling is well known in the literature, one can check for example [30] where models for different types of beams are presented.

We consider an homogeneous beam, clamped at one end and free at the other, of constant section, which has the length L and the mass m. By definition, the dimensions of the beam cross section are much smaller (in theory are null dimensions) than the length of the beam.

The coordinate system $Oxyz$ is selected so that the axes Ox, Oy correspond to

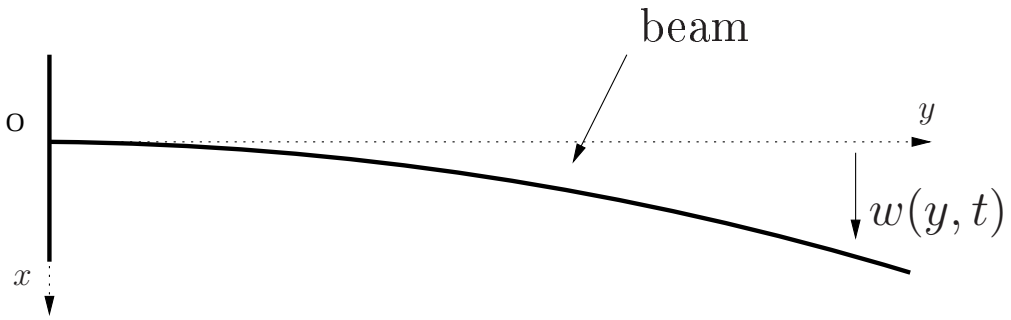

Figure 2.1: Beam with a flexion movement

the main inertia axes. We start the study of transverse beam vibrations supposing that the beam has only flexing movements.

We make the classical cinematic hypotheses as in [56]:

- the beam is uniform and composed of a homogeneous, isotropic elastic material;
- the beam is reduced to its neutral fiber, which by definition will be the part of the beam that does not feel any constraint, thus the axis where the elements are neither lengthened or shortened;
- Bernoulli hypothesis: plane sections remain plane, thus only deformations normal to the undeformed beam axis are considered. This is equivalent to the fact that shear deformations are neglected;
- the beam deformation is only along the x axis. This deformation w is therefore written as a function of the coordinate y defined along the beam length and of time t:
$$w = w(y, t);$$
- the hypothesis of geometrical linearity is verified. This is equivalent to the fact that the deformations have a infinitely small amplitude. The normal longitudinal strain tensor ϵ_y is therefore a linear function of displacement and rotation:
$$\epsilon_y = -x\frac{\partial^2 w}{\partial y^2}.$$

Under these hypotheses and assuming that a flexion moment m_y is acting on the beam, the calculus of potential and kinetic energies lead to the following movement equation by applying the Hamilton principle. Thus, we get the following PDE:

$$\frac{\partial^2 w}{\partial t^2} + \frac{YI}{m_l}\frac{\partial^4 w}{\partial y^4} = 0 \tag{2.2}$$

where $m_l = \frac{m}{L}$ is the linear density of the beam, I the area moment of inertia (second moment of inertia) of the beam cross section about the beam neutral axis and Y the Young modulus of the beam material. Moreover, for a beam of rectangular section of height h and width l, we write the area inertial momentum as (see [30]) $I = \frac{lh^3}{12}$ and the linear density as $m_l = \rho lh = \rho S$, where ρ is the density of the beam material.

Concerning the initial conditions, they are defined as:

$$w(y,0) = w_0(y) \text{ and } \frac{\partial w}{\partial y}(y,0) = w_1(y) \tag{2.3}$$

where w_0 and w_1 stand for the initial deformation and velocity respectively.

Clamped-free beam

As one can read in reference [30, Chapter 8], the boundary conditions of the beam are written for the clamped side by constraining the transverse deformation and his derivative to be null:

$$w(0,t) = \frac{\partial w}{\partial y}(0,t) = 0 \tag{2.4}$$

and for the free side by constraining that the bending moment and Kelvin-Kirchoff edge reaction (which depends on the transverse shearing force and the derivative of the bending moment) are also equal to zero:

$$\frac{\partial^2 w}{\partial y^2}(L,t) = \frac{\partial^3 w}{\partial y^3}(L,t) = 0. \tag{2.5}$$

Of course, other boundary conditions are possible (see [30, Chapter 8]) and some of them will be used latter in this work (for the "free-free" beam for instance).

First, the beam vibration response is obtained by solving the homogeneous equation (2.2) with the initial conditions (2.3) and the boundary conditions (2.4) and (2.5). In our case, homogeneous beam with constant section, it is possible to find an analytical approximate solution for w under the shape of a series [36], [113] using the

variable separation method or Fourier decomposition method [30, Chapter 8]:

$$w(y,t) = \sum_{i=1}^{\infty} Y_i(y) q_i(t). \tag{2.6}$$

To ensure the convergence of the series, we choose the functions $\{Y_i\}_i$ as a set forming a Hilbert orthogonal basis (L^2) of the eigenfunctions of the space differential operator $\frac{\partial^4}{\partial y^4} = \Delta^2$. The existence of this basis is due to the fact that Δ^2 is a compact and symmetric operator [32]. Therefore, the functions $\{Y_i\}_i$ have to be a solution of the eigenvalues problem:

$$\begin{aligned} \frac{d^4 Y_i(y)}{dy^4} &= \lambda_i Y_i(y), \ y \in [0, L] \\ Y_i(0) &= \frac{dY_i}{dy}(0) = 0, \\ \frac{d^2 Y_i}{dy^2}(L) &= \frac{d^3 Y_i}{dy^3}(L) = 0. \end{aligned} \tag{2.7}$$

which has an infinity of solutions (λ_i, Y_i) detailed below.

Since $\{Y_i\}_i$ is an orthogonal basis, one can use the scalar product to compute the beam displacement w:

$$w(y,t) = \sum_{i=1}^{\infty} < w(y,t), Y_i(y) > Y_i(y) = \sum_{i=1}^{\infty} q_i(t) Y_i(y)$$

where $< Y_i, Y_k >= \delta_{ik}$, the Kronecker delta symbol, equal to 1 when $i = k$ and 0 otherwise.

Combining the previous equation with (2.2), we can rewrite the homogeneous equation as:

$$\sum_{i=1}^{\infty} q_i \ \frac{d^4 Y_i}{dy^4} + \frac{\rho S}{YI} \sum_{i=1}^{\infty} \frac{d^2 q_i}{dt^2} \ Y_i = 0.$$

Using (2.7) we get:

$$\sum_{i=1}^{\infty} \left(q_i \lambda_i Y_i + \frac{\rho S}{YI} \ddot{q}_i Y_i \right) = 0.$$

The scalar product with Y_k, for $k \in \mathbb{N}^*$ gives:

$$\sum_{i=1}^{\infty} \left(q_i \lambda_i < Y_i, Y_k > + \frac{\rho S}{YI} \ddot{q}_i < Y_i, Y_k > \right) = 0$$

and using the orthogonality of the hilbertian basis, we get:

$$q_i\lambda_i + \frac{\rho S}{YI}\ddot{q}_i = 0.$$

Therefore, the cinematic parameters q_i verify the differential equations, for $i \in \mathbb{N}^*$:

$$\begin{aligned} \ddot{q}_i(t) + \frac{YI\lambda_i}{\rho S} q_i(t) &= 0, \\ q_i(0) &= < w_0(y), Y_i >_{L^2}, \\ \dot{q}_i(0) &= < w_1(y), Y_i >_{L^2} . \end{aligned} \tag{2.8}$$

and the modal displacements Y_i verify the differential equations (2.7).

Therefore, the solutions of the ordinary differential equation (2.8) are given by:

$$q_i(t) = E_i \cos \omega_i t + F_i \sin \omega_i t$$

where

$$\omega_i = \sqrt{\lambda_i \frac{YI}{\rho S}} \tag{2.9}$$

and E_i, F_i are computed from the boundary conditions.

We then find the modal displacements Y_i by solving the differential equation (2.7).

From (2.9), we infer that there are only two possible cases for λ_i for the "clamped-free" beam: $\lambda_i = 0$ and $\lambda_i > 0$. The third case $\lambda_i < 0$ is not valid, since it will imply that, as the other plate coefficients are positive, there are vibration modes with a complex natural angular frequency.

Let us first consider the simpler case when $\lambda_i = 0$. From (2.7) we have

$$\frac{d^4 Y_i}{dy^4}(y) = 0$$

which has a possible solution of the following shape: $Y_i(y) = A_i y^3 + B_i y^2 + C_i y + D_i$. Solving this equation using the boundary conditions we find the coefficients $A_i = B_i = C_i = D_i = 0$, thus $Y_i(y) = 0$. This solution is again not valid since, as detailed earlier, the $Y_i(y)$ are forming an orthogonal basis thus they can't be equal to zero.

Let us now consider the case $\lambda_i > 0$. Again we need to solve (2.7) with the boundary conditions. There are several approaches in the literature for writing the solutions of this equation. For example one can check [81] where the author writes the

total expression of the modal displacement as a sum of sine, cosine, hyperbolic sine and hyperbolic cosine functions, each function multiplied by an unknown constant which needs to be determined.

Another more elegant and faster approach is the one proposed by [56]. We write the solution of the equation as:

$$Y_i(y) = A_i s_1(\Omega_i y) + B_i c_1(\Omega_i y) + C_i s_2(\Omega_i y) + D_i c_2(\Omega_i y) \tag{2.10}$$

where

$$(\Omega_i)^4 = \lambda_i = \frac{\rho S}{YI}(\omega_i)^2 \tag{2.11}$$

was used to simplify the writing. The functions s_1, c_1, s_2, c_2 are independent and defined as:

$$\left|\begin{array}{l} s_1(\Omega_i y) = \sin(\Omega_i y) + \sinh(\Omega_i y), \\ c_1(\Omega_i y) = \cos(\Omega_i y) + \cosh(\Omega_i y), \\ s_2(\Omega_i y) = -\sin(\Omega_i y) + \sinh(\Omega_i y), \\ c_2(\Omega_i y) = -\cos(\Omega_i y) + \cosh(\Omega_i y). \end{array}\right.$$

As usual, the constants from the displacement equation (2.10) are found by writing the boundary conditions of the beam. As it can be seen, the functions: s_1, c_1, s_2 and c_2 can be easily obtained one from another by a simple derivative operation. Thus, the boundary conditions, that use the derivative of the coordinate up to the third order, are very easy to express. After checking the boundary conditions we notice that we have only four equations but five unknown elements: A_i, B_i, C_i,D_i and $\lambda_i = \Omega_i$.

A fifth equation is therefore found by imposing a normalization equation, which involves the length L of the beam and the modal deformation, for all $i \in \mathbb{N}^*$:

$$\frac{1}{L}\int_0^L Y_i(y)^2 dy = 1. \tag{2.12}$$

We solve (2.7) imposing the shape (2.10) of the solution, with the normalization condition (2.12). We obtain the following solutions for our "clamped-free" beam:

$$Y_i(y) = \cos(\Omega_i y) - \cosh(\Omega_i y) + \varsigma_i^L(\sinh(\Omega_i y) - \sin(\Omega_i y)) \tag{2.13}$$

where ς_i^L is defined by:

$$\varsigma_i^L = \frac{\cos(\Omega_i L) + \cosh(\Omega_i L)}{\sin(\Omega_i L) + \sinh(\Omega_i L)} \tag{2.14}$$

and where the frequency variable Ω_i is the i^{th} positive solution of the implicit equation:

$$1 + \cos(\Omega_i L)\cosh(\Omega_i L) = 0. \tag{2.15}$$

In order to obtain the angular frequency ω_i of the beam modes we first solve the equation (2.15) using a graphical method (a simple plot is drawn and the solutions are checked) and second we used the value of Ω_i in (2.11) to compute it.

Free-free beam

Let us now consider a "free-free" beam of length l along the z axis. The methodology in finding the modal displacements and frequencies is the same. The only changes are of course the boundary conditions (2.4) and (2.5), which now become (see [30, Chapter 8]):

$$\begin{aligned} \frac{\partial^2 w}{\partial z^2}(0,t) = \frac{\partial^3 w}{\partial z^3}(0,t) = 0, \\ \frac{\partial^2 w}{\partial z^2}(l,t) = \frac{\partial^3 w}{\partial z^3}(l,t) = 0. \end{aligned} \tag{2.16}$$

We consider that the hypothesis given in the case of the "clamped-free" beam are respected. Therefore, we can write the displacement w of the beam using again the separation of variable method [30, Chapter 8]:

$$w(z,t) = \sum_{j=1}^{\infty} Z_j(z) q_j(t). \tag{2.17}$$

Following the same approach as earlier, we express the deformation of the "free-free" beam as a solution of the following equations:

$$\begin{aligned} \frac{d^4 Z_j(z)}{dz^4} = \lambda_j Z_j(z), \ z \in [0,l] \\ \frac{\partial^2 Z_j}{\partial z^2}(0) = \frac{\partial^3 Z_j}{\partial z^3}(0) = 0, \\ \frac{\partial^2 Z_j}{\partial z^2}(l) = \frac{\partial^3 Z_j}{\partial z^3}(l) = 0. \end{aligned} \tag{2.18}$$

Different solutions are found based on the values of λ_j. Since for the "free-free" beam, the natural frequency of the modes is again given by (2.9) we infer that, the solution with $\lambda_j < 0$ is physically impossible. Therefore, $\lambda_j \geq 0$.

Let us fist solve the equation for the case when $\lambda_j > 0$. In this case we use the

same approach as earlier, and solve the general equation of the beam (2.18), imposing the shape

$$Z_j(z) = A_j s_1(\Gamma_j z) + B_j c_1(\Gamma_j z) + C_j s_2(\Gamma_j z) + D_j c_2(\Gamma_j z)$$

of the solution, using the normalization condition:

$$\frac{1}{l}\int_0^l Z_j(z)^2 dz = 1 \tag{2.19}$$

and the boundary conditions. This allows us to find the expression of modal displacements:

$$Z_j(z) = \cos(\Gamma_j z) + \cosh(\Gamma_j z) - \varsigma_j(\sinh(\Gamma_j z) + \sin(\Gamma_j z)) \tag{2.20}$$

where ς_j^l is defined by:

$$\varsigma_j^l = \frac{-\cos(\Gamma_j l) + \cosh(\Gamma_j l)}{\sin(\Gamma_j l) + \sinh(\Gamma_j l)} \tag{2.21}$$

and the frequencies are computed from:

$$1 - \cos(\Gamma_j l)\cosh(\Gamma_j l) = 0 \tag{2.22}$$

where the angular frequency γ_j of the j^{th} mode of the "free-free" beam is such that:

$$(\Gamma_j)^4 = \frac{\rho S}{YI}(\gamma_j)^2 = \lambda_j. \tag{2.23}$$

Let us now consider the case when $\lambda_j = 0$, therefore $\Gamma_j = 0$. In this case we obtain the so-called rigid modes. They are characterized by the fact that the "free-free" beam can vibrate (with a frequency equal to zero) without bending itself, like a rigid body.

In this case we have

$$\frac{d^4 Z_j}{dz^4}(z) = 0$$

which has a possible solution $Z_j(z) = A_j z^3 + B_j z^2 + C_j z + D_j$. Using the boundary conditions we obtain $Z_j(z) = C_j z + D_j$ which still has variables to be found.

We think that, *a priori*, for this type of beam the rigid modes can represent a solution. Therefore, we first impose that the deformation at both ends of the beam are identical: $Z_j(0) = Z_j(l)$. Using the normalization condition (2.19), the corresponding

beam deformation for this translation rigid mode is:

$$Z_j(z) = 1, \ \forall z \in [0, l]. \tag{2.24}$$

On the other hand, we impose that the deformation at both beam ends are identical but in opposite directions: $Z_j(0) = -Z_j(l)$ (rotation of the beam). In this case the mode is called rotation rigid mode and is characterized by a deformation (after normalization):

$$Z_j(z) = -\sqrt{12}(\frac{z}{l} - \frac{1}{2}), \ \forall z \in [0, l]. \tag{2.25}$$

Until here we voluntarily forgot the inherent structural damping and we considered only the case of conservative structures. The presence of a damping in a beam equation makes it more difficult to solve since the damping creates a system in which the modes are not decoupled anymore (see [40]).

Nevertheless, when computing the exact value of the frequencies and mode shapes for a real structure it is compulsory to take the damping into consideration. One solution to this problem is given by the Basile hypothesis: *even with a damping coefficient, the movement equations can remain decoupled if the structural damping is sufficiently small and the modes frequencies of the structure are spaced enough.* This hypothesis allows us to describe the entire structure, a beam in our case, by a complete set of equations with no coupling, each equation describing the behavior of a single mode (see [86]).

In the case of the "clamped-free" beam for example, this is written as (see [56, Chapter 3]):

$$\ddot{q_i} + 2\zeta_i\omega_i\dot{q_i} + {\omega_i}^2 q_i = 0 \tag{2.26}$$

where $i \in \mathbb{N}^*$ stands for the mode number and ζ_i being the damping of the i^{th} mode of the "clamped-free" beam. In the case of the "free-free" beam the expression is identical with respect to the mode frequency and damping.

Until here, we computed the PDE model of two beams: a "clamped-free" beam which is along the y-axis and a "free-free" beam which is along the z-axis. As it will be seen in the next section, the beam PDE model and deformations are needed for

computing the rectangular plate model.

2.2.2 Plate infinite dimensional model

In this part we are going to build the model of the rectangular plate with piezoelectric actuators and sensors glued on each side. The plate is clamped at one end and free at the three others. It has a length L, a width l and a thickness h.

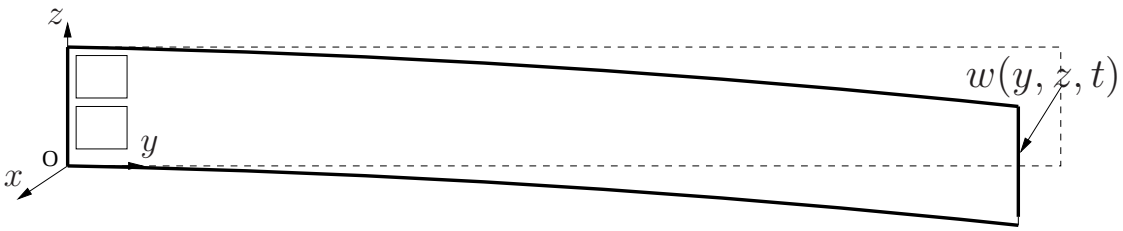

Figure 2.2: Plate bending along x axis

We consider that the plate movement is only along the x-axis (see Figure 2.2) and, as for the beam, we suppose that the following kinematic hypothesis (see [30] or [81]) are verified:

- the material of the plate is considered homogeneous, elastic and isotropic;
- the plate has a constant height;
- the plate is considered very thin;
- the plate sections, which in steady motion are perpendicular to the neutral fiber of the plate, remain perpendicular to the neutral fiber also during movement (this means that the rotary inertia and shear movement along the x axis are considered zero; furthermore, we define the neutral fiber as the imaginary line that stays undeformed during movement);
- we consider only small deformations of the plate.

Further on, we compute the expression of the potential and kinetic energies in order to find the mass and stiffness matrices. A more detailed expression of these matrices is given in [56]. Using this expressions we can infer the partial derivative equation of the plate:

$$m_s \frac{\partial^2 w}{\partial t^2} + \zeta(w)\frac{\partial w}{\partial t} + YI_s\Delta^2 w = \frac{\partial^2 m_y}{\partial y^2} + \frac{\partial^2 m_z}{\partial z^2} \tag{2.27}$$

where m_s is the mass per unit plate area, Y and ν are the Young modulus and respectively the Poisson coefficient of the plate material. The area moment of inertia of the plate about the neutral fiber is $I_s = \frac{h^3}{12(1-\nu^2)}$, similar in expression with the one of the beam (see (2.2) and the details therein). In (2.27) $w = w(y,z,t)$ stands for the displacement (deformation) of the plate along the x axis thus, it depends only on the coordinates y and z and on the time t. The operator quantifying the damping is denoted $\zeta(w)$ and his expression will be detailed latter. Furthermore, Δ is the Laplace operator, Δ^2 being equal to $\left(\frac{\partial^2}{\partial y^2} + \frac{\partial^2}{\partial z^2}\right)^2$.

On the right hand side of the equation, m_y and m_z are the external moments along the y and z-axis. The moment along each axis is delivered to the plate by the actuators (see [47] or [42]) and, as it will be demonstrated latter in this work (see 2.4), by the sloshing modes of the liquid in the tank. Even though, for the time being, we study the plate alone (without the tank filled with liquid), it is easy to see from the moment expression the influence of the tank on the plate.

Equation (2.27) is to be solved using the appropriate boundary conditions and initial conditions. More precisely the boundary conditions are given for the three free sides by:

$$\begin{aligned}
&\frac{\partial^3 w}{\partial y^3} = \frac{\partial^3 w}{\partial z^3} = \frac{\partial^2 w}{\partial y^2} = \frac{\partial^2 w}{\partial z^2} = 0, \quad \forall (y,z) \in \{L\} \times [0,l], \\
&\frac{\partial^3 w}{\partial y^3} = \frac{\partial^3 w}{\partial z^3} = \frac{\partial^2 w}{\partial y^2} = \frac{\partial^2 w}{\partial z^2} = 0, \quad \forall (y,z) \in (0,L) \times \{0,l\}.
\end{aligned}$$

and for the clamped side:

$$w = \frac{\partial w}{\partial y} = \frac{\partial w}{\partial z} = 0, \ \forall (y,z) \in \{0\} \times [0,l]. \tag{2.28}$$

The initial conditions are:

$$\begin{aligned}
w(y,z,0) &= w_0(y,z), \ \forall (y,z) \in [0,L] \times [0,l] \\
\frac{\partial w}{\partial t}(y,z,0) &= w_1(y,z), \ \forall (y,z) \in [0,L] \times [0,l]
\end{aligned} \tag{2.29}$$

where w_0 and w_1 stand for the initial deformation and velocity respectively.

The first step in finding the expression for plate deformation, of $w(y,z,t)$, is to consider the plate equation (2.27) in the absence of the exterior forces and damping:

$$m_s \frac{\partial^2 w}{\partial t^2} + Y I_s \Delta^2 w = 0 \tag{2.30}$$

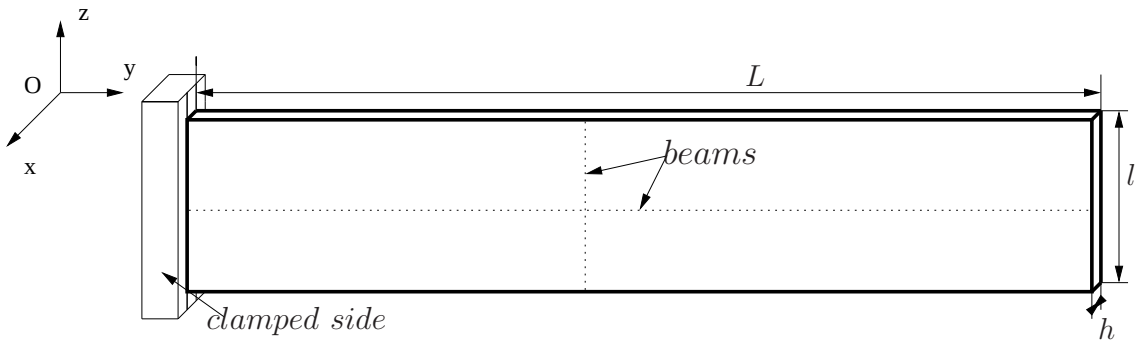

Figure 2.3: The plate and the two beams selected for the choice of the Ritz functions

We use the same approach as in the case of the beam. Therefore the deformation is written in a orthogonal Hilbertian basis using Ritz method:

$$w(y,z,t) = \sum_{k=1}^{\infty} \eta_k(y,z) q_k(t) \tag{2.31}$$

We can find many Ritz functions that can approximate the plate deformation. An intuitive idea is to use a group of functions with a particular shape, resembling as much as possible to the plate. As in [81], we chose two orthogonal beams, their boundary conditions given by the plate boundary conditions. As we have a "clamped-free-free-free" plate, we thus choose a "clamped-free" beam and a "free-free" beam to approximate the deformations. Due to this choice for beam geometry, the Ritz functions η_k, are defined as a product of modal deformations of the two considered beams (see Figure 2.3).

$$\eta_k(y,z) = Y_{i_k}(y) Z_{j_k}(z) \tag{2.32}$$

where $Y_{i_k}(y)$ and $Z_{j_k}(z)$ are the beam modal deformations along the y and z axis respectively. Moreover, each k mode of the plate variable corresponds to a pair denoted (i_k, j_k).

Until here we computed the infinite dimensional model of the plate (see equation (2.27)) using partial derivative equations. Let us now make a finite approximation of the model under the shape of a state-space representation.

2.2.3 Plate finite dimensional approximation

In this section we detail the steps to make the finite dimensional approximation of equation (2.27) (thus implicitly, of equation (2.31) previously written).

It is known (see [63]) that the first modes contain the main part of the energy of the deformation of the flexible structure. It is therefore important to study the behavior of the system specially in low frequencies. Moreover, due to the limited bandwidth of actuators and sensors (their response time is limited thus they cannot respond to very high frequencies), the high frequency modes can not be controlled [15]. Furthermore, using the energy approach presented in Section 3.1 of Chapter 3 and tested in Section 4.2 of Chapter 4, it is possible to check that the first modes contain almost all the energy of the structure. Due to this last issue we think of truncating our model based on the energetic contribution of each mode, thus considering only a finite number of modes.

Using modal analysis techniques we aim at extracting from equation (2.27) a state-space dynamical model, of finite dimension, which will sufficiently represent the dynamical behavior of the structure especially in low frequencies.

Ritz method is widely spread in analytical modeling of rectangular plates. One can check [28], [73] or [80] among many other references. When choosing the Ritz functions, some conditions must be fulfilled. As it is detailed in [56] and in [142], one important condition that must be satisfied is the kinematic boundary condition. In the case of a "clamped-free-free-free" plate as here, this condition states that the transverse deformation and its first derivative must be zero at the clamped side.

As an example, we give in Table 2.1 the construction of the first Ritz functions, based on the first modal displacement of the "clamped-free" beam and on the first modal displacements of the "free-free" beam.

Ritz functions	k	i_k	j_k
$\eta_1(x,y) = Y_1(y)Z_1(z)$	1	1	1
$\eta_2(x,y) = Y_2(y)Z_1(z)$	2	2	1
$\eta_3(x,y) = Y_3(y)Z_1(z)$	3	3	1
$\eta_4(x,y) = Y_1(y)Z_2(z)$	4	1	2
$\eta_5(x,y) = Y_4(y)Z_1(z)$	5	4	1
$\eta_6(x,y) = Y_2(y)Z_2(z)$	6	2	2
$\eta_7(x,y) = Y_5(y)Z_1(z)$	7	5	1
$\eta_8(x,y) = Y_3(y)Z_2(z)$	8	3	2
$\eta_9(x,y) = Y_6(y)Z_1(z)$	9	6	1

Table 2.1: Plate Ritz functions (Z_1 means the mode is a flexion mode while Z_2 means is a torsion mode)

Moreover, because of the number of Ritz functions we select to use (let us denote it N), the plate deformation w from (2.31) now becomes

$$w(y,z,t) = \sum_{k=1}^{N} \eta_k(y,z)q_k(t) = \eta(y,z)^T \cdot q(t) \tag{2.33}$$

where the Ritz functions can be stacked in a vector denoted

$$\eta^T = (\eta_1(y,z), ..., \eta_k(y,z), ..., \eta_N(y,z)) \tag{2.34}$$

and the general coordinates in another vector denoted:

$$q^T = (q_1(t), ..., q_k(t), ..., q_N(t)). \tag{2.35}$$

As stated earlier, in order to ease our work in the control problem, we aim at computing a state-space approximation of the plate model described by (2.27). We therefore detail the computation of each matrix of the state-space representation and at the end this representation will be shown in a compact manner.

2.2.3.1 Computation of the dynamic plate matrix A_p

We used two beams to approximate the deformation of the plate. The exact values of their natural frequency along with their mode shape will be detailed later in Section 4.3.1.1 of Chapter 4, Figures 4.5 to 4.9 and Table 4.3.

There are two different approaches in the literature for the computation of the modal frequencies of the plate:

- A numerical calculus. The approach is detailed in [30] for a plate with different boundary conditions. Based on the boundary conditions, several parameters are computed and finally, the value of the frequency is approximated. Even though the calculus is tedious, the final approximation is quite similar to the analytical result;

- An analytical calculus. This is the approach we use to compute the frequency, first of all because the precision of the method but also for the simplicity of the calculus. Another motivation is that we want to build a fully analytic model.

Using the analytical method, the frequency of the k^{th} mode is written as [30]:

$$f_k = \frac{\vartheta_k^2}{2\pi L l}\sqrt{\frac{Y I_s}{m_s}} = \frac{\vartheta_k^2}{2\pi L l}\left(\frac{Y h^3}{12 m_s(1-\nu^2)}\right)^{\frac{1}{2}} \tag{2.36}$$

where ν is the Poisson coefficient and Y the Young modulus of the plate material. The thickness of the plate is denoted h, the mass per unit plate area is m_s and ϑ_k is a dimensionless coefficient. The coefficient ϑ_k is called the natural frequency parameter and is a function of the Poisson coefficient. It also depends on the mode, on the applied boundary conditions and on the plate ratio $\frac{L}{l}$:

$$\vartheta_k = \vartheta_k(\text{boundary conditions}, \frac{L}{l}, \nu).$$

Concerning the inherent damping of each mode, we use the approach detailed in [87]. In the case of a beam equation, the damping is usually taken constant in time and space and identical for all the modes. In the case of plates, even though many authors consider it as a constant term in time and space and identical for all modes (see for example [73], [81] or [133] among many others), we notice during measurements that for our structure it is different for each vibration mode and is even changing with the input voltage delivered to the actuators. This implies that, for example, the damping of each mode changes when two different voltages are applied to the actuators.

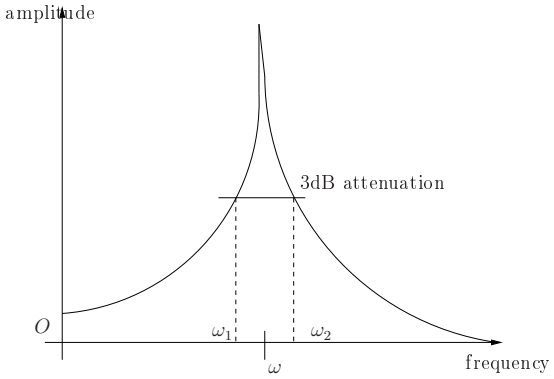

Figure 2.4: Quality factor Q

In order to quantify the damping associated to a mode we use the quality factor Q_k (also known as the Q factor). It is used to characterize the bandwidth of an oscillator relative to its center frequency as it is shown in Figure 2.4. It is a dimensionless parameter that compares the frequency at which a system oscillates to the rate at which it dissipates its energy. The quality factor Q_k can be measured starting from the width of the resonance [127]:

$$Q_k = \frac{f_k}{\Delta f_k} \tag{2.37}$$

where f_k is the resonant frequency in Hertz[Hz] of the k^{th} mode and the bandwidth Δf_k is the width of the range of frequencies for which the energy is at least equal to $\frac{1}{\sqrt{2}} \simeq 0.7$ of its peak value. This is equivalent to 3dB of attenuation.

To experimentally measure the quality factor we use a signal generator and an oscilloscope. Form (2.37) we can define it using the angular frequencies $\omega_k = 2\pi f_k$ in $[\frac{\text{rad}}{\text{s}}]$:

$$Q_k = \frac{\omega_k}{\Delta\omega_{-3dB}} = \frac{\omega_k}{\omega_{k2} - \omega_{k1}}. \tag{2.38}$$

Let us now detail the procedure of calculus of ζ_k from the quality factor Q_k.

As stated earlier in the case of the two beams, we can write an equation for each mode using the dynamical model (2.26). In the case of the plate we make the same analogy as for the beam. Using the Basile hypothesis presented earlier and the cinematic parameters q_k for each mode k of the plate (see (2.35)), we can write a set

of N decoupled equations, one equation modeling each mode:

$$\ddot{q_k} + 2\zeta_k\omega_k\dot{q_k} + {\omega_k}^2 q_k = 0,\ k \in [0, N] \tag{2.39}$$

where ζ_k is the damping of the k^{th} mode and ω_k the angular resonant frequency in $[\frac{\text{rad}}{\text{s}}]$.

The same set of decoupled N equations can be regrouped using the mechanical equation of the plate in the absence of exterior influence [56, Chapter 3.1]:

$$M\ddot{q} + D_s\dot{q} + Kq = 0 \tag{2.40}$$

where M is the mass matrix and K the stiffness matrix. The vector q gathers the coordinates of all modes (see equation (2.35)). We suppose that the energy dissipation of the structure takes the shape of a viscous damping contained in the diagonal matrix D_s.

In our case, since the modes are perfectly decoupled, the mass M is an identity matrix of appropriate dimensions and the stiffness matrix is a diagonal matrix

$$K = diag({\omega_1}^2, \cdots, {\omega_k}^2, \cdots, {\omega_N}^2).$$

Therefore, for the k^{th} mode, the viscous damping becomes:

$$D_{s_k} = \frac{1}{Q_k}\sqrt{{\omega_k}^2} \tag{2.41}$$

where D_{s_k} is the k^{th} diagonal term of the D_s matrix.

The analogy between (2.39) and (2.40), allows to find the damping ζ_k of each mode:

$$\zeta_k = \frac{1}{2Q_k} \tag{2.42}$$

Practically, Q_k is measured for each mode using (2.38). We find the resonant frequency of the mode and we measure the amplitude of the vibrations with an oscilloscope. We divide this value by $\sqrt{2}$ (which is equivalent with placing ourselves on the bandwidth of $-3dB$) and we search on each side of the resonant frequency the two frequencies which have this amplitude of vibration. This procedure is depicted in Figure 2.4. As it can be easily noticed, the quality factor will depend not only on the considered mode, by means of its resonant frequency, but also on the input voltage

used to measure the frequencies. The calculus of the damping factor of each plate mode will be given in Section 4.3.2 of Chapter 4.

When choosing the state-space vector, we have a variety of choices for the state-space variables. The most common choice is $X_p = \begin{pmatrix} \dot{q_1} & q_1 & \cdots & \dot{q_N} & q_N \end{pmatrix}$. Instead of choosing this, we will use the state-space vector proposed in [61] and used also in [81]:

$$X_p = \begin{pmatrix} \dot{q_1} & \omega_1 q_1 & \ldots & \dot{q_N} & \omega_N q_N \end{pmatrix}. \tag{2.43}$$

It allows us to have only elements of comparable amplitude in the dynamic matrix. This will imply a better conditioning for the dynamic matrix and thus for the whole system.

Having the state-space vector from (2.43), we compute the frequencies of each mode using (2.36) and the damping using (2.42). Then the computation of the dynamic matrix A_p of the plate is straightforward using the formulation (2.39) and gives the following proposition:

Proposition 2.2.1. *The dynamic matrix of the plate is:*

$$A_p = \begin{pmatrix} A_{p_1} & 0 & \cdots & 0 \\ 0 & A_{p_2} & \cdots & 0 \\ & \cdots & & \\ 0 & 0 & \cdots & A_{p_N} \end{pmatrix} \tag{2.44}$$

where for each k from 1 to N the block matrices of the diagonal are equal to:

$$A_{p_k} = \begin{pmatrix} -2\zeta_k\omega_k & -\omega_k \\ \omega_k & 0 \end{pmatrix}.$$

2.2.3.2 Computation of the plate input matrix B_p

The plate deflection is modified by the moment of force delivered by the expanding piezoelectric actuator. As presented in Section 1.3 of Chapter 1, when a voltage is applied to the faces of the piezoelectric material, the latter is changing his dimensions, thus creating a momentum which is bending the plate. This voltage applied to one of the two piezoelectric patches used as actuators is the control input of our plate. Therefore, for the calculus of the control matrix B_p of the plate, we have to take into account the behavior of the actuator.

Let us now consider the case of the plate without external influence. We suppose

that the only way the plate can be moved from the equilibrium position is by applying a sinusoidal voltage to the actuators which will deliver a proportional momentum that bends the plate. Furthermore, we consider that the presence of the actuator is not significantly changing the plate mass or plate stiffness, thus is not changing the shape nor the frequency of the modes computed in Section 2.2.3.1, [47].

The piezoelectric actuator model is well known in the literature. As an example one can check the work of [47], [94] or even [81] for the model computation. In the last two cases, in order to maintain the symmetry of the structure and to increase the effect of the patches, two actuators are used. One is glued at the top of the structure and the other at the bottom. They are then activated by applying an identical voltage of opposite sign.

We are aware that the actuator position is very important for the success of the active control. In our case though, the problem is different. As it was detailed in Section 1.3.2 of Chapter 1, due to the system configuration, we can not change the thickness of the actuators nor their position on the plate. Moreover, in our case the control actuator is glued only on one side of the plate and not on both sides as in the references [47], [81].

Furthermore, we propose below an analytical model of the actuators.

Piezoelectric actuators can be used in different configurations depending on what the user wants to do. These different modes are a function of the direction of the electric field (the polarization) and the direction of the material deformation. This coupling gives three main types of behavior for the patches, denoted as modes: longitudinal mode (denoted mode 33), transverse mode (denoted mode 31) and shear stress mode (denoted mode 51). The first two modes are interdependent due to the relation between their corresponding piezoelectric coefficients d_{31} and d_{33} [102].

Let us consider a piezoelectric actuator used in "mode 31", initially suffering no external constraint. The considered mode "31" implies that for a polarization along the x axis, equal stains are induced in both y and z-axis.

Based on the physical behavior of the actuator we can also assume the following hypothesis:

- the patch deformation is identical in the directions y and z due to the equality of strains in these directions. From the patch anisotropy (actuator used in "mode 31") we also infer that the deformation along the x-axis is zero;

- the actuator patch undergoes no torsion effect. Actually we suppose that even if the plate has a torsion movement, the piezoelectric patch does not sense it;

- the deformations are linear along the structure thickness.

Proposition 2.2.2. *The shape of the control matrix B_p is the following:*

$$B_p = (b_{p_1}, 0, ..., b_{p_k}, 0, ..., b_{p_N}, 0)^T \tag{2.45}$$

where the components b_{p_k} are given by

$$\begin{aligned} b_{p_k} &= K_b(Y'_{i_k}(y_{a2}) - Y'_{i_k}(y_{a1})) \int_{z_{a1}}^{z_{a2}} Z_{j_k}(z)dz \\ &\quad + K_b(Z'_{j_k}(z_{a2}) - Z'_{j_k}(z_{a1})) \int_{y_{a1}}^{y_{a2}} Y_{i_k}(y)dy \end{aligned} \tag{2.46}$$

and $(y_{a1}, z_{a1}), (y_{a2}, z_{a2})$ are the coordinates of the actuator opposite corners position and K_b is a constant depending on the plate and piezoelectric patch characteristics.

Proof:

Under the hypothesis detailed before the proposition, the piezoelectric equations for the plate and piezoelectric patches are written using the strain vector (for more details see [100])

$$\epsilon = \begin{pmatrix} \epsilon_{11} & \epsilon_{22} & \epsilon_{33} & \sqrt{2}\epsilon_{23} & \sqrt{2}\epsilon_{13} & \sqrt{2}\epsilon_{12} \end{pmatrix},$$

and the stress vector

$$\sigma = \begin{pmatrix} \sigma_{11} & \sigma_{22} & \sigma_{33} & \sqrt{2}\sigma_{23} & \sqrt{2}\sigma_{13} & \sqrt{2}\sigma_{12} \end{pmatrix}.$$

Due to the transverse mode of utilization of the piezoelectric actuator, the strain and stress vectors are reduced to three components which correspond to the two axes of the induced stress [47]. Therefore, the tensoral Hook law (1.1) can be written:

$$\left| \begin{array}{l} \sigma_{11} = \frac{Y}{1-\nu^2}(\epsilon_{11} + \nu\epsilon_{22}) \\ \sigma_{22} = \frac{Y}{1-\nu^2}(\epsilon_{22} + \nu\epsilon_{11}) \\ \sigma_{12} = \frac{Y}{2(1+\nu)}(\epsilon_{12}) \end{array} \right. \tag{2.47}$$

for the plate and identically

$$\left|\begin{array}{l} \sigma_{p_{11}} = \frac{Yp}{1-\nu_p^2}(\epsilon_{11} + \nu_p\epsilon_{22} - d_{31}(1+\nu_p)\frac{V_a}{h_p}) \\ \sigma_{p_{22}} = \frac{Yp}{1-\nu_p^2}(\epsilon_{22} + \nu_p\epsilon_{11} - d_{31}(1+\nu_p)\frac{V_a}{h_p}) \\ \sigma_{p_{12}} = \frac{Yp}{2(1+\nu_p)}(\epsilon_{12}) \end{array}\right. \tag{2.48}$$

for the piezoelectric patch. Furthermore, for the actuator h_p is the thickness, ν_p the Poisson coefficient and Y_p the Young modulus. As it can be seen, the last term that appears in the expression of the strain components $\sigma_{p_{11}}$, $\sigma_{p_{22}}$ is an expression of the magnitude of the induced strains. It is expressed as a function of the piezoelectric constant d_{31}, actuator thickness h_p and the voltage applied to the patch V_a.

Based on the earlier hypothesis, some simplifications are possible. Since the patch has no torsion effect, we get $\epsilon_{12} = 0$ which implies $\sigma_{12} = 0$.

Due to the linearity of the deformations in the structure we have $\epsilon_{11} = \epsilon_{22}$. Moreover, the deformation elements ϵ_{11} and ϵ_{22} are expressed using their value on the connecting common points on their surface (denoted with the subscript i):

$$\left|\begin{array}{l} \epsilon_{11} = \frac{z}{h-\delta_n}\epsilon_{11_i} \\ \epsilon_{22} = \frac{z}{h-\delta_n}\epsilon_{22_i} \\ \epsilon_{12} = 0. \end{array}\right. \tag{2.49}$$

Here δ_n is the distance of the plate inferior side to the neutral fiber of the structure (plate + piezoelectric patch) as shown in the Figure 2.5.

In the case of the symmetric structures, the values of δ_n becomes equal to the half thickness of the plate. In our case though, since the structure is asymmetrical (piezoelectric actuator patch only on one side of the plate) we have to compute the new position of the neutral plane. Using the method detailed in [74] we computed the distance of the neutral plane to the inferior side of the plate:

$$\delta_n = \frac{h^2Y + h_p^2Y_p + 2hh_pY}{2(hY + h_pY_p)}. \tag{2.50}$$

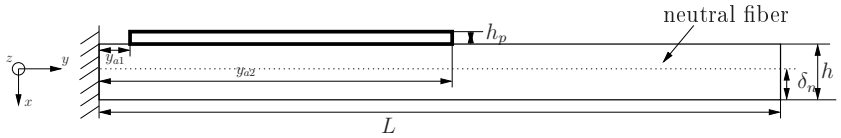

Figure 2.5: Neutral fiber of the rectangular plate

The position of the neutral plane is of great importance since it is used for the equality of moments coming from the plate and the piezoelectric patch. Since we neglected the torsion effect, we can write for the two axes y and z the plane equilibrium condition using the moment expression:

$$\int_{-\delta_n}^{h-\delta_n} \sigma_{11} y dy + \int_{h-\delta_n}^{h-\delta_n+h_p} \sigma_{11p} y dy = 0 \tag{2.51}$$

$$\int_{-\delta_n}^{h-\delta_n} \sigma_{22} z dz + \int_{h-\delta_n}^{h-\delta_n+h_p} \sigma_{22p} z dz = 0 \tag{2.52}$$

Using in (2.51) and (2.52) the values from (2.47) and (2.48) combined with (2.49) and the distance from (2.50), we find the unknown variables ϵ_{11_i} and ϵ_{22_i}:

$$\epsilon_{11_i} = \epsilon_{22_i} = \frac{\frac{\beta((h-\delta_n+h_p)^2-(h-\delta_n)^2)}{2(1-\nu_p)}\frac{d_{31}}{h_p}}{\frac{1}{3(h-\delta_n)}\left(\frac{(h-\delta_n)^3-(-\delta_n)^3}{1-\nu}+\frac{((h-\delta_n+h_p)^3-(h-\delta_n)^3)\beta}{1-\nu_p}\right)} V_a \tag{2.53}$$

where $\beta = \frac{Y_p}{Y}$.

Once the interface stress of the plate is found, the resulting plate momentum can be found by integrating the actuator stress. After the integration on the plate thickness the moment is written as:

$$m_y^a = m_z^a = \int_{-\delta_n}^{h-\delta_n} \sigma_{11} z dz = \frac{Y\epsilon_{11i}}{1-\nu}\frac{(h-\delta_n)^3-(-\delta_n)^3}{3(h-\delta_n)} = K_b V_a \tag{2.54}$$

where:

$$K_b = \frac{\frac{\beta((h-\delta_n+h_p)^2-(h-\delta_n)^2)((h-\delta_n)^3-(-\delta_n)^3)}{6(1-\nu_p)(1-\nu)}}{\frac{(h-\delta_n)^3-(-\delta_n)^3}{1-\nu}+\frac{((h-\delta_n+h_p)^3-(h-\delta_n)^3)\beta}{1-\nu_p}}\frac{Y d_{31}}{h_p} \tag{2.55}$$

Since the momentum is applied only under the actuator, we use the Heaviside step (or unit step function) H to impose this (as in [62]). Therefore, using the coordinates of the actuator opposite corners (y_{a1}, z_{a1}) and (y_{a2}, z_{a2}), we can write m_y and m_z:

$$m_y^a = m_z^a = K_b V_a[\mathrm{H}(y-y_{a1}) - \mathrm{H}(y-y_{a2})][\mathrm{H}(z-z_{a1}) - \mathrm{H}(z-z_{a2})] \tag{2.56}$$

where the Heaviside step is defined as:

$$\mathrm{H}(r) = \begin{cases} 0 \text{ if } r > 0, \\ 1 \text{ if } r < 0. \end{cases} \tag{2.57}$$

In order to finally obtain the input matrix B_p, we compute the total bending momentum Γ generated by the piezoelectric patch along both axes y and z:

$$\Gamma = \int_0^L \int_0^l (\frac{\partial^2 m_y^a}{\partial y^2} + \frac{\partial^2 m_z^a}{\partial z^2}) w(y,z,t) dy dz \tag{2.58}$$

where $w(y,z,t)$ is the deformation of the plate.

Recalling that $w(y,z,t) = \sum_{k=1}^{N} Y_{i_k}(y) Z_{j_k}(z) q_k(t)$ and that the momentum along both axes is given by (2.56), we obtain from the earlier equation the components b_{p_k} of the input matrix B_p. □

2.2.3.3 Computation of the plate output matrix C_p

In order to compute the output matrix C_p we study the behavior of the piezoelectric patch used as sensor. As detailed earlier in Section 1.2 of Chapter 1, the sensor is connected to a charge amplifier which imposes a null electric field between the sensor electrodes. In this way all the charges are sent to a capacity denoted C_a where we can just measure the voltage in order to have the total amount of charges.

Proposition 2.2.3. *The output matrix C_p has the shape:*

$$C_p = (0, c_{p_1}, ..., 0, c_{p_k}, ..., 0, c_{p_N}) \tag{2.59}$$

where each component c_{p_k} is given by

$$\begin{aligned} c_{p_k} &= \frac{K_c}{\omega_k C_a} (Y'_{i_k}(y_{c2}) - Y'_{i_k}(y_{c1})) \int_{z_{c1}}^{z_{c2}} Z_{j_k}(z) dz \\ &+ \frac{K_c}{\omega_k C_a} (Z'_{j_k}(z_{c2}) - Z'_{j_k}(z_{c1})) \int_{y_{c1}}^{y_{c2}} Y_{i_k}(y) dy. \end{aligned} \tag{2.60}$$

and (y_{c1}, z_{c1}) and (y_{c2}, z_{c2}) denote the coordinates of the sensor opposite corners, K_c is a coefficient depending on the plate and sensor characteristics while ω_k is the angular frequency of the k^{th} mode.

Proof:

Due to the electric properties of the piezoelectric material (the presence of an electric polarization due to a mechanical strain) the electric polarization is equivalent to a surface charge distribution σ_p defined using the polarization vector P (see [100]):

$$\sigma_p = P\overrightarrow{n}$$

where $\overrightarrow{n}$ is the unitary vector, normal to the surface of the piezoelectric sensor.

Moreover, due to the piezoelectric behavior, the electric displacement D can be related to the intensity of the electric field E created by the polarization. This relation is described by equation (1.3) recalled here below:

$$D = \kappa_0 E + P.$$

For our case, the intensity of the electric field is zero because of the charge amplifier. Therefore, using the last equation, the surface charge distribution is:

$$\sigma_p = P\ \overrightarrow{n} = D\ \overrightarrow{n}.$$

Integrating σ_p on a closed surface denoted S of normal $\overrightarrow{n}$ we get the total charge Q_p appearing on the sides of the material (see [106]):

$$Q_p = -\int\int_S \sigma_p dS = -\int\int_S D\overrightarrow{n}\, dS$$

If we neglect, as in the case of the actuator, the torsion effect on the sensor, the electrical displacement becomes:

$$D = e_{31}(\epsilon_{11} + \epsilon_{22}),$$

where the fact that the PZT material of the sensor is transverse isotropic and the influence of the charge amplifier ($E = 0$) were used. Moreover, under the same hypothesis as for the piezoelectric actuator, we approximate the deformation of the sensor patch by the deformation in the middle of the patch since the deformation is linear along the sensor thickness:

$$D = -e_{31}\left((h - \delta_n) + \frac{h_p}{2}\right)\left(\frac{\partial^2 w}{\partial y^2} + \frac{\partial^2 w}{\partial z^2}\right) \tag{2.61}$$

where $w(y,z,t)$ is the plate displacement and e_{31} is a piezoelectric coefficient of the sensor. Using the classic equations of a piezoelectric material written for one dimensional patch [27], the connection between the piezoelectric coefficients e_{31} and d_{31} is proven in [26]. Since the sensor is on only one side of the plate, δ_n is the distance computed from (2.50).

In this case, we also have the electric displacement different from zero only under the sensor and thus we use again the Heaviside step H from (2.57) to represent his action on the plate [62].

Using the last equation (2.61) we can write the expression of the total charge Q_p:

$$Q_p = K_c \int_{y_{c1}}^{y_{c2}} \int_{z_{c1}}^{z_{c2}} \left(\frac{\partial^2 w}{\partial y^2} + \frac{\partial^2 w}{\partial z^2} \right) dydz \tag{2.62}$$

where:

$$K_c = e_{31} \left((h - \delta_n) + \frac{h_p}{2} \right).$$

From (2.62), we can compute the total voltage in the output of the charge amplifier. This gives the terms of the output matrix C_p divided by a coefficient.

$$\mathscr{C}_k = \frac{K_c}{C_a} \left((Y'_{i_k}(y_{c2}) - Y'_{i_k}(y_{c1})) \int_{z_{c1}}^{z_{c2}} Z_{j_k}(z)dz + (Z'_{j_k}(z_{c2}) - Z'_{j_k}(z_{c1})) \int_{y_{c1}}^{y_{c2}} Y_{i_k}(y)dy \right)$$

Moreover, due to the choice of the state-space vector (2.43) the components of the output matrix C_p are the one previously computed, divided by the angular frequency of each mode, $c_{p_k} = \frac{1}{\omega_k}\mathscr{C}_k$. □

Conclusion: We computed a finite dimensional approximation of the PDE plate model by considering only the first N modes of the plate. The dynamic matrix A_p is computed by considering two orthogonal beams. After analyzing the behavior of the piezoelectric actuators and sensors the input matrix B_p and output matrix C_p are also computed. Finally a state-space representation of the system is realized:

$$\begin{cases} \dot{X}_p &= A_p X_p + B_p u \\ y &= C_p X_p \end{cases} \tag{2.63}$$

where the state-space vector is computed from (2.43), the dynamic matrix from Proposition 2.2.1, the control matrix from Proposition 2.2.2 and finally the output matrix from Proposition 2.2.3.

2.3 Tank model

In this section we present the different steps to compute the model of the tank filled with liquid.

As the tank is partially filled with liquid, any disturbance of the container will cause a motion of the liquid free surface. This phenomenon of the liquid is called sloshing. Depending on the container shape, different types of motions can be observed.

2.3.1 Sloshing of liquids - state of the art

Liquid sloshing in moving or stationary containers has been studied for many years due to their applicability especially in the aerospace and aeronautic domains. These studies lead to the complex work of Abramson [2] finalized in the early 1960s. Later, these kinds of results were also published in [48] along with some improvements. Many other works can be found in the literature about the liquid sloshing, [34], [67], [92], [97] can be cited among many others.

In the aeronautic and space flight domain, the increase in size of the tank diameters decreases the sloshing frequencies of the propellants and thus affects the vehicles stability. Thus, the eigen (natural) frequencies of the tank liquid shift towards zero, thus coming closer to the control frequencies. This leads to a continuous excitation of the liquid which will influence the overall stability. One can read for instance [138] where the authors present how fuel unpredictable reactions, prevented the NEAR-Shoemaker (Near Earth Asteroid Rendezvous) spacecraft from orbiting the Eros asteroid, delaying the space mission for almost a year. Other examples can be found in [129], concerning the uncontrollable fuel oscillations during flight testing of several planes: Douglas A4D, Lockhead P-80, Boeing KC-135, Cessna T-37 or again the strange fuel shift during takeoff that lead to static pitch instability of North American YF-100 plane.

In order to reduce the influence of the sloshing, there are several solutions. The first, immediate, solution will be to reduce the quantity of liquid in tanks by dividing them in several smaller tanks using walls of different shapes. The second solution is to simply introduce baffles into the liquid to disturb the flow and to create larger

damping which will control the wave magnitude. The third solution is, of course, to choose a suitable control algorithm which will be able to diminish the forces and momenta exerted by the sloshing. We are going to consider further in this work this last solution.

To solve the sloshing problem we need to compute the natural frequency for each sloshing mode along with the mode shape and then the total forces and momenta generated by the sloshing. Moreover, it is easy to show that the natural frequency of each wave depends on the tank shape and on the acceleration (which is either the total acceleration of the system if the tank containing the liquid is in movement, or the gravity alone if the tank is in steady motion) [48]. The knowledge of fluid density and of tank fullness, which will determine these frequencies, is therefore essential in the design process of liquid tanks and in implementing active control [92].

For each mode, though, the calculus of the natural frequencies, mode shape, total forces and momenta is very difficult, exact solutions being possible only for very few special cases such as vertical cylindrical or rectangular tank [67].

Moreover, as the natural frequencies are depending upon the tank shape, analytical expressions of frequency exist for different tank geometries [19], [22], [48], [49], [67], [90], [124], [130]. The general equations of motion for a fluid in closed containers can be simplified by making the following hypothesis which allow the use of classical potential flow theory:

- the container is rigid and impermeable;
- the fluid has no viscosity, is inviscid, incompressible and frictionless. This assumption of frictionless liquid is justified since the damping due to friction at the tank walls is of very small magnitude [18];
- the wave motion is linear in the sense that the wave amplitude is linearly proportional to the imposed tank amplitude. The nonlinear case is not treated here but the reader can check [48] or [54] for nonlinear corrections to the linear theory;
- the wave speed and motion are of small amplitude;

In the case of rectangular and upright vertical cylindrical tanks, the sloshing problem can be solved using the variable separation method which gives a set of decoupled equations, one for each sloshing mode. In the case of tanks with different geometry, the analytical solutions, if they exist, are very difficult to implement due

to their complexity. In this case the most used approach is the one of numerical approximations.

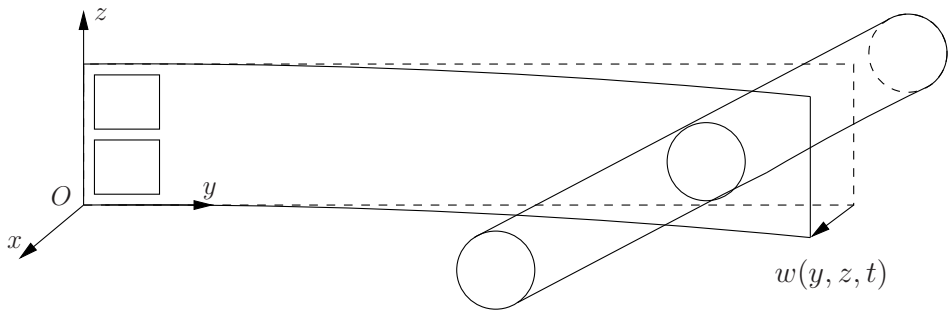

Figure 2.6: Cylindrical tank connected to the plate

In our case, the cylindrical tank is horizontal, has a length L, diameter $2R$ and is filled with liquid up to a level denoted h_s. In Figure 2.6 it can be seen how the tank is connected to the rectangular plate.

The solution of the sloshing problem depends on the type of movement the tank undergoes. We can cite several types of tank movements:

- horizontal motion parallel to either x or y axis due to a force or a momentum along the x or y axis respectively. In this case the solution of the sloshing can be found if we impose for each axis of motion, the equivalence between the velocity of the liquid perpendicular to the plane of the wall and the velocity of the tank wall itself;

- pitching motion along y or even along x axis. In this case also the sloshing problem can be solved imposing that for any point on the tank wall the displacement is proportional to the distance from that point to the pitch axis.

- rolling motion about z axis. In the case of an axisymmetrical tank without internal walls, the rolling motion will cause liquid motion only in a very thin layer near the tank walls and only if the liquid is viscous. Furthermore, this liquid motion, will create, if any, only waves of small amplitude [48]. Under the general assumption of a liquid without viscosity though, no liquid sloshing will be experienced for this type of tank motion, [48].

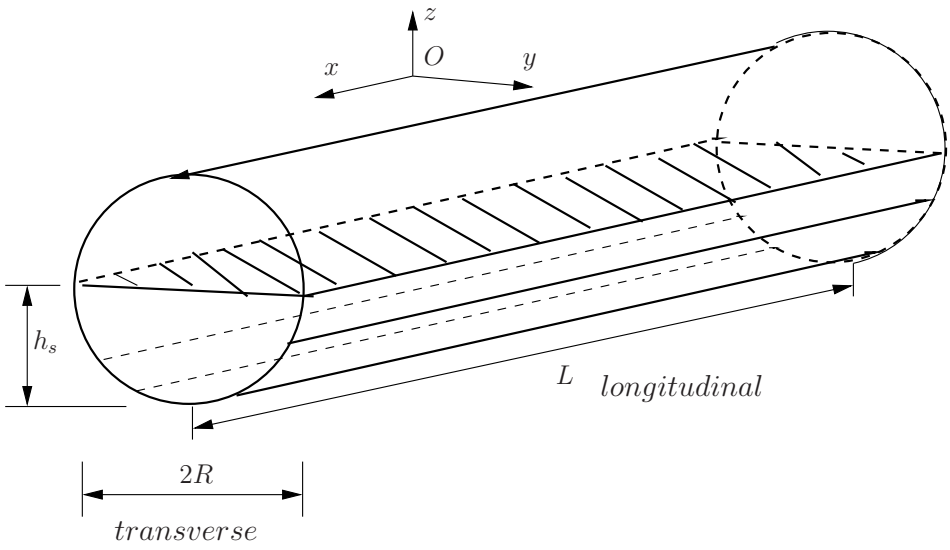

Figure 2.7: Horizontal cylindrical tank

Related to this types of movements (and also since the liquid is considered with no viscosity), the tank connected to the plate can sense only two types of wave movements: a pitch movement along the cylinder y-axis or a longitudinal movement along the longitudinal axis (x-axis) as it can be seen from Figure 2.6 or 2.7.

Usually, the first mode (the one corresponding to the lowest sloshing frequency) is along the longest axis of the cylinder [48]. Thus, the first sloshing mode will be longitudinal if $L > 2R$ (as it is our case here, see Table 1.2) or transverse if $L < 2R$. In the case where the liquid depth h is very small, a notable exception occurs: the first mode is always a transverse one even though $L > 2R$.

Horizontal cylinders partially filled with liquid, as we consider here in this work, are very difficult to analyze in order to determine the natural frequencies and mode shapes. This comes from the fact that the tank walls are not straight and parallel to the axis of symmetry [67], thus the sloshing can't be computed using the separation of variable method.

Based on the two types of movements the tank undergoes, two types of sloshing modes are experienced: a longitudinal sloshing mode along the tank length and a transverse sloshing mode along the tank diameter. Both types are detailed below.

Transverse sloshing modes

Many of the work done in the study of the horizontal cylindrical tanks is for the case of transverse sloshing modes. These modes are along the smaller axis of the tank, their motion being perpendicular to the cylinder generators. To the best of our

knowledge, the work [78] is the first one that, using an energy approach, determined the natural frequency of the first transverse mode but only for a half full horizontal cylinder, while the reference [34] it is the first who proved that the application of the calculus of variations (the energy minimization technique) coupled with successive changes in system coordinates (conformal mapping), allows to obtain some limited results for the general case when the tank filling level can vary. Based on this theory, [48] gives a graphic representation of the natural frequency of the transverse modes. Figure 2.8 presents the dependence of the experimental natural frequencies of the first 3 transverse sloshing modes on the filling level $\frac{h_s}{2R}$ of the tank. As it can be seen the values are increasing when the filling level tends to 1 (tank completely full). It is also easy to notice that, especially for the 2^{nd} and 3^{rd} modes, the natural frequency is varying a lot comparing to the tank filling.

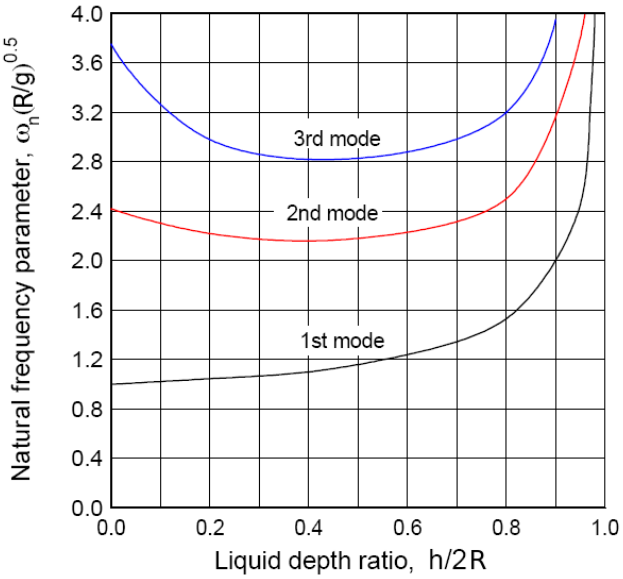

Figure 2.8: Natural angular frequency ω_n of the first transverse sloshing modes (extracted from [48])

Another method in finding the natural frequencies of the horizontal cylindrical tank is given by [90] which uses bipolar coordinates instead of the conformal mapping. Using these frequencies [6] and [7] among others, proposed approximate models in order to estimate mode shapes for partially filled tanks.

A detailed analysis in the case of symmetric and anti-symmetric modes, along

with details about analytically computing the natural frequencies can be found in [67].

Longitudinal sloshing modes

Longitudinal sloshing modes have been much less studied. Most of the known solutions for these modes are in general numerical solutions. As stated in [48] there are no strong analytical results for this type of fluid motion in the case of arbitrary liquid depths, the only results are curves faired through experimental data. In Figure 2.9 the natural frequency of the first three longitudinal sloshing mode is depicted. As it can be seen, for this type of sloshing, the frequency is not changing much compared to the tank filling level $\frac{h_s}{2R}$.

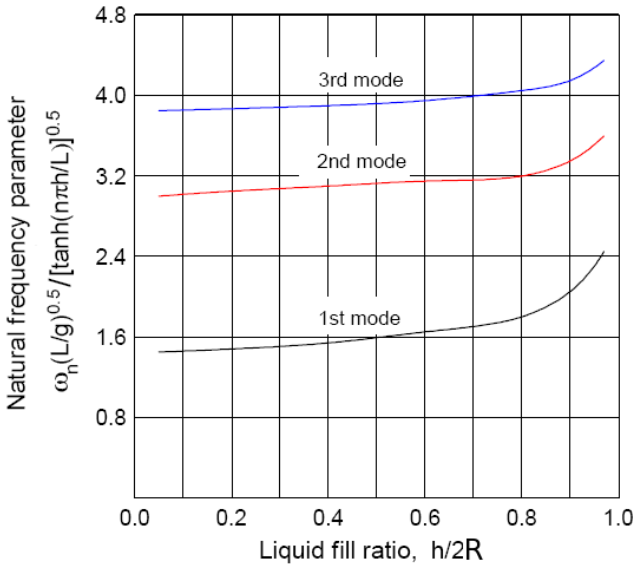

Figure 2.9: Natural angular frequency ω_n of the first longitudinal sloshing modes (extracted from [48])

One notable exception is the case when the tank is half full. In this case there are some analytical results given by [70] and [91] regarding modes shape, forces and momenta generated by the liquid sloshing.

After analyzing the behavior of the experimental device, we notice that both types of tank movements produce only longitudinal sloshing waves. Therefore, from now on we analyze only this type of sloshing modes.

2.3.2 Tank approximation

As we detailed earlier, for longitudinal sloshing modes in a horizontal cylindrical tank there are no analytical results for the natural frequencies and for the forces and moments. This is why we decide, in this work, to make a geometrical approximation of the tank. In general, we state that the new tank can have any shape as long as it can be well described in the Cartesian (x, y, z) coordinate system. In our situation, we therefore approximate the horizontal cylindrical tank by a rectangular horizontal tank. The idea of making a tank approximation is not new, one can also check for example the work [70].

To compute the dimensions of the virtual rectangular tank we propose three different computation methods. The choice of one or another method will be done comparing the computed natural frequencies to the experimental ones on one side (the precision of the method) and the computation complexity plus the time employed in implementing the method on the other side.

First method

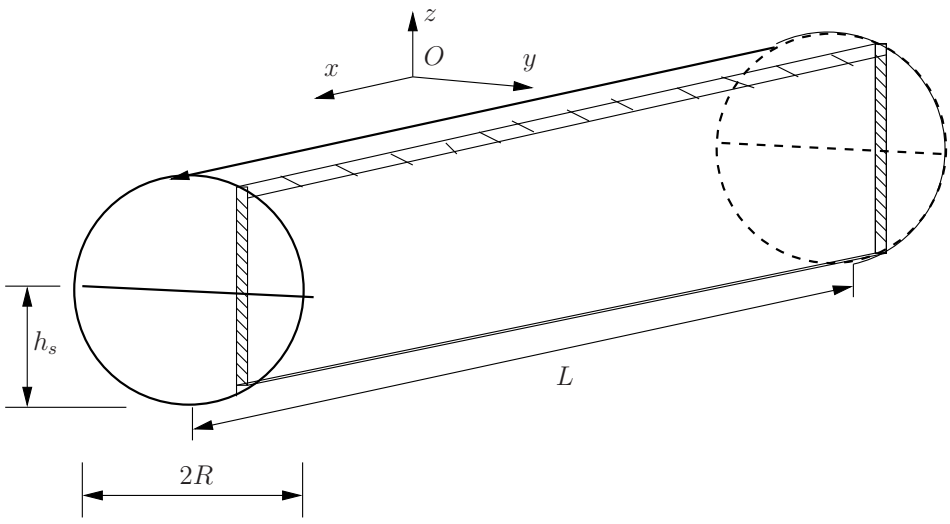

Figure 2.10: Implementing the first method (only one rectangular tank is shown)

The first method we proposed consists in cutting along the longitudinal axis the cylindrical tank in a large (infinite in theory) number of small rectangular tanks. The length of the rectangular tanks is equal to the length of the cylindrical one. As the number of rectangular tanks is large, we can say that they approximate well the curvature of the cylinder and thus the whole cylindrical tank (see Figure 2.10 where one rectangular tank is shown). At the first iteration the filling level in each tank is considered the same as in the case of the cylindrical tank. Further on, for each rectangular tank we compute the natural frequencies depending on the filling level. Based on this frequency, at the second and further iterations, we then change the filling level of each small tank. The core idea is to choose for each tank, a "virtual" filling level so that each tank has a natural sloshing frequency as close as possible to the predicted (from [48]) sloshing frequency. This is done for each sloshing mode from Figure 2.9.

As we expect, (proof in Section 4.3.1.2), this method allows us to obtain natural frequencies very close to the natural frequencies measured on the experimental setup. Nevertheless, the implementation of this method is very tedious because it consists of computing, for each sloshing mode and for each considered small rectangular tank, a new filling level and then the exerted force/moment.

After some repeated experiments we even observed that, if the tank fill level $\frac{h_s}{2R}$ ranges between 0.65 and 0.9 the sloshing natural frequencies given by the method are even closer to the predicted sloshing frequency. This comes though with an increase in difficulty during the implementation phase.

Second method

Another idea consists in choosing the length of the rectangular tank equal to the length of the cylinder and the width of the rectangular tank equal to the tank diameter. The height of the new tank is selected so that the same volume is kept in both tanks.

This method, which is easier to implement than the former method, does not find sloshing natural frequencies close to the ones from [48]. This last issue will be proved later in this work Section 4.3.1.2.

Third method

The last method is very close to the second one but gives natural frequencies that are closer to the experimental ones. As it will be proven later (see Section 4.3.1.2), the frequencies of the rectangular equivalent tank computed using this method are up to only 5% different than the ones from [48]. Since the method remains easy to

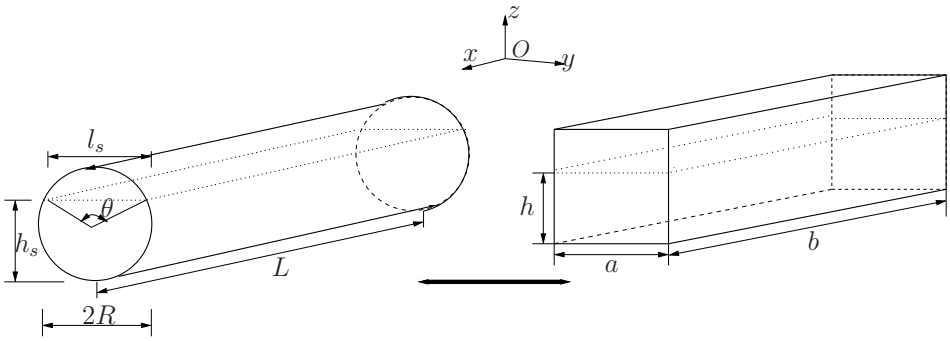

Figure 2.11: Equivalent tanks

implement but also gives good frequency values we decide from now on to use it in the construction of the rectangular tank.

This method keeps the length b and the width a of the rectangular tank equal to the length of the cylinder L and the width l_s of the free surface at rest. The difference of the second method comes from the fact that in this case, the liquid height is chosen so that the volume of liquid in both tanks is the same. Before actually implementing it, we can easily notice that, as for the second method presented here, the parameters of the equivalent tank will need to be recalculated each time the value of the liquid in the tank changes.

Knowing the filling level of the tank $e = \frac{2R}{h_s}$, where R and h_s are the radius and the height of the liquid in the cylinder respectively, we can easily compute the width of the liquid free surface since:

$$l_s = \frac{R}{2}\sqrt{1-(2e-1)^2}.$$

From Figure 2.11 we can write the total volume of the horizontal cylinder V_{cyl} based on the diameter and on the angle θ describing the width of the free surface:

$$V_{cyl} = \frac{R^2}{2}(\theta - \sin(\theta))L$$

where $\theta = 2\arccos(1-2e)$.

Making the analogy between the volume previously computed and the volume of the new rectangular tank which can be easily written as a multiplication of all the tank dimensions ($b \times a \times h$), we compute the height of the liquid h in the rectangular

tank by:

$$h = \frac{R(\theta - sin(\theta))}{\sqrt{1-(2e-1)^2}}. \tag{2.64}$$

All the parameters of the rectangular equivalent tank are now computed. As stated earlier, even though the results given by the first proposed method are more precise (see Table 4.7 from Chapter 4), this last method is preferred due mainly to the simplicity in the implementing phase.

In this paragraph an approximation of the cylindrical tank was conducted. Each of the three method presented will be tested on the experimental setup in Section 4.3.1.2 of Chapter 4 and the theoretical conclusions given here will be checked.

2.3.3 Tank infinite dimensional model

2.3.3.1 General equations

From now on we consider a rigid rectangular container, of length b and width a, partially filled with an incompressible and inviscid liquid to the height h, as shown in Figure 2.12. Thus, the earlier hypothesis given in the introduction of Section 2.3.1 are fulfilled. We finally consider that the dimensions of the container are such that the surface tension is neglected.

As seen from Figure 2.6, the tank is not free but connected to the plate. Therefore, we cannot study the tank alone but in relation with the plate. Since the plate has mostly flexion movements (the torsion movements of the plate are of very small amplitude comparing to the flexion ones, see Section 4.2), we infer that the tank movement is mostly along the generator axis, which corresponds to the x - axis in the coordinate system. Therefore, most of the container moves are horizontal in the x direction. Moreover, based on the plate movement, the tank oscillation has a small constant acceleration C_0.

The fact that the liquid is irrotational allow us to express the fluid velocity as a gradient of a velocity potential function ϕ. Therefore, the liquid speed in all the directions can be written as (see [93, Chapter 2.70]):

$$(V_x, V_y, V_z) = \left(\frac{\partial \phi}{\partial x}, \frac{\partial \phi}{\partial y}, \frac{\partial \phi}{\partial z}\right) \tag{2.65}$$

The introduction of the velocity potential $\phi = \phi(x, y, z, t)$ has the main advan-

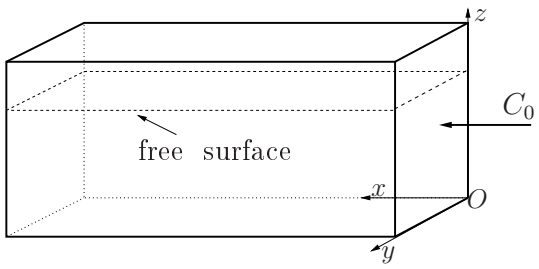

Figure 2.12: Coordinate system for a partially filled rectangular container under external acceleration

tage that all the velocities, forces, moment of forces generated by the liquid sloshing can now be expressed with only one function (which of course will depend on the coordinates x, y, z and on time t).

Since the fluid is incompressible, the equation of continuity (the velocity distribution), that is to say the basic differential equation that the velocity vector must satisfy, is obtained by differentiating with respect to the spatial coordinates, [48, Chapter 1]:

$$\frac{\partial V_x}{\partial x} + \frac{\partial V_y}{\partial y} + \frac{\partial V_z}{\partial z} = 0. \tag{2.66}$$

Furthermore, the Euler equation of motion [78, art. 20], also known as the unsteady form of Bernoulli equation, written for a tank filled with liquid undergoing a longitudinal movement along the x - axis admits the following representation:

$$\frac{\partial \phi}{\partial t} + \frac{1}{2}(V_x^2 + V_y^2 + V_z^2) + \frac{p}{\rho} + g(z-h) - C_0 x = 0 \tag{2.67}$$

for $x \in (0, b)$, $y \in (0, a)$, $z \in (0, h)$ and $t \geq 0$. In these last equations $p = p(x, y, z, t)$ and ρ stand for the pressure and the density of the liquid while the term C_0 stands for the external acceleration.

Using equation (2.66) coupled with equation (2.65), the velocity potential function is a solution of the Laplace equation, which does not explicitly contain the time:

$$\frac{\partial^2 \phi}{\partial x^2} + \frac{\partial^2 \phi}{\partial y^2} + \frac{\partial^2 \phi}{\partial z^2} = \Delta_{x,y,z}\phi = 0, \ \forall (x, y, z) \in (0, b) \times (0, a) \times (0, h), \forall t \geq 0. \tag{2.68}$$

with appropriate boundary conditions.

Given the equation of the free surface like $z = h + \xi(x, y, t)$, the equation of motion

from (2.67) becomes, for all $x \in (0,b)$, $y \in (0,a)$, $t \geq 0$:

$$\frac{\partial \phi}{\partial t} + \frac{1}{2}(V_x^2 + V_y^2 + V_z^2) + g\xi(x,y,t) - C_0 x = 0 \tag{2.69}$$

and the kinematic free surface condition according to [78, art. 9] is for all $x \in (0,b)$, $y \in (0,a)$, $t \geq 0$

$$\frac{d}{dt}(\xi(x(t),y(t),t) - z) \equiv \frac{\partial \xi}{\partial t} + \frac{\partial \phi}{\partial x}\frac{\partial \xi}{\partial x} + \frac{\partial \phi}{\partial y}\frac{\partial \xi}{\partial y} - \frac{\partial \phi}{\partial z} = 0 \tag{2.70}$$

where the equivalences $\frac{\partial \phi}{\partial x} = V_x = \frac{\partial x}{\partial t}$, $\frac{\partial \phi}{\partial y} = V_y = \frac{\partial y}{\partial t}$ and $\frac{\partial \phi}{\partial z} = V_z = \frac{\partial z}{\partial t}$ have been used.

Further progress in finding the expression of ϕ can be made if (2.69) is linearized (by omitting squares and products of x,y,z and ξ). This is a justified approximation if the deflection (the degree to which a structure element is displaced under a load) and slope (gradient) of the free surface are everywhere small [1]. In this case, the simplified equation becomes:

$$\frac{\partial \phi}{\partial t} + g\xi - C_0 x = 0, \ \forall x \in (0,b), y \in (0,a), t \geq 0 \tag{2.71}$$

for the dynamic free surface condition.

Moreover, if equation (2.67) is linearized and written for the steady state ($\frac{\partial \phi}{\partial t} = 0$), also considering that the pressure p on the free surface equals 0, we get another expression for the free surface equation: $z = h + \frac{C_0}{g}x$. Using this last equation, the kinematic free surface condition (2.70) can be simplified in:

$$\frac{\partial \xi}{\partial t} = \frac{\partial \phi}{\partial z} - \left|\frac{C_0}{g}\right| \frac{\partial \phi}{\partial x}, \ \forall x \in (0,b), t \geq 0 \tag{2.72}$$

If we assume $\left|\frac{C_0}{g}\right|$ to be of small quantity (we think that, at least in laboratory conditions, the external acceleration is much smaller than the gravity), from (2.72) we obtain $\forall x \in (0,b), y \in (0,a), t \geq 0$

$$\frac{\partial \xi}{\partial t} = \frac{\partial \phi}{\partial z} \tag{2.73}$$

on the free surface ($z = h$)

When considering the other boundary conditions, we need to set that the relative

[1] It is interesting to notice that for a real liquid this is not true near the walls [24].

velocity normal to the wall is equal to zero. Hence

$$\begin{aligned} V_x &= \tfrac{\partial\phi}{\partial x} = 0 \text{ at } x = 0, a; \\ V_y &= \tfrac{\partial\phi}{\partial y} = 0 \text{ at } y = 0, b; \\ V_z &= \tfrac{\partial\phi}{\partial z} = 0 \text{ at } z = 0. \end{aligned}$$

which, written in a more compact form, becomes:

$$\frac{\partial\phi}{\partial n} = \overrightarrow{n} \cdot \nabla\phi = 0 \tag{2.74}$$

where $\overrightarrow{n}$ is the unitary outward vector and:

$$\nabla\phi = \left(\frac{\partial\phi}{\partial x} \quad \frac{\partial\phi}{\partial y} \quad \frac{\partial\phi}{\partial z}\right)^T.$$

The vector $\overrightarrow{n}$ takes on the different walls the well known shapes: $n_x = \begin{pmatrix} \pm 1 & 0 & 0 \end{pmatrix}^T$ (on the two walls perpendicular to the x-axis), $n_y = \begin{pmatrix} 0 & \pm 1 & 0 \end{pmatrix}^T$ (on the two walls perpendicular to the y-axis) and $n_z = \begin{pmatrix} 0 & 0 & -1 \end{pmatrix}^T$ (on the wall at the bottom of the tank).

Proposition 2.3.1. *The solutions ϕ and ξ of the unsteady Bernoulli equation (2.67) and of the Laplace equation (2.68), under the boundary conditions (2.73) and (2.74) are:*

$$\phi(x, z, t) = \sum_{i=1,3,5,\cdots}^{\infty} \dot{r}_i(t) \frac{\cosh(\Upsilon_i z)}{\Upsilon_i \sinh(\Upsilon_i h)} \cos\left(\frac{\pi i x}{a}\right) \tag{2.75}$$

and

$$\xi(x, y, t) = \sum_{i=1,3,5,\cdots}^{\infty} r_i(t) \cos\left(\frac{\pi i x}{a}\right) \tag{2.76}$$

where the $r_i(t)$ are given by (denoting $\frac{\pi i}{a} = \Upsilon_i$):

$$\begin{aligned} \ddot{r}_i(t) + g\Upsilon_i \tanh(\Upsilon_i h) r_i &= -\tfrac{4C_0}{ag\Upsilon_i^2} g\Upsilon_i \tanh(\Upsilon_i h) \quad \text{for } i = 2p+1, p \in \mathbb{N} \\ &= 0 \qquad\qquad\qquad\qquad\quad \text{for } i = 2p, p \in \mathbb{N} \end{aligned} \tag{2.77}$$

Proof:

In order to find the expressions of ξ and ϕ, and to prepare the field for finite

dimensional approximation, we write them in the Hilbert basis $L^2([0,a]\times[0,b])$ composed of the eigenfunctions of Δ_{xy} with Neumann homogeneous boundary conditions. Therefore we obtain for the two functions the general shape:

$$\begin{aligned}\phi(x,y,z,t) &= \sum_{i=0}^{\infty}\sum_{j=0}^{\infty} g_{ij}(t)f_{ij}(z)S_{ij}(x,y)\\ \xi(x,y,t) &= \sum_{i=0}^{\infty}\sum_{j=0}^{\infty} r_{ij}(t)S_{ij}(x,y)\end{aligned}$$

Since the tank is rectangular, we can apply the separation of variable method along the x and y coordinates, to the S_{ij} function [67]. Thus, it can be written as:

$$S_{ij}(x,y) = \cos\left(\Upsilon_i x\right)\cos\left(\Upsilon_j y\right),\ \forall x\in(0,b), y\in(0,a) \tag{2.78}$$

where

$$\Upsilon_{ij} = \pi\left(\frac{i}{a}+\frac{j}{b}\right) \tag{2.79}$$

Therefore, applying the boundary condition on the free surface (2.73) to the expressions of ϕ and ξ from (2.78) we find the dependency between the two functions depending on time t, $\forall x\in(0,b)$ and $\forall y\in(0,a)$:

$$\frac{\partial\phi}{\partial z}(t,x,y,h) = \sum_{i=0}^{\infty}\sum_{j=0}^{\infty} g_{ij}(t)f'_{ij}(h)S_{ij}(x,y) = \frac{\partial\xi}{\partial t} = \sum_{i=0}^{\infty}\sum_{j=0}^{\infty}\dot{r_{ij}}(t)S_{ij}(x,y)$$

which yields to:

$$g_{ij}(t) = \dot{r_{ij}}(t),\ \forall t\geq 0 \text{ and } \ f'_{ij}(h) = 1,\ \forall i,j\in\mathbb{N}. \tag{2.80}$$

Using the boundary conditions (2.74), we have

$$\frac{\partial\phi}{\partial z} = 0 \text{ at } z=0, \forall x\in(0,b), y\in(0,a), t\geq 0$$

and thus we get $f'_{ij}(0) = 0\ \forall i,j\in\mathbb{N}$.

Moreover, after introducing the expression of ϕ into the Laplace equation (2.68), and taking into account (2.80), we obtain:

$$\sum_{i=0}^{\infty}\sum_{j=0}^{\infty}\dot{r_{ij}}(t)\left(-\Upsilon_{ij}^2 f_{ij}(z)S_{ij}(x,y) + f''_{ij}(z)S_{ij}(x,y)\right) = 0$$

$\forall t \geq 0$ and (x, y, z) in the liquid domain. It is easy to notice that the term $f''_{ij}(z)$ comes from the last term in the Laplace equation $\frac{\partial^2 \phi}{\partial z^2}$ and $-\Upsilon^2_{ij}$ comes after using the expression (2.78) on the first two terms of the same Laplace equation: $\frac{\partial^2 \phi}{\partial x^2} + \frac{\partial^2 \phi}{\partial y^2}$.

This last equation gives, for all $z \in (0, h)$ and $\forall i, j \in \mathbb{N}$:

$$-\Upsilon^2_{ij} f_{ij}(z) + f''_{ij}(z) = 0$$

which is to be solved using the boundary conditions on z previously deduced $f'_{ij}(h) = 1$ and $f'_{ij}(0) = 0$. This gives:

$$f_{ij}(z) = \frac{\cosh(\Upsilon_{ij} z)}{\Upsilon_{ij} \sinh(\Upsilon_{ij} h)}, \ \forall z \in (0, h), \forall i, j \in \mathbb{N} \tag{2.81}$$

Using the expressions (2.80) and (2.81) we write the expressions of ϕ and ξ together, $\forall (x, y, z) \in (0, b) \times (0, a) \times (0, h), t \geq 0$:

$$\xi(x, y, t) = \sum_{i=0}^{\infty} \sum_{j=0}^{\infty} r_{ij}(t) S_{ij}(x, y)$$

$$\phi(x, y, z, t) = \sum_{i=0}^{\infty} \sum_{j=0}^{\infty} r_{ij}(t) \frac{\cosh(\Upsilon_{ij} z)}{\Upsilon_{ij} \sinh(\Upsilon_{ij} h)} S_{ij}(x, y)$$

where the values of S_{ij} and Υ_{ij} are the same one from (2.78) and (2.79).

Now, the r_{ij} function are calculated by replacing ϕ and ξ into (2.71), recalled here below:

$$\frac{\partial \phi}{\partial t} + g\xi - C_0 x = 0.$$

The calculation is very tedious. One simplifying solution comes from the type of movement that the tank undergoes. As presented earlier in the beginning of this section, the rectangular tank is moving along the x-axis. This constraint, which at the beginning seems to complicate the problem, will now give us some clues about solving the equation.

Taking into account this constraint, the former expressions of ϕ and ξ can be simplified as follows. For the free surface, equation (2.71) recalled above, which represents the equation of motion, can now be written using (2.80) and (2.81):

$$\sum_{i=0}^{\infty} \sum_{j=0}^{\infty} \left[\ddot{r_{ij}}(t) \frac{\cosh(\Upsilon_{ij} z)}{\Upsilon_{ij} \sinh(\Upsilon_{ij} h)} S_{ij}(x, y) + g r_{ij}(t) S_{ij}(x, y) \right] = C_0 x \tag{2.82}$$

where C_0 is the external acceleration along the x-axis.

Since the right-hand side of the equation depends only on the coordinate x, the equality can be satisfied if and only if the left hand side also depends only on x. Therefore we can write $S_{ij}(x, y) = S_i(x)$ which from (2.78) implies that S_{ij} depends only on x. This is verified if and only if $j = 0$.

With this last simplification, the whilom equations for ϕ and ξ become:

$$\xi(x, y, t) = \xi(x, t) = \sum_{i=0}^{\infty} r_i(t) S_i(x) \tag{2.83}$$

$$\phi(x, y, z, t) = \phi(x, z, t) = \sum_{i=0}^{\infty} \dot{r_i}(t) \frac{\cosh(\Upsilon_i z)}{\Upsilon_i \sinh(\Upsilon_i h)} S_i(x) \tag{2.84}$$

where (see (2.79))

$$\Upsilon_{ij} = \Upsilon_i = \frac{\pi i}{a} \tag{2.85}$$

Equation (2.82) can be written as:

$$\sum_{i=0}^{\infty} \left[\ddot{r_i}(t) \frac{\cosh(\Upsilon_i z)}{\Upsilon_i \sinh(\Upsilon_i h)} S_i(x) + g r_i(t) S_i(x) \right] = C_0 x \tag{2.86}$$

and r_i can be found using the approach of [72], which consists of multiplying both sides by $\cos\left(\frac{i_0 \pi x}{a}\right)$ for a given $i_0 \in \mathbb{N}$ and integrating over the whole length of the tank $[0, a]$. With (2.78) this leads to (2.77) by observing (as in [72]) that the integral of the right-hand side is different from 0 for the odd values of i and equal to 0 for the even indexes. This concludes the proof of Proposition 2.3.1.

From this last equation we observe that, having the r_i, we can compute the velocity potential ϕ from (2.75) and ξ from (2.76). For a detailed expression of the velocity potential, in the case when the fluid behavior is treated as a two or three-dimensional flow, one can check [67, Chapter 1]. □

The computation of the natural frequency of the modes is also quite easy. We start by computing the time derivative for the simplified version of the unsteady Bernoulli equation (2.71) without external acceleration, combined with the simplified kinematic

free surface condition (2.73). Therefore, we obtain:

$$\frac{\partial^2 \phi}{\partial t^2} + g\frac{\partial \phi}{\partial z} = 0 \tag{2.87}$$

As it can be seen, the equation depends only on the the velocity potential, which characterizes the liquid movement and which is already known.

Further on, since the liquid in the tank is continuously moving back and forth with a certain frequency, we can write the velocity potential previously computed (implicitly all the functions depending on time t that are in the expression of ϕ), as a harmonic periodic function $\exp(i\omega_i t)$. Here, the variable ω_i stands for the natural frequency of the i^{th} mode.

After replacing the two times derivative in (2.87) by the equivalent term $-\omega_i^2 \exp(i\omega_i t)$ and canceling out the term $\exp(i\omega_i t)$ which multiplies both sides, we find the expression of the natural frequency for the rectangular tank (where (2.77) was used):

$$\omega_i^2 = g\Upsilon_i \tanh(\Upsilon_i h) \tag{2.88}$$

where $i \in \mathbb{N}^*$ is the index of the sloshing wave.

In theory we have two types of longitudinal sloshing modes: symmetric modes and antisymmetric modes. The difference comes from the value of i (odd or even) that comes in the expression of S_i and corresponds to the natural frequency (2.88).

Symmetric sloshing modes

The symmetric sloshing modes are found for the even values of i, starting with $i = 2$, in (2.88). The shape of the first three sloshing modes is depicted in Figure 2.13.

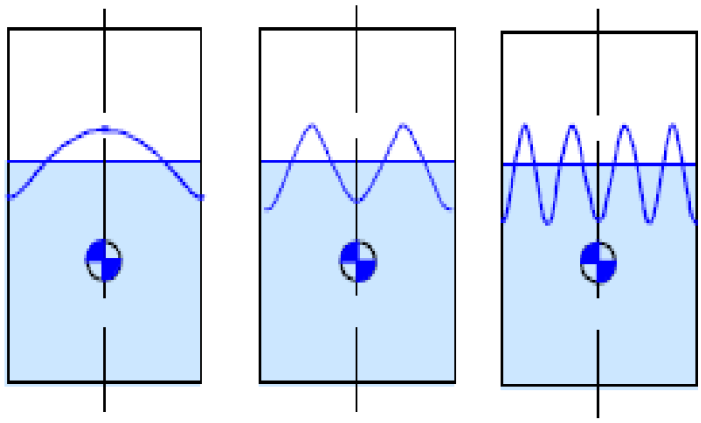

Figure 2.13: The mode shape of the first three symmetric waves (from left to right)

One tool we can use to quantify the sloshing motion is the study of the center of mass. It represents the mean location of all the liquid mass and his position is depicted in our figures by a blue circle in the interior of the tanks.

As it can be seen, the symmetric sloshing modes do not shift the position of the center of mass. Moreover, since the center of mass does not oscillate, there will be no forces or moment of force generated by the liquid sloshing and thus no movement at all of the tank.

Antisymmetric sloshing modes

The antisymmetric modes are found for the odd values of i, starting from $i = 1$. The natural frequency of the antisymmetric modes is again computed from (2.88) (for the odd values of i).

Since the first mode is antisymmetric ($i = 1$), all the frequencies of the symmetrical modes are higher than those of the antisymmetric modes. The shape of the first three modes is depicted in Figure 2.14. The first mode computed for $i = 1$, which is the first on the left, is called the fundamental antisymmetric mode and has the lowest frequency.

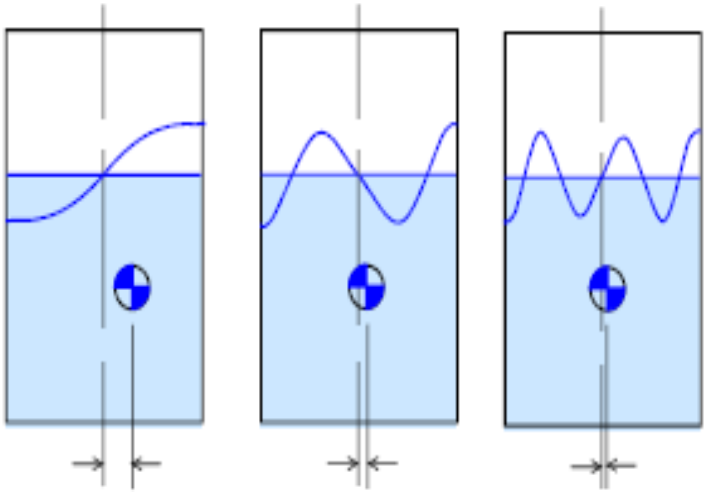

Figure 2.14: The mode shape of the first three antisymmetric waves (from left to right)

As it can be seen from Figure 2.14, during wave movement, a visible shifting in the position of the center of mass can be noticed. Moreover, the oscillation of this position signifies that a large amount of liquid moves from one side to the other side of the tank, thus creating a liquid sloshing which at his turn will create forces and torques. The fundamental mode makes the largest displacement of the center of mass from his equilibrium position. This will create the most powerful sloshing wave, which will induce the greater force and moment on the tank.

Therefore, as a conclusion, for our disposal, the important modes are only the antisymmetric ones since, only they create the sloshing motion. From now on, we concentrate our attention only on this types of sloshing modes.

Until here, after a tank approximation, we computed the infinite dimensional model of the tank with liquid. After analyzing the types of sloshing waves in the tank, our purpose is now to compute all the forces and moments generated by the sloshing. Their value will allow us to describe the tank behavior and its influence on the rectangular plate that is connected on.

2.3.3.2 Determination of forces and moments

Proposition 2.3.2. *The total force generated by the sloshing is* $F = (F_x, F_y, F_z)$ *where:*

$$F_x = \rho abhC_0 - 2\rho b \sum_{i=1,3,5,\ldots}^{\infty} \frac{\ddot{r}_i(t)}{\Upsilon_i^2}, \tag{2.89}$$

$$F_y = 0, \tag{2.90}$$

$$F_z = \rho abgh + \rho bC_0 \frac{a^2}{2}. \tag{2.91}$$

Proof:

The total pressure acting at any point of the liquid is competed from (2.67). After neglecting the second order terms one can write

$$p = \rho \left[-\frac{\partial \phi}{\partial t} - g(z-h) + C_0 x \right] \tag{2.92}$$

The resultant force in the x,y,z-direction is $F = (F_x, F_y, F_z)$ (see [48]). Each component of the force is therefore found by integration of the liquid pressure [122]:

$$F_x = \int_0^h \int_0^b \left(p|_{x=a} - p|_{x=0} \right) dydz, \tag{2.93}$$

$$F_y = \int_0^h \int_0^a \left(p|_{y=b} - p|_{y=0} \right) dxdz, \tag{2.94}$$

$$F_z = \int_0^a \int_0^b \left(p|_{z=h} - p|_{z=0} \right) dxdy = -\int_0^a \int_0^b p|_{z=0} dxdy. \tag{2.95}$$

The minus sign between the two pressures, while computing the total force from the previous three equations, is not due to the sign of the pressure, which is a scalar quantity, but due to the direction of the $\overrightarrow{n}$ vector (which is the vector normal to the considered surface). Since the tank length is along the positive sense of the x-axis (see Figure 2.12), the $\overrightarrow{n}$ vector calculated for $x = a$ is "positive" and the one calculated for $x = 0$ is "negative". The same explanations are valid for the other axis.

In the case of the force along the z-axis, the pressure on the free surface is considered equal to zero and thus the first term of (2.95) computed for $z = h$ is canceled.

Since the movement of the container is only in the x-direction (having only longitudinal sloshing waves) we can simplify the equations (2.93), (2.94) and (2.95). Indeed, because of these considerations the force along the y-axis is equal to zero. Since there are no transverse sloshing waves we have: $p|_{y=b} = p|_{y=0}$ and thus $F_y = 0$.

Moreover, using (2.92) in (2.93) we get:

$$F_x = \rho abhC_0 - \rho b \int_0^h \frac{\partial \phi}{\partial t}|_{x=a} dz + \rho b \int_0^h \frac{\partial \phi}{\partial t}|_{x=0} dz.$$

As stated at the end of the previous section, the sloshing motion of the liquid (the one responsible for creating forces and moments of forces) is generated only by the antisymmetric sloshing modes. Therefore, only odd values of i are considered in the infinite sum. In this case we have $\cos(\Upsilon_i a) = -\cos(\Upsilon_i 0)$ (where $\Upsilon_i = \left(\frac{i\pi}{a}\right)$) and we deduce that $\frac{\partial \phi}{\partial t}|_{x=a} = -\frac{\partial \phi}{\partial t}|_{x=0}$. Thus:

$$F_x = \rho abhC_0 - 2\rho b \int_0^h \frac{\partial \phi}{\partial t}|_{x=0} dz.$$

Replacing ϕ by (2.75), giving

$$\frac{\partial \phi}{\partial t}(x, z, t) = \sum_{i=1,3,5,\ldots} \ddot{r}_i(t) \frac{\cosh(\Upsilon_i z)}{\Upsilon_i \sinh(\Upsilon_i h)} \cos(\Upsilon_i x),$$

we obtain:

$$F_x = \rho abhC_0 + 2\rho b \sum_{i=1,3,5,\ldots}^{\infty} \frac{1}{\Upsilon_i \sinh(\Upsilon_i h)} \int_0^h \ddot{r}_i \cosh(\Upsilon_i z) dz,$$

and integrating along the height of the liquid we get the final expression of the x-coordinate of the force from (2.89).

Concerning the coordinate of the force along the z-axis, we use the same methodology. The difference between the two situations comes from the fact that for the z-axis force, since the tank movement is along x-axis, the term $C_0 x$ from (2.92) has to be taken into account when computing the integrals. Using the pressure described by (2.92) in equation (2.95) we obtain:

$$F_z = \rho abgh + \rho b C_0 \int_0^a x dx - \rho b \int_0^a \frac{\partial \phi}{\partial t}|_{z=0} dx.$$

The last term of the equation is integrated separately and we get:

$$\int_0^a \frac{\partial \phi}{\partial t}|_{z=0} dx = \sum_{i=1,3,5,\ldots}^{\infty} \frac{\ddot{r}_i}{\Upsilon_i \sinh(\Upsilon_i h)} \int_0^a \cos(\frac{i\pi x}{a}) dx = 0.$$

Therefore, the total force along the z-axis is then written as (2.91). □

Proposition 2.3.3. *The total moment of force generated by the sloshing is* $M = (M_x, M_y, M_z)$, *where:*

$$M_x = M_z = 0,$$

$$M_y = \frac{\rho C_0 a^3 b}{12} + 2\rho b \sum_{i=1,3,5,\ldots}^{\infty} \frac{\ddot{r}_i(t)}{\Upsilon_i^2} \left[\frac{h}{2} - \frac{1}{\Upsilon_i \tanh(\Upsilon_i h)} + \frac{2}{\Upsilon_i^3 \sinh(\Upsilon_i h)} \right]. \quad (2.96)$$

Proof:

In a general manner the moment is written [58]: $M = \overrightarrow{distance} \wedge \overrightarrow{force}$, where $\wedge$ represents the cross product (or vector product). We are going to study the moment generated by the liquid sloshing along the three axis. The moment along the x-axis is caused by the pressure acting on the y walls and at the bottom of the tank (the pressure acting on the top of the tank is null). The moment along the y-axis and is caused by the pressure acting on the x walls and again at the bottom of the tank ($z = 0$), while the moment along the z-axis is caused by the pressure acting on the x and y walls. This can be written in a more compact form using the differential element of moment, computed in the center of gravity of the liquid:

$$dM_x = (z - \frac{h}{2}) dF_y + (y - \frac{b}{2}) dF_z = (z - \frac{h}{2}) p dA_y + (y - \frac{b}{2}) p dA_z, \quad (2.97)$$

$$dM_y = (z - \frac{h}{2}) dF_x + (x - \frac{a}{2}) dF_z = (z - \frac{h}{2}) p dA_x + (x - \frac{a}{2}) p dA_z, \quad (2.98)$$

$$dM_z = (y - \frac{b}{2}) dF_x + (x - \frac{a}{2}) dF_y = (y - \frac{b}{2}) p dA_x + (x - \frac{a}{2}) p dA_y. \quad (2.99)$$

One important issue in dealing with the moment of force is its direction since it is a vector. Therefore we consider $\vec{r}$, $\vec{s}$ and $\vec{t}$ the unity vectors in the positive direction of the x, y and z-axis. Taking into consideration that $\vec{r} \wedge \vec{-t} = -(\vec{-s})$ and $\vec{t} \wedge \vec{r} = \vec{s}$, we can compute the direction of the total moment along a specific axis.

As presented before, the force F_y along the y-axis is equal to zero. Moreover, since

there are no lateral sloshing waves, the center of gravity along the y-axis is exactly in the middle of the tank. With (2.97) and (2.99), we get:

$$dM_x = dM_z = 0.$$

Replacing the forces by their expressions computed in (2.89) and (2.91), we finally get from (2.98):

$$\begin{aligned} M_y &= \int_0^h \int_0^b (z - \frac{h}{2}) p|_{x=a} \, dydz - \int_0^h \int_0^b (z - \frac{h}{2}) p|_{x=0} \, dydz \\ &+ \int_0^a \int_0^b (x - \frac{a}{2}) p|_{z=0} \, dxdy. \end{aligned} \tag{2.100}$$

On one hand, replacing the pressure (2.92) in (2.100), we have:

$$\begin{aligned} &\int_0^h \int_0^b (z - \frac{h}{2}) p|_{x=a} \, dydz - \int_0^h \int_0^b (z - \frac{h}{2}) p|_{x=0} \, dydz \\ &\qquad = 2\rho b \int_0^h z \frac{\partial \phi}{\partial t}|_{x=0} \, dz - h\rho b \int_0^h \frac{\partial \phi}{\partial t}|_{x=0} \, dz \end{aligned} \tag{2.101}$$

where the part depending on C_0 is equal to zero. Of course, we used the relation between the time derivatives of the velocity potential, computed for $x = 0$ and $x = a$:

$$\frac{\partial \phi}{\partial t}|_{x=0} = -\frac{\partial \phi}{\partial t}|_{x=a}.$$

On the other hand, using again (2.92), we have:

$$\int_0^a \int_0^b (x - \frac{a}{2}) p|_{z=0} \, dxdy = \rho b \left(C_0 \frac{a^3}{12} - \int_0^a x \frac{\partial \phi}{\partial t}|_{z=0} \, dx + \frac{a}{2} \int_0^a \frac{\partial \phi}{\partial t}|_{z=0} \, dx \right)$$

Summing up these last two equations we find the expression of the moment along y-axis depending only on time derivatives of the velocity potential:

$$\begin{aligned} M_y &= \rho b \left(2 \int_0^h z \frac{\partial \phi}{\partial t}|_{x=0} \, dz - h \int_0^h \frac{\partial \phi}{\partial t}|_{x=0} \, dz - \int_0^a x \frac{\partial \phi}{\partial t}|_{z=0} \, dx \right. \\ &\left. + \frac{a}{2} \int_0^a \frac{\partial \phi}{\partial t}|_{z=0} \, dx + C_0 \frac{a^3}{12} \right) \end{aligned} \tag{2.102}$$

After computing the time derivatives and integrating, we obtain the expression (2.96) of the moment, where the r_i are computed from (2.77). □

In this paragraph we computed the totality of forces and moments of forces gen-

erated by the liquid sloshing. This is done for the theoretical case when an infinite amount of sloshing modes is considered.

2.3.4 Tank finite dimensional model

2.3.4.1 General presentation of the equivalent mechanical model

The objective of this section is to construct an approximate model of the liquid sloshing in the tank. As stated in Section 2.3.3.1 the dynamical effect of the sloshing is a horizontal oscillation of the liquid center of mass relative to the tank. From the works [48], [22], [124], [130] this effect can be well represented by an equivalent linear mechanical model: a mass pendulum system or an equivalent spring mass system. Both mechanical models are presented in Figure 2.15. In the first model, the oscillation of the center of mass, generated by liquid sloshing, is represented by a vertical pendulum with a mass, while in the second model, the same oscillation is represented by a horizontal spring with a mass. A complete overview of the two mechanical models can be found in [67].

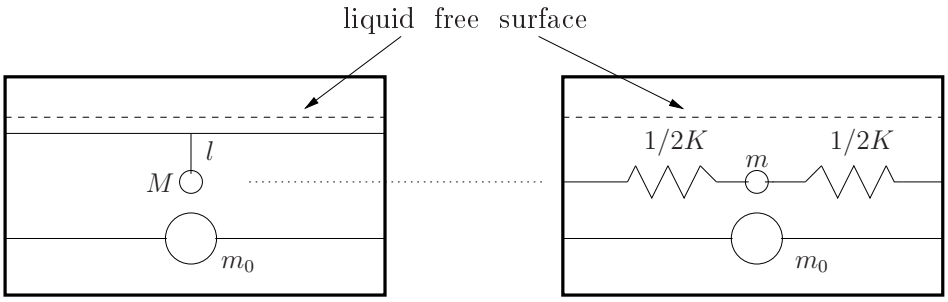

Figure 2.15: Mass pendulum and mass spring mechanical models

In our case there are many reasons why we need to compute the finite dimensional model of the tank with liquid using an equivalent mechanical model. The first reason is because the use of the potential of velocity equation (2.75) is quite difficult to numerically manipulate due to its complexity. For example, as mentioned in [48, Chapter 3], in the case of a space vehicle, coupling of the equations of motion of the vehicle to the equation of motion of a continuous liquid is too computationally demanding even with super computers. Thus, it is convenient to replace the liquid sloshing by a simple linear mechanical system. Besides, as explained in [18], the mechanical model is a good and easy tool for the introduction of linear damping, especially when the magnitude of the damping needs to be determined by experiments.

Finally, another reason is that with a mechanical model, the shape of the model will not depend on the tank geometry or fill level.

An alternative idea in order to compute the state-space representation of the tank with liquid would be to do some model identification. This approach though, which is not based on a PDE model, is difficult to implement due to the structure of the experimental setup. As we can see from Figure 2.6 we cannot decouple the tank from the plate, thus the identification of the tank model will be done through the plate. In this case the eventual errors from the plate model will propagate to the tank model.

One can find two equivalent mechanical models for sloshing behavior in the literature. The natural frequencies of both mechanical systems are easy to compute. In the case of the mass pendulum system, the natural frequency is $\frac{1}{2\pi}\sqrt{\frac{g}{l}}$; while in case of the spring mass system, the natural frequency is $\frac{1}{2\pi}\sqrt{\frac{K}{m}}$, where l and g are the length of the pendulum and the gravitational acceleration, while K and m are the spring constant and the mass of the spring system as depicted in Figure 2.15. Moreover, the transformation between the models is straightforward if we consider the spring mass located at the same height as the pendulum mass (not at the connection point of the pendulum hinge) and that the spring mass is attached to the walls through a spring with a constant of $K = \sqrt{\frac{mg}{l}}$.

The question that rises now is which of the two models is better to use since they are similar, thus exerting the same forces and moment on the tank. Generally, the mass pendulum system is considered more adequate (see [3], [70] or [123] among others) because of his natural frequency $\frac{1}{2\pi}\sqrt{\frac{g}{l}}$ which varies with the changes in axial (or gravitational) acceleration g as the sloshing frequency of the liquid does. In the case of the spring mass system, we will need to change the spring constant K every time the value of g will change (in spite of this issue this approximation is also used by [18]). Even though, for the moment we do not plan to use a time changing gravitational acceleration (although when considering a flying airplane g changes with the altitude), we still prefer this formulation since we consider it more general.

Remark: Before starting the model computation, one can notice that the mechanical model is compatible with our early conclusion, that a longitudinal tank motion will create sloshing while a vertical oscillation will not.

The main criterion when computing the equivalent model of the liquid oscillation in the container are the following [67]:

- The equivalent system must produce the same force and moment, under some

external excitation, as the actual system;

- The center of gravity G must remain the same for small oscillations;

- The equivalent system must preserve the equivalent masses and moments of inertia;

- The equivalent system must have the same modes of oscillations and produce the same damping force.

Therefore, corresponding to each sloshing mode we will choose an oscillating mass. Since the contribution to the resultant force and moment comes through the odd sloshing modes (see (2.89), (2.91), (2.96)), the mechanical model would incorporate oscillating masses corresponding to odd sloshing modes only.

Figure 2.16 shows a mass-pendulum model representing the liquid motion under horizontal acceleration C_0 acting upon the center of gravity of the tank and liquid. The oscillating masses, m_{n_i} are attached through a pendulum rod of length l_{n_i} and the pivot of the pendulum is placed at a distance L_{n_i} from the liquid center of gravity. A fixed mass m_0 is placed at a distance L_0 also from the liquid center of gravity. The introduction of the fixed mass is compulsory since not all the liquid in the tank is free to move but only a small amount of liquid on the free surface.

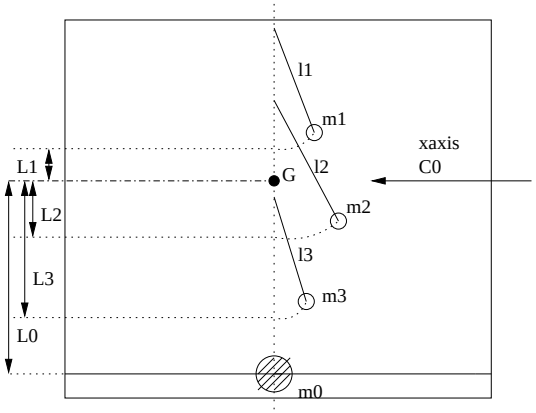

Figure 2.16: Mechanical model with one fixed mass and 3 sloshing masses, representing fuel sloshing under longitudinal excitation

2.3.4.2 Determination of parameters for the mass-pendulum model

Proposition 2.3.4. *The equivalent mass-pendulum model is composed of M equations:*

$$\ddot{\theta}_i + 2\xi_\theta \sqrt{\frac{g}{l_i}}\dot{\theta}_i + \frac{g}{l_i}\theta_i = -\frac{1}{l_i}C_0,\ i = 1 \cdots M \tag{2.103}$$

where θ_i is the angle of the i^{th} pendulum compared to its equilibrium position, $\xi_\theta = 0.001$ is the damping of the pendulum and l_i the length of the pendulum computed from

$$l_i = \frac{g}{\Omega_i^2} \tag{2.104}$$

where Ω_i is the angular frequency of the corresponding liquid sloshing mode.

Each mass-pendulum system is characterized by his mass m_i

$$m_i = \frac{8\rho bh}{\pi i} \tag{2.105}$$

and his position to the gravity center of the liquid in steady motion L_i

$$L_i = \frac{h}{2} - \frac{1}{\frac{\pi i}{a}\tanh(\frac{\pi i}{a}h)} + \frac{2}{\frac{\pi i}{a}\sinh(\frac{\pi i}{a}h)}. \tag{2.106}$$

Moreover, the mass-pendulum model contains a fixed mass m_0

$$m_0 = \rho abh - \sum_{i=1}^{M} m_i \tag{2.107}$$

situated at a distance L_0 from G

$$L_0 = \frac{1}{m_0}\left[\frac{\rho b a^3}{12} - \sum_{i=1}^{M} m_i L_i\right]. \tag{2.108}$$

Proof:

Step 1: l_i

The length of the pendulum, l_{n_i} is determined so that the angular natural frequency (which is equal to 2π times the natural frequency) of the pendulum is the same as

the corresponding liquid mode (Ω_i). Hence,

$$\Omega_i = \sqrt{\frac{g}{l_{n_i}}} \tag{2.109}$$

where $n_i \in \mathbb{N}^*$ is the pendulum number [2]. Therefore, from this last equation we compute the pendulum length (2.104). Note that a perfect approximation of the system is attained when choosing an infinite number of mass pendulum systems.

Step 2: m_i and m_0

The equation of motion of a pendulum under a horizontal acceleration C_0 [112], under the assumption of small oscillating angles for which $\sin(\theta_{n_i}) = \theta_{n_i}$ and $\cos(\theta_{n_i}) = 1$, is:

$$l_{n_i}\ddot{\theta}_{n_i} + g\theta_{n_i} = -C_0 \tag{2.110}$$

where θ_{n_i} is the oscillating angle taken from the equilibrium position.

Using this equation, we compute the total horizontal force generated by the mechanical model. The expression of the force is found using Newton's second law of mechanics $F_x^{mech} = ma$, where the m is the total mass of the system composed by the pendulum masses and by the fixed mass and the a is the total acceleration of the system.

The acceleration the system undergoes is a sum of two components, one component is generated by the pendulum free movement and the other component is the tank external acceleration C_0. The first component of the two accelerations, is found by writing the force equilibrium on the pendulum mass, when the connection point of the pendulum hinge is in steady motion (null external acceleration). Thus the horizontal acceleration is given only by the horizontal component of the force of gravity: $m_{n_i} g \sin(\theta_{n_i}(t))$. The force equilibrium then gives:

$$m_{n_i} g \sin(\theta_{n_i}(t)) = m_{n_i} l_{n_i} \ddot{\theta}_{n_i}(t).$$

Therefore, the total acceleration is $a = l_{n_i}\ddot{\theta}_{n_i}(t) + C_0$ and one can write the total

[2] Here we use the subscript n_i to differentiate the mechanical system from the corresponding sloshing mode. Once this relation is set, we will use for sake of simplicity, i instead of n_i

force F_x^{mech} generated by the mass pendulums movement:

$$F_x^{mech} = m_0 C_0 + \sum_{n_i=1}^{\infty} m_{n_i} C_0 + \sum_{n_i=1}^{\infty} m_{n_i} l_{n_i} \ddot{\theta}_{n_i}(t). \tag{2.111}$$

Imposing that the force generated by the mass pendulums is identical to the one generated by the liquid sloshing, ($F_x = F_x^{mech}$ from (2.89) and (2.111)), we compute the value of the fixed mass m_0 from (2.107), where the m_{n_i} are the masses of the pendulums and the product ρabh is the total mass of the liquid. Moreover, again from $F_x = F_x^{mech}$ we can also write:

$$\sum_{n_i=1}^{\infty} m_{n_i} l_{n_i} \ddot{\theta}_{n_i}(t) = 2\rho \sum_{i=1,3,5,\ldots}^{\infty} \frac{\ddot{r}_i(t)}{\Upsilon_i^2}. \tag{2.112}$$

From this last equation, since each sloshing mode is independent of the others, one can write for each odd mode:

$$\frac{m_{n_i} l_{n_i} \Upsilon_i^2}{2\rho} = \frac{\ddot{r}_i(t)}{\ddot{\theta}_{n_i}(t)} \tag{2.113}$$

which gives the dependency between the sloshing mode and the corresponding mass pendulum system.

The relation between n_i and i is that every liquid mode $i \in \{1, 3, 5, ...\}$ (as it can be seen from equation (2.77) the modes of liquid sloshing are only odd modes) is corresponding to a pendulum denoted $n_i \in \{1, 2, 3, ...\}$. Even if a perfect approximation comes only with $n_i \to \infty$ in real situations it is possible to truncate n_i at a certain natural number M.

As an example for $M = 3$ we can see that to the first sloshing mode $i = 1$ is corresponding a first pendulum ($n_i = 1$), to the third liquid mode $i = 3$ is corresponding a second pendulum ($n_i = 2$) and to the fifth liquid mode $i = 5$ is corresponding a third pendulum ($n_i = 3$).

Remark: Since the relation between the sloshing modes and the mass pendulum systems is well established, from now on, we will denote the mass pendulum systems by the subscript i instead of n_i in order to simplify the writing.

As mentioned before, we further make the assumption of small displacements of the pendulum above the equilibrium position ($tanh(\Upsilon_i h) \sim \Upsilon_i h$) and deduce from

(2.77):

$$\ddot{r}_i(t) = -\frac{4C_0 h}{a} - g\Upsilon_i^2 h r_i(t). \tag{2.114}$$

Using (2.114) and (2.110), the ratio between $\ddot{r}_i(t)$ and $\ddot{\theta}_i(t)$ becomes:

$$\frac{\ddot{r}_i(t)}{\ddot{\theta}_i(t)} = \frac{4hl_i}{a}\left(\frac{\frac{C_0}{g} + \frac{\Upsilon_i^2 a r_i(t)}{4}}{\frac{C_0}{g} + \theta_i(t)}\right) \tag{2.115}$$

which with (2.113) gives:

$$\frac{m_i \Upsilon_i^2 a}{8\rho h} = \frac{\frac{C_0}{g} + \frac{\Upsilon_i^2 a r_i(t)}{4}}{\frac{C_0}{g} + \theta_i(t)} \tag{2.116}$$

Analyzing the structure of both sides of equation (2.116), note that, for a given pendulum system, the left-hand side is constant number. Thus, the right-hand side must be a constant too (independent of $r_i(t)$, $\theta_i(t)$ for all $t \geq 0$). Since at the initial state the liquid is supposed at rest ($r_i(0) = 0$) and the pendulums in their vertical position ($\theta_i(0) = 0$), we conclude that the right side of the equation can be only equal to 1:

$$\frac{m_i \Upsilon_i^2 a}{8\rho b h} = \frac{\frac{C_0}{g}}{\frac{C_0}{g}} = 1.$$

Since the right-hand side of the equation is unitary, we obtain the following relation between free surface displacement and pendulum rotation:

$$\theta_i(t) = \frac{\Upsilon_i^2 a}{4} r_i(t),$$

and finally we can compute the value of pendulum mass m_i:

$$m_i = \frac{8\rho b h}{\Upsilon_i^2 a}. \tag{2.117}$$

where a simple replacement of Υ_i by his expression from (2.85) gives the value of each pendulum mass from (2.105).

Step 3: L_i and L_0

The distance between the center of gravity of the liquid in steady motion and the connection point of the pendulum hinge is denoted L_i (measured positive above the center of gravity). It will be computed using the equivalence of moments.

In the case of the mass pendulum system, the moment is computed, as in the case of the liquid sloshing, by multiplying the distance and the force $M = \overrightarrow{distance} \wedge \overrightarrow{force}$. Thus, the moment computed at the center of gravity is:

$$M_y^{mech} = m_0 L_0 C_0 + \sum_{i=1}^{\infty} m_i L_i C_0 + \sum_{i=1}^{\infty} m_i l_i L_i \ddot{\theta}_i \tag{2.118}$$

where the force created by the mass pendulum system (2.111) is multiplied by the distance corresponding to each pendulum system.

The two systems generate the same resultant moment. Thus, imposing that $M_y = M_y^{mech}$, one can write from (2.96) and (2.118):

$$m_i l_i L_i \ddot{\theta}_i(t) = 2\frac{\rho}{\Upsilon_i^2} \ddot{r}_i(t) \left[\frac{h}{2} - \frac{1}{\Upsilon_i \tanh(\Upsilon_i h)} + \frac{2}{\Upsilon_i \sinh(\Upsilon_i h)} \right]$$

Using the relation between $\ddot{r}_i$ and $\ddot{\theta}_i$ from (2.113), we get, $\forall i \in \mathbb{N}^*$

$$L_i = \frac{h}{2} - \frac{1}{\Upsilon_i \tanh(\Upsilon_i h)} + \frac{2}{\Upsilon_i \sinh(\Upsilon_i h)} \tag{2.119}$$

which is exactly the expression from (2.106), with Υ_i from (2.85).

Concerning the distance L_0 of the fixed mass, it is found comparing the terms depending on the exterior acceleration C_0 from the equations (2.96) and (2.118):

$$m_0 L_0 C_0 + \sum_{i=1}^{\infty} m_i L_i C_0 = \frac{\rho C_0 a^3 b}{12}.$$

After eliminating the external acceleration we get equation (2.108).

Step 4: Mass-pendulum equation

The state-space representation of the tank with liquid is straightforward from equation (2.110). Moreover, as stated earlier, one of the advantages of the use of mechanical models is the easiness in considering the inherent damping. The damping ξ_θ can be easily introduced in the pendulum representation (2.110) to obtain equation (2.103). We did not find a methodology to measure the damping, so we fixed it at 0.001 for all the M modes, which represents the viscous coefficient of the water at normal temperature of around 20°C.

This last issue concludes the proof of Proposition 2.3.4. □

The choice of the state-space vector for the liquid sloshing, as in the case of the

plate, is subject to several solutions. Finally, we choose the state-space vector as

$$X_\theta = \begin{pmatrix} \dot{\theta}_1 & \sqrt{\frac{g}{l_1}}\theta_1 & \cdots & \dot{\theta}_i & \sqrt{\frac{g}{l_i}}\theta_i & \cdots & \dot{\theta_M} & \sqrt{\frac{g}{l_M}}\theta_M \end{pmatrix}^T \tag{2.120}$$

instead of $\begin{pmatrix} \dot{\theta}_1 & \theta_1 & \cdots & \dot{\theta}_i & \theta_i & \cdots & \dot{\theta_M} & \theta_M \end{pmatrix}^T$. This choice is done in order to obtain a better conditioning of the system.

Using the state-space vector (2.120), the dynamic equation, for the general case of an input u_{acc}, is given by the following proposition:

Proposition 2.3.5. *The dynamic equation for the mass-pendulum system is*

$$\dot{X}_\theta = A_\theta X_\theta + B_\theta u_{acc} \tag{2.121}$$

where the matrix A_θ computed from (2.103) for each i satisfies

$$A_\theta = \begin{pmatrix} A_{\theta_1} & 0 & \cdots & 0 \\ 0 & A_{\theta_2} & \cdots & 0 \\ & & \cdots & \\ 0 & 0 & \cdots & A_{\theta_M} \end{pmatrix} \tag{2.122}$$

with $A_{\theta_i} = \begin{pmatrix} -2\xi_\theta\sqrt{\frac{g}{l_i}} & -\sqrt{\frac{g}{l_i}} \\ \sqrt{\frac{g}{l_i}} & 0 \end{pmatrix}$ *and the control matrix B_θ is given by:*

$$B_\theta = (b_{\theta_1}, 0, ..., b_{\theta_i}, 0, ..., b_{\theta_M}, 0)^T \tag{2.123}$$

where $b_{\theta_i} = \begin{pmatrix} -\frac{1}{l_i} \\ 0 \end{pmatrix}$ *and $u_{acc} = C_0$ as the control variable.*

With this last proposition the equivalent mechanical model is set. Based on the method of calculus, the equivalent force and moment generated by the equivalent model is identical to the one generated by the sloshing of liquid. Besides, as one can observe from Proposition 2.3.4, all the parameters of the mass pendulum systems: length, mass, position comparing to the center of gravity are independent from the excitation parameters (time, frequency, amplitude).

Conclusion: In this section we computed the model of the tank and liquid sloshing. In order to easily manipulate the infinite dimensional model of the liquid we made an analogy with a mechanical mass pendulum system. Finally, a state-space representation of the sloshing behavior is computed.

2.4 Complete model representation

2.4.1 Infinite dimensional coupling

As presented earlier in the introduction, the idea in computing the complete model of the entire structure is first to build one model for the plate and one for the tank with liquid and second to combine them by studying the mutual interactions between the two separate models. Therefore, as shown, in Section 2.2.2 we computed the infinite dimensional model of the rectangular plate, given by the equation (2.27) and in Section 2.3.3 we computed the infinite dimensional model of the tank with liquid, given by the equation (2.67) and (2.68) for the liquid movement. The coupling is the most difficult and a key point in our work.

For further details concerning the coupling between a sloshing liquid and a flexible structure one can check [123] or [103]. Thus, to the best of our knowledge there are no other works that will detail the coupling between a flexible plate and a tank with sloshing liquid, in both infinite and in finite dimension.

In order to complete the model we first analyze the influence of the liquid sloshing on the plate movement and second we analyze the influence of the plate bending on the sloshing of liquid.

2.4.1.1 Influence of the liquid sloshing on the plate movement

The liquid sloshing is sensed by the plate as an external moment which, along with the piezoelectric actuators, will contribute to the plate bending. As it can be seen from the partial derivative equation of the plate (2.27), on the right-hand side of the equation, we have m_y and m_z which are the external moments along the y and z-axis:

We recall this equation here:

$$m_s \frac{\partial^2 w}{\partial t^2} + \zeta(w)\frac{\partial w}{\partial t} + YI_s\Delta^2 w = \frac{\partial^2 m_y}{\partial y^2} + \frac{\partial^2 m_z}{\partial z^2}$$

where w is the plate displacement from its equilibrium position. The other variables were detailed before in (2.27).

These moments are generated by the piezoelectric actuators glued to the plate and by the sloshing of the liquid:

$$m_y = m_y^a + m_y^f \ , \ m_z = m_z^a + m_z^f$$

where m_y^a and m_z^a are the moments delivered by the actuators and m_y^f and m_z^f are delivered by liquid sloshing along the y and z axis. Furthermore, the moments generated by liquid sloshing were computed in Proposition 2.3.3 for the moments along the y-axis and z-axis.

2.4.1.2 Influence of plate deformation on the liquid sloshing

The plate deformation is sensed by the liquid sloshing as an external acceleration that disturbs the liquid. The study of the liquid subject to an external acceleration is given by the linear equation of motion of the liquid (2.67):

$$\frac{\partial \phi}{\partial t} + \frac{p}{\rho} + g(z-h) - C_0 x = 0$$

where C_0 is the external acceleration.

In our case, this acceleration is generated by the plate bending. Therefore, it can be expressed as a two time derivative of the plate deformation $w(y,z,t)$ computed in the gravity center of the tank in steady motion $G = (y_G, z_G)$:

$$C_0 = \ddot{w}(y_G, z_G, t) = \sum_{k=1}^{\infty} \eta_k(y_G, z_G)\ddot{q}_k(t) \tag{2.124}$$

Based on the issues detailed earlier in this chapter, we can write the complete PDE model of the system. This model though, is not implementable on the experimental device. Therefore, in the next section, we express the coupling in finite dimension and we explicitly compute all the new matrices entering the model formulation.

2.4.2 Finite dimensional coupling

In this section we will write the finite dimensional approximation of the complete system. As detailed earlier, we first computed PDE models for the plate and for the sloshing liquid in the tank and second we made finite dimensional approximations of two different kinds (modal for the plate and mechanical for the sloshing) to construct state-space models. Now, we also need to study the influence of each model

approximation onto the other.

Therefore, we consider again the two separate cases: the influence of the liquid sloshing on the deformation of the plate and the influence of the plate deformation on the tank filled with liquid up to an arbitrary level.

Before detailing these issues let us remind that in Section 2.2.3 we computed the state-space approximation of the rectangular plate undergoing deformation (by considering only the first N deformation modes) while in Section 2.3.4.2 we computed the state-space approximation of the tank with liquid (by making an analogy with M mass pendulum system corresponding to the first $2M-1$ odd sloshing modes).

Let us now detail the coupling issue.

2.4.2.1 Liquid sloshing influence on the rectangular plate

The liquid sloshing is sensed by the rectangular plate as an external perturbation which comes by the mean of an external moment. Moreover, we suppose that the total moment generated by the liquid sloshing is concentrated in a small square area around the gravity center G (measured in steady motion) of the tank with liquid. This area can be geometrically described by the position of the opposite corners (y_{1G}, z_{1G}) and (y_{2G}, z_{2G}).

If we denote $\mathcal{M}_{\theta p}$ the moment generated by the M considered mass-pendulums system, his expression can be written from (2.118) by canceling the external acceleration of the tank:

$$\mathcal{M}_{\theta p} = \sum_{i=1}^{M} m_i L_i l_i \ddot{\theta}_i$$

where the fixed mass denoted m_0 was not taken into account since is not creating any sloshing.

Further on, we can notice that the variable $\ddot{\theta}_i$ can be expressed using the state-space vector of the pendulum approximation given by (2.120). Thus, the previous expression of the moment can be equivalently written:

$$\mathcal{M}_{\theta p} = \sum_{i=1}^{M} \begin{pmatrix} m_i L_i l_i & 0 \end{pmatrix} \begin{pmatrix} \ddot{\theta}_i \\ \sqrt{\frac{g}{l_i}}\dot{\theta}_i \end{pmatrix}. \tag{2.125}$$

This equation can also be further simplified if we notice that the column vector is

the time derivative of the state-space vector X_θ of the liquid:

$$\dot{X}_\theta = \begin{pmatrix} \cdots \\ \ddot{\theta}_i \\ \sqrt{\frac{g}{l_i}}\dot{\theta}_i \\ \cdots \end{pmatrix}.$$

The last expression (2.125) becomes, developing the sum:

$$\mathcal{M}_{\theta p} = \begin{pmatrix} m_1 L_1 l_1 & 0 & \cdots & m_i L_i l_i & 0 & \cdots & m_M L_M l_M & 0 \end{pmatrix} \dot{X}_\theta$$

or again

$$\mathcal{M}_{\theta p} = \begin{pmatrix} m_1 L_1 l_1 & 0 & \cdots & m_i L_i l_i & 0 & \cdots & m_M L_M l_M & 0 \end{pmatrix} A_\theta X_\theta, \tag{2.126}$$

the dynamic matrix A_θ being computed from (2.122).

We make the same analogy as in the case of the moment generated by the piezoelectric actuators (see Section 2.2.3.2). We consider that the moment generated by liquid sloshing is being sensed by the plate as an external perturbation.

Since the moment is concentrated around the gravity center, we use again the Heaviside step H from (2.57) to compute it.

As we did for the case of control actuator in Section 2.2.3.2, we integrate on the surface where the moment is different than zero and we get the $2N$ components $a_{\theta p_k}$ of the perturbation matrix denoted $A_{\theta p}$:

$$\begin{aligned} a_{\theta p_k} \quad = \quad & K_{\theta p}(Y'_{i_k}(y_{2G}) - Y'_{i_k}(y_{1G})) \int_{z_{1G}}^{z_{2G}} Z_{j_k}(z)dz \\ & + K_{\theta p}(Z'_{j_k}(z_{2G}) - Z'_{j_k}(z_{1G})) \int_{y_{1G}}^{y_{2G}} Y_{i_k}(y)dy \end{aligned} \tag{2.127}$$

where $a_{\theta p_k} \in \mathbb{R}^{1\times 2M}$ and the matrix

$$K_{\theta p} = \begin{pmatrix} m_1 l_1 L_1 & 0 & \cdots & m_i l_i L_i & 0 & \cdots & m_M l_M L_M & 0 \end{pmatrix} A_\theta$$

is computed from (2.126). As in (2.46), i_k, j_k express the deformations of the two considered beams of the plate deformation (see Section 2.2.3 and more precisely equation (2.32)).

The total perturbation matrix is finally written:

$$A_{\theta p} = \begin{pmatrix} a_{\theta p_1} \\ 0 \\ \vdots \\ a_{\theta p_k} \\ 0 \\ \vdots \\ a_{\theta p_N} \\ 0 \end{pmatrix} \in \mathbb{R}^{2N \times 2M} \tag{2.128}$$

where the lines $a_{\theta p_k}$ are computed from (2.127).

The state-space representation of the plate (2.63) can finally be rewritten taking into account also the influence of the liquid sloshing and becomes:

$$\begin{cases} \dot{X}_p = A_p X_p + B_p u + A_{\theta p} X_\theta \\ y = C_p X_p \end{cases} \tag{2.129}$$

2.4.2.2 Plate deformation influence on tank liquid sloshing

The tank senses the plate movement as an external horizontal acceleration, superposed on the tank own acceleration created by liquid movement without external influence.

The mass pendulum systems were already analyzed under an external acceleration C_0 (see (2.110) or Figure 2.16). Now, we express this acceleration as a two times derivative of the plate deformation $w(y, z, t)$ at the tank gravity center (since the external acceleration acting on the mechanical systems is located there). Therefore we get:

$$C_0 = \ddot{w}(y_G, z_G, t) = \sum_{k=1}^{N} \eta_k(y_G, z_G) \ddot{q_k}(t)$$

where y_G, z_G are the coordinates of the gravity center G along the y and z-axis.

Furthermore, for sake of simplicity, the terms not depending on the plate kinematic parameters are introduced in a vector denoted K_G. Finally we get:

$$C_0 = K_G \begin{pmatrix} \ddot{q_1}(t) & \omega_1 \dot{q_1}(t) & \cdots & \ddot{q_k}(t) & \omega_k \dot{q_k}(t) & \cdots & \ddot{q_N}(t) & \omega_N \dot{q_N}(t) \end{pmatrix}^T \tag{2.130}$$

where

$$K_G = \begin{pmatrix} Y_{i_1}(y_G)Z_{j_1}(z_G) & 0 & \cdots & Y_{i_k}(y_G)Z_{j_k}(z_G) & 0 & \cdots & Y_{i_N}(y_G)Z_{j_N}(z_G) & 0 \end{pmatrix}$$

and the column vector is exactly the derivative of the state-space vector of the plate X_p as it can be seen from (2.43).

Thus, the latter equation can be written in a more compact form:

$$C_0 = K_G \dot{X}_p \tag{2.131}$$

or again using (2.63),

$$C_0 = K_G A_p X_p + K_G B_p u. \tag{2.132}$$

Using the equation (2.132) into the state-space representation of the mass pendulum systems (2.121) we get the complete state-space representation of the mass pendulum systems connected to the plate:

$$\dot{X}_\theta = A_\theta X_\theta + B_\theta (K_G A_p X_p + K_G B_p u) \tag{2.133}$$

where all the matrices are detailed in Section 2.2.3 and in Section 2.3.4.2.

2.4.2.3 Compact writing of complete model

The state-space representation of the complete model can be written in a compact form by using equations (2.129) and (2.133). By taking the state-space vector of the complete system as a combination of the plate state-space vector and liquid state-space vector

$$X = \begin{pmatrix} X_p \\ X_\theta \end{pmatrix}$$

the complete model written for N modes of the plate and $M \neq N$ mass pendulum systems is:

$$\begin{cases} \dot{X} = \begin{pmatrix} A_p & A_{\theta p} \\ A_{p\theta} & A_\theta \end{pmatrix} X + \begin{pmatrix} B_p \\ B_{p\theta} \end{pmatrix} u \\ y = \begin{pmatrix} C_p & \mathbf{0} \end{pmatrix} X. \end{cases} \tag{2.134}$$

where $A_{p\theta} = B_\theta K_G A_p$, $B_{p\theta} = B_\theta K_G B_p$ and $\mathbf{0}$ denotes null matrix because the output variable is the piezoelectric sensor which is not influenced in any way by the liquid sloshing.

In this section we first expressed the coupling between the PDE plate model and the PDE liquid model. This is done by studying the influence of the plate bending on the liquid sloshing and *vice-versa*. Based on this, an approximation of the coupling was then conducted.

2.5 Conclusion of the chapter

In this chapter, the complete model of the experimental device was computed. It was first wrote in infinite dimension and then approximated under the shape of a state-space representation. The final expression of the model is given by (2.134).

This model will be used in Chapter 4 in order to compute different types of controllers that will be used to attenuate the vibrations of the structure.

Chapter 3

Controller synthesis - Theoretical approach

The model of the structure was previously computed in Chapter 2 and is written as the system of equations (2.134).

In this chapter we detail some preliminary techniques in order to effectively compute the model, along with some details for the application of different control methods. We propose two types of control starting from the state-space representation: first, a classical pole placement control coupled with a Luenberger observer and second, a frequency domain H_∞ control, designed with meeting frequency-domain performance criteria.

In this chapter we also detail some of the theoretical considerations regarding the problem of active control of vibrations for our experimental setup imitating a plane wing (see [4] for more details about airplane characteristics and control). The experimental plant is a flexible structure thus our control problem can be considered as a part of the complex class of active control problems of flexible structures. One can read [82] for different control strategies that can be applied on flexible systems, [131] for a controller that takes into account the nonlinear behavior of these systems, [17] for a feedback controller or again [14], [12], [126], [15], [88] where the robust H_∞ control of flexible systems is detailed. In our case, the objective is to attenuate the vibrations of the structure while maintaining some predetermined performances. More precisely, the issue is to attenuate the mode vibration while the structure (thus the dynamic) is affected by perturbations.

3.1 Energy computation

Before starting the control procedure, an important step is to chose the number N of plate modes and the number M of mass pendulum systems we will use for computing the analytical model. As it will be proven latter in this paragraph, the influence of the sloshing modes on the total plant dynamics is much smaller than the influence of the plate's bending modes. We will indeed see latter that the magnitude of the sloshing modes is very small comparing to the one of the plate modes. Therefore, the most important choice is the one of the appropriate number of plate modes. Nevertheless, the method will be detailed for the whole coupled system, rectangular plate and cylindrical tank together.

Several factors must be taken into consideration. First of all, we should insure that the number of modes we select give a close representation of the experimental setup. Since the experiment corresponds theoretically to an infinite number of modes, the truncation we perform should gather the largest number of modes. But this is not relevant in practice since in this case the control cannot be computed due to the very large dimension of the system.

Considering the plate, since we want to control flexion and torsion movements, it is natural to consider both flexion and torsion modes in our truncated model. Even in this case, we need to find how many torsion and flexion modes have to be taken into consideration in order to have a good approximation. For example one can check the work [114] where, on the same experimental setup as ours, the author chooses only one flexion mode and only one torsion mode of the plate with no sloshing mode. Another example can be found in the works [81] and [133] where the authors choose *a priori* the number of considered modes.

In our case, even though the *a priori* choice is still possible, we propose also another method based on the energetic contribution of each mode of the model. The basis for the energy calculation used in this approach can be read in [146, Chapter 4.6].

The first point is to consider that the system is in his diagonal representation. Even though the plate modes and the liquid sloshing modes are decoupled (because their dynamic matrices are in a diagonal representation due to the decoupled modes hypothesis), the coupled dynamic matrix is not diagonal due to the coupling between the plate and the tank, as detailed in Section 2.4. This last issue can be easily noticed by considering only the final equation of the complete system (2.134). If the system is diagonal, the controllability and observability Gramians have a special shape which

will make possible the energy computation (see equation (3.3) below).

Consider the total output energy e_T of our system denoted $\Sigma(s)$ of dimension $\mathbb{R}^{(2M+2N)\times(2M+2N)}$ represented by equation (2.134). When the system is excited by a Dirac unit impulse on his input, the energy can be written as:

$$e_T = ||y(t)||_2^2 = ||\Sigma(s)||_2^2. \tag{3.1}$$

Moreover, using the observability Gramian W_o and the controllability Gramian W_c, this expression can be rewritten as in [146, Chapter 4.6]:

$$e_T = \text{Trace}\{BW_oB^T\} = \text{Trace}\{CW_cC^T\} \tag{3.2}$$

where the B and C are the control and output matrix of the system written in the diagonal state-space representation.

We suppose that the controllability Gramian has the following shape:

$$W_c = \begin{bmatrix} W_{11} & \cdots & W_{1j} & \cdots & W_{1(2M+2N)} \\ \cdots & & & & \\ W_{i1} & \cdots & W_{ij} & \cdots & W_{i(2M+2N)} \\ W_{(2M+2N)1} & \cdots & W_{(2M+2N)j} & \cdots & W_{(2M+2N)(2M+2N)} \end{bmatrix} \tag{3.3}$$

where $W_{ij} = W_{ij}^T$ since the dynamic matrix is diagonal.

Since the system is written in a diagonal basis, and the dynamic matrix has only complex conjugate pairs of eigenvalues, each element of the controllability Gramian verifies an autonomous Lyapunov equation:

$$A_iW_{ij} + W_{ij}A_j^T + B_iB_j^T = 0 \tag{3.4}$$

where $A_i \in \mathbb{R}^{2\times2}$ and $A_j \in \mathbb{R}^{2\times2}$ are the dynamic matrices corresponding to the i^{th} and j^{th} modes.

The output contribution of each mode, can be computed by substact from the total energy e_T the energy that the system would have had if this mode was uncontrollable. Therefore, the methodology we are using is simple: we consider that for a specific mode of index k, the corresponding control matrix B_k (see (3.4)) is equal to zero. In this case we notice that, the newly computed Gramian matrix, denoted W_{c_k} in order to emphasize the uncontrolled mode k, has the elements containing the k^{th} mode, equal to zero.

If we denote the output energetic contribution of the k^{th} mode by E_{o_k}, its value

can be written:

$$E_{o_k} = e_T - \text{Trace}\{CW_{c_k}C^T\} \tag{3.5}$$

For us, it is more convenient to compute the modal energetic contribution instead [134]. This is easily done by replacing the output matrix C in equation (3.5) by the identity matrix I of dimension $(2M + 2N) \times (2M + 2N)$. Therefore the modal energetic contribution of the k^{th} mode is:

$$E_k = e_T - \text{Trace}\{\text{I}W_{c_k}\text{I}^T\} \tag{3.6}$$

Finally, using a simple percentage operation $\frac{E_k}{e_T}100$ we can compute the energy contribution of the k^{th} mode comparing to the total amount of energy of the plant.

In our case, we compute analytically the state-space model of the plate using a large number of modes (14 modes for the structure). We then use this methodology and equation (3.6) to compute the energy contribution of each mode. Finally, we sum the energy of all the modes until more than 90% of the total plate energy is reached. Thus, the considered modes describe well the plate behavior in terms of energy. The correct amount of modes is set. See below in Section 4.2 of Chapter 4 for the results of this algorithm on the experimental device.

3.2 Pole placement and full state observer

Using the state-space representation (2.134), we now aim at computing a controller using the pole placement method. As seen from Figure 1.1, there are two piezoelectric actuators in the system input and two piezoelectric sensors in the system output. Actually, they are not both used as inputs and outputs of the system. One actuator is used for system input and one sensor for system output. The other actuator glued on the plate is used, as it will be shown latter in Section 3.3 below, as a possible input for applying perturbations to the system. The other sensor is used only for further complementary measurements, when needed. Thus, the system we consider is a single input single output system (SISO).

Pole placement control

The pole placement method is well known in control system theory. Our purpose here is not to offer a detailed presentation of the method but just to give a few details concerning the implementation of the method in our case. For further details

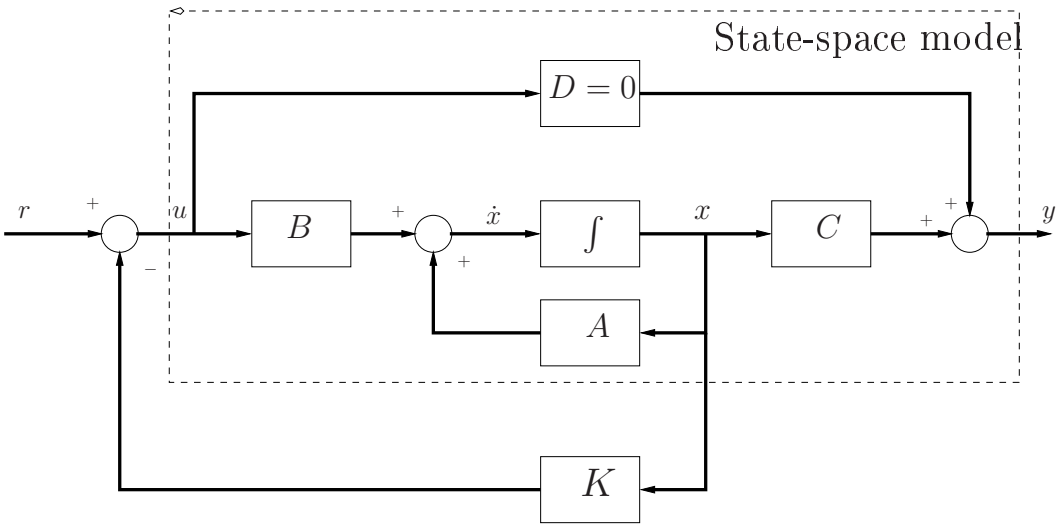

Figure 3.1: State feedback control

about state-feedback and pole placement coupled with observer construction one can check for example the references [9], [57], [77], [143] among others. For a feedback control implementation on a flexible structure, one can see [89] for example. The pole placement method gives the user the possibility to choose himself the location of the closed-loop system poles, therefore allowing the possibility of placing them at some predetermined locations. Although this method has some drawbacks when considering very complex systems, it is quite good for our case and may be seen as an introduction to the control of more complex systems.

Usually, the state-space design control methods, such as the pole placement in our case, are more easily performed using a full or partial state feedback. In the case of the state feedback, the control action is achieved by feeding back a linear combination of the system's states through a matrix (or gain depending on the feedback type) usually denoted K. The diagram of the state feedback control is depicted in Figure 3.1, where the different blocks are exactly the ones from the state-space representation (2.134).

Let us consider a state-space representation of a $2M + 2N$ dimension linear time invariant (LTI) system, written in the compact standard form:

$$\begin{cases} \dot{x}(t) &= Ax(t) + Bu(t) \\ y(t) &= Cx(t), \end{cases} \tag{3.7}$$

where the first equation describes the dynamic of the system and the second equation the measured output. The values M and N stand respectively for the number of

plate modes and mass pendulum systems. The physical meaning and the dimensions of y and u are presented in Section 2.4.2.3 of Chapter 2. Furthermore, we assume the system is causal, and therefore the usual feed-forward matrix is zero.

Using the feedback law, the control signal can be written

$$u(t) = -Kx(t) + r(t)$$

where $x(t)$ is the state-space vector of the system and $r(t)$ is a reference signal. Two different cases can be found for the reference signal. It can be different from 0 and variable in an unstructured manner. In this case we need the system output to track rapidly, for a specific class of systems, this reference signal. The other possibility is when the reference vanishes ($r(t) \equiv 0$). In this case, the controller generates a certain command to the plant based on the error between the system reference r and the system measured output y. The goal in this case is to generate a control that first will rapidly and smoothly take the values of the system output to the value of the reference (or set point) and second will maintain the reached value in the presence of some external disturbances. In this case the control system problem is a regulation problem and the controller is called a regulator. Afterward, we place ourselves in this type of control problem. Taking this last issue into account, the earlier equation becomes:

$$u(t) = -Kx(t). \tag{3.8}$$

Replacing this last equation into the dynamic representation (3.7), we obtain the closed-loop representation of the system with feedback:

$$\dot{x}(t) = (A - BK)\, x(t). \tag{3.9}$$

In this case, all the closed-loop poles of the system can be placed by selecting the value of the K matrix such that the eigenvalues of $(A - BK)$ are at the desired pole values. This can be done only if the open-loop system is fully controllable, that is to say the rank of the controllability matrix is the same as the dimension $2M + 2N$ of the dynamic matrix A.

The controllability of a system is a key concept in the computation of system control laws since it tells if the implementation of classical control laws will be of some result or not. A system is said to be controllable if any initial state x_0 at any initial time t_0 can be moved to any other desired state $x_f = x(t_f)$ in a finite time

interval $t_f - t_0 > 0$ and by applying an admissible control function. The direct result of this formulation is the definition of the controllable system using the controllability matrix Q_c defined as in [139] by:

$$Q_c = \begin{pmatrix} B & AB & \cdots & A^{(2M+2N)-1}B \end{pmatrix}. \tag{3.10}$$

As a conclusion, the controllability of the system is assured, meaning that the matrix pair (A, B) is controllable, if $\text{rank}(Q_c) = 2M + 2N$.

Finally, if the system is fully controllable, we choose the value of the closed-loop poles, which are the eigenvalues of $(A - BK)$, and then we compute the matrix K. There are different methods for computing this matrix and for further details one can check reference [101]. For example, the direct substitution method combined with the computation of the coefficients of like powers can be used, or again the Ackermann's formula (see [99]). Another elegant way is to write the system in the controllable canonical form, using an adequate transformation matrix, and then simply compute each element of the K matrix by simple subtraction operations.

Observer design

The first assumption when designing a state feedback control is that all the system states gathered in the state-space vector $x(t)$ are known, and thus they can be used for the feedback law. In practice thus, this is only sometimes, but mostly never, true. There are many reasons. One first reason may be simply from the impossibility to measure some of the system states, either because of their very large quantity or because of the great cost that will be needed for specialized sensors. Another reason may be just simply the impossibility to measure some system states since they have no physical meaning or because the noise in the measurements is too large and therefore it gives a faulty measurement.

A straightforward class of solutions are the observers (or estimators). They were first introduced by Luenberger [84] and are defined as a system which (see [139]):

- is intended to approximate the state vector x of another system by means of a vector $\hat{x}$;
- has at its inputs the inputs and available outputs of the latter system.

The observer can be either a Luenberger observer (see [84]), if the signal-to-noise ratios are sufficiently high (thus the system can be treated as deterministic) or a

Kalman filter (see [68]) if the signal-to-noise ratios are not very high. In our case though, we consider the system deterministic. Therefore we will further use Luenberger observers.

Moreover, since we do not have information about any of the parameters of the state-space vector, we need to reconstruct all the state-space vector x of the system. In this case the state-space vector of the observer becomes identical to the approximated state-space vector of the plant $\hat{x}$. This observer is called full state Luenberger observer and some steps regarding his construction are detailed in the following lines.

Before starting the controller computation, we suppose that there is no additive noise in the state equation or in the measurements and controls. Using this assumption, we think of estimating the entire state-space vector of the LTI system using only the output and control measurements. The error between the estimated state $\hat{x}$ and the true state should become minimal. There are several ways of defining the minimal error [99], either as the minimum square error, minimum absolute error, etc., but in our case the estimation error is defined as:

$$e(t) = x(t) - \hat{x}(t). \tag{3.11}$$

Therefore, as stated earlier, the constructed observer should satisfy $e(t) \underset{t\to+\infty}{\longrightarrow} 0$.

The main idea in the observer construction is to choose a predetermined shape for the observer:

$$\dot{\hat{x}}(t) = F\hat{x} + Gy(t) + Hu(t) \tag{3.12}$$

where $y(t)$ and $u(t)$ are the measurement output and the control input of the real plant (3.7). The vector $\hat{x}$ has the same dimension as the state-space vector x since the observer is a full state observer. Furthermore, the matrix F is a square matrix of dimension $(2M+2N)\times(2M+2N)$ while G and H are in $\mathbb{R}^{(2M+2N)\times 1}$ since y and u are scalar measures.

Putting the dynamic equations (3.7) and (3.12) in the error equation (3.11) we obtain

$$\dot{e}(t) = \dot{x}(t) - \dot{\hat{x}}(t) = Ax(t) + Bu(t) - (F\hat{x} + Gy(t) + Hu(t))$$

or again using the measured output equation from (3.7)

$$\dot{e}(t) = Fe(t) + (A - GC - F)\,x(t) + (B - H)\,u(t). \tag{3.13}$$

Furthermore, we want this error to be independent both of the control law we are considering and of the state-space vector we want to reconstruct. Therefore, we need it to tend asymptotically to zero regardless these issues. This means that it is compulsory to have $H = B$ and $F = A - GC$.

Moreover, the G matrix is computed using the pole placement method detailed in the previous part. From the control theory we know that we can find the G matrix, that will arbitrarily place the poles of $A - GC$ at the desired locations, but only if the system is observable.

The observability of a specific state or of the whole system is a key concept in the computation of observers. In this case the output has all the components of the state, therefore, it is possible to estimate all the system's states using only the input and output of the system. Moreover, the concept of observability is mathematically dual with the concept of controllability presented earlier.

A system is said to be observable if any initial state $x(t_0)$ can be determined after a finite time interval $t - t_0$ from the measurement history $Y(t) = \{y(\tau), t_0 \leq \tau < t\}$. Thus, the whole vector x can be computed given the uniqueness of the initial state (see [139]).

Using the observability test matrix Q_o:

$$Q_o = \begin{pmatrix} C \\ CA \\ \vdots \\ CA^{(2M+2N)-1} \end{pmatrix}, \tag{3.14}$$

the observability of the system can be written: the system (3.7) is fully observable (or the matrix pair $(A; C)$ is said to be observable), if the observability matrix has full rank: $\text{rank}(Q_o) = 2M + 2N$.

Separation principle

Until now we treated separately the two issues, observer design and state feedback control design, without taking into consideration the influence of one to the other. Actually, we considered them to be completely separate and we did not check if there is, or not, a reciprocal influence of their dynamics. But, as it can also be seen from Figure 3.2, they can not be treated separately since the feedback law uses the estimated system state since the real state vector is completely unknown.

It can be easily proven that, in our case, when the reference signal is equal to zero,

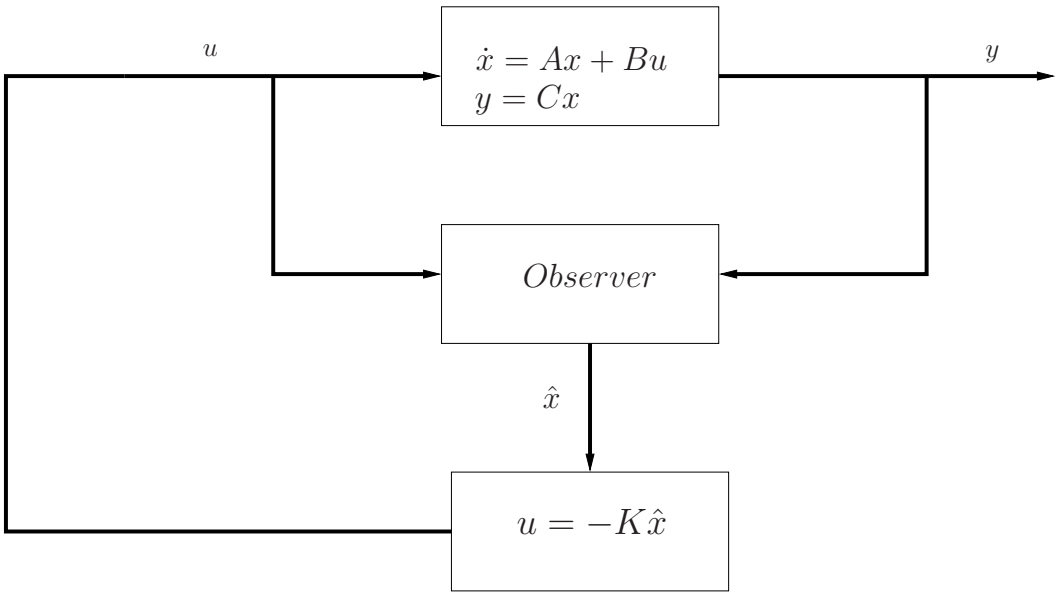

Figure 3.2: Feedback control law and observer

using (3.9) and (3.13) we can write $\forall t \geq 0$:

$$\begin{cases} \begin{pmatrix} \dot{x}(t) \\ \dot{e}(t) \end{pmatrix} = \begin{pmatrix} A - BK & BK \\ 0 & A - GC \end{pmatrix} \begin{pmatrix} x(t) \\ e(t) \end{pmatrix} \\ y(t) = \begin{pmatrix} C & 0 \end{pmatrix} \begin{pmatrix} x(t) \\ e(t) \end{pmatrix}. \end{cases} \tag{3.15}$$

Computing the characteristic equation of the system (3.15), we obtain:

$$\psi(s) = \det \begin{bmatrix} s\mathrm{I} - (A - BK) & -BK \\ 0 & s\mathrm{I} - (A - GC) \end{bmatrix} = 0$$

and since the system is block triangular, the characteristic equation becomes

$$\psi(s) = \det[s\mathrm{I} - (A - BK)] \det[s\mathrm{I} - (A - GC)] = 0.$$

This last equation indicates clearly all the poles of the closed-loop system with the observer. They are only the poles of the plant that result from the computation of the feedback gain K and the desired observer poles, chosen when computing the matrix G. This is called the principle of separation of estimation and control (or shortly separation principle or deterministic separation principle [15], [104]). Therefore, the optimal feedback controller can be solved by separately design an optimal observer,

for the state-space system, which will feed the optimal deterministic controller.

Some practical precautions have to be taken while choosing the poles. First of all, we would like the estimator error to vanish as quickly as possible so that the feedback law becomes in reality $u = -Kx$ and not $u = -K\hat{x}$. In order to do this, the observer poles will be chosen so that they are faster than those of the system we are estimating. Hence the observer will be delivering a faster response. This means that the smallest chosen pole (in absolute value) of the observer will need to have its magnitude considerably larger than the value of the smallest system pole. At the same time, we need to be careful since very large observer poles will imply a very fast response from the observer. This suggest that it will not follow only the system but also the noise of the ignored measurements. The same rule applies also in the case of the feedback control. Here, the observer poles must be chosen faster that the closed-loop system poles. There are different methods in the literature concerning how fast the observer poles have to be in comparison to the feedback poles (see [9] or [128]), but the criteria used are only empirical. In spite of this, we state that we can not *a priori* impose a certain amount since this basically depends on the system under consideration.

It is well know that only the real part of the complex eigenvalues influences the response time [9]. In our case we observe that choosing all the feedback poles with their real part larger than the real part of the open-loop poles is a complicated issue. This is due to the voltage delivered by the feedback controller which is exceeding the actuator amplitude limitations.

Further details about the implementation of the state feedback law, along with tests on the experimental device are given later in Section 4.4 of Chapter 4.

3.3 H_∞ controller

When considering the problem of active control of flexible structures, the most employed approach is the one using H_∞ theory. This is mainly due to the fact that, in the control problem, many issues usually need to be taken into account. Let us detail these issues for our case. First, since the modes we consider are the most energetic ones (see Section 4.2), the controller has to attenuate especially the vibrations of these ones. Second, the controller needs to attenuate vibrations in spite of model mismatching or uncertain description of some physical phenomena. Third, the dynamic of high frequencies, which has been neglected in the model computation, needs

also to be taken into account. Finally, our purpose is to see how the system reacts to exterior perturbations, thus the controller must be robust enough in order to take this specification into account. Based on these issues, the H_∞ approach seems to be the most natural one.

The work in the field of robust H_∞ control is very dense. The purpose of this paragraph is not to give a fully detailed presentation of the theory but just to give some pointy details and to focus on the actual implementation of the control to our setup. For a complete overview of the method, one can check the first works [51] or [145]. For a more practical approach, one can read references [12], [59] or [85] where implementation methods are carried out. The specific case of H_∞ control on flexible structures can be checked in [5], [37], [69], [88], [135] among others.

When computing the model of a flexible structure coupled with a liquid flow, numerous sources of errors may exist. For instance, we can cite the damping of the liquid sloshing which in our case is chosen constant for all modes and which in reality is not. Another example we can mention concerns the clamped side of the plate which we considered to be perfectly fixed. In reality this is not always true, and each small movement of the clamped side can change the value of the frequency and the modes shape. Finally, and probably the most important source of errors to our knowledge, is the contact between the tank and the rectangular plate or the perfect centering of the tank to the plate. The contact is assumed to be perfectly rigid during the modeling phase but in reality, we can observe that it is not. Furthermore, experiences on the experimental device show that the system behavior is different based on the tank being perfectly centered or not (decreases in the amplitude of the first flexion mode of the plate are visible if the tank is not perfectly centered, especially when a large amount of liquid is considered).

This gap between the dynamic model and the actual experimental setup, leads us to choose a type of control that can be robust to all these issues. At the same time, one should be aware of the inherent trade-off that exists between the robustness of the control law and the performance objectives [14]. Finally, one should also keep in mind, that, in the case of airplanes and space vehicles the natural frequencies of the controls generated by the pilot and the natural frequencies of the first sloshing modes of the fuel are very close [21]. This implies that great care should be taken when eliminating the unwanted sloshing modes.

The robust method we employ here is based on the $||\cdot||_\infty$ norm which indicates the

maximum gain value of the frequency response of an arbitrary transfer function F:

$$||F||_\infty = \sup_{\omega \in \mathbb{R}} \overline{\sigma}(F(j\omega)) \tag{3.16}$$

where $\overline{\sigma}$ denotes the maximum singular value. For a SISO system, this equation states that $||F||_\infty$ represents, on the Nyquist plot of $F(p)$, the distance from the origin to the farthest point on the plot. On the Bode plot, $||F||_\infty$ is the highest point on the magnitude frequency response.

As stated in Section 3.1 the first modes are the most important in terms of deformation energy of the structure (therefore having large amplitudes on the Bode plot - see the experimental Bode plot from Figure 4.2 in Section 4.2 of Chapter 4). We want to attenuate these resonant peaks of the transfer function between the perturbation and the controlled output.

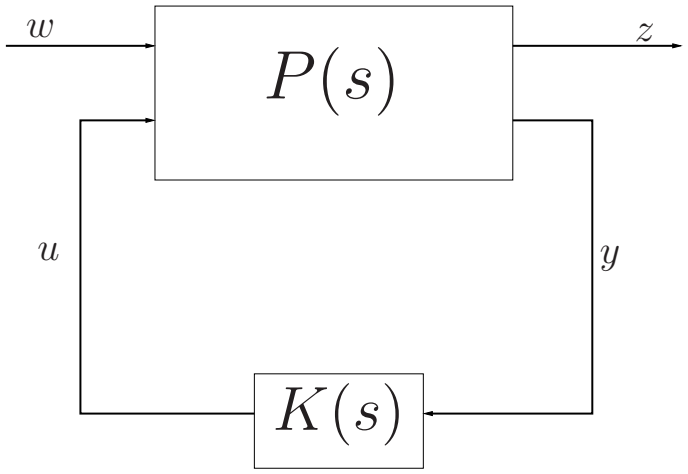

Figure 3.3: Standard H_∞ problem

Before starting the computations, we first write our problem in the standard form of the robust control, depicted in Figure 3.3. In this figure, w is the vector gathering all the perturbation signals, u is the control signal generated by the robust controller, y the output signal of the plant (the voltage delivered by the piezoelectric sensor) and z is a vector that contains all the to-be-controlled outputs. The choice of the variables contained by the z vector is very difficult. In our case, we propose a first choice for the to-be-controlled outputs by considering: the output signal of the plant y and the signal u generated by the H_∞ controller. The experimental state-space representation of the experimental setup (2.134) is denoted by $P(s)$, and the computed robust controller by $K(s)$.

If we take into account the four input and output signals: w, u, y and z, the plant P can be written by decomposition in four distinct matrices:

$$\begin{cases} z = P_{11}w + P_{12}u \\ y = P_{21}w + P_{22}u \end{cases} \tag{3.17}$$

or in a compact form

$$P(s) = \begin{bmatrix} P_{11}(s) & P_{12}(s) \\ P_{21}(s) & P_{22}(s) \end{bmatrix}.$$

Taking into account the feedback law $u = Ky$, equation (3.17) gives:

$$z = (P_{11} + P_{12}K(\mathbb{I} - P_{22})^{-1}P_{21})w,$$

where $(P_{11}+P_{12}K(\mathbb{I}-P_{22})^{-1}P_{21}) = F_l(P,K)$ is the lower linear fractional transformation (LFT). In addition we can also write the upper linear fractional transformation $F_u(P,K)$ which express the transfer between the control and the output of the plant:

$$y = F_u(P,K)u.$$

Using the LFT, the H_∞ control problem now becomes:

Finding the system $K(s)$ that will satisfy the optimization problem:

$$\min_{stabilizing\ K} ||F_l(P,K)||_\infty. \tag{3.18}$$

This optimization problem is further solved either using DGKF method and Ricatti equations (see [51]) or linear matrix inequalities (LMI) method and semi-definite programming (SDP) (see [31], [55]).

The state-space representation of the complete model, in the H_∞ framework (see Figure 3.3) can be summed up by:

$$\begin{cases} \dot{x}(t) &= Ax(t) + B_1w(t) + B_2u(t) \\ z(t) &= C_1x(t) + D_{12}u(t) \\ y(t) &= C_2x(t), \end{cases}$$

where matrices D_{11}, D_{21} and D_{22} (see the H_∞ framework of [145, Chapter 14]) are equal to zero. The control variable $u(t)$ is the voltage applied to one of the piezo-

electric actuator patch, the perturbation variable $w(t)$ is a perturbation applied to the other piezoelectric actuator, the output variable $y(t)$ is the voltage delivered by one of the piezoelectric sensors and $z(t) = \begin{pmatrix} u(t) \\ y(t) \end{pmatrix}$ is the to-be-controlled output. Furthermore, the variable $u(t)$ is selected as a controlled variable since we need to keep the voltage delivered by the controller in the limits imposed by the actuator saturation.

To take into consideration the value of the perturbation, we need to express it in a mathematical way so that it can be introduced in the robust controller synthesis. In our case, it is a random perturbation characterized by his frequency spectrum. Since the modes we consider are only of low frequency, it is natural to consider a perturbation whose frequency spectrum is also in low frequency. Furthermore, as it will be proved later in Section 4.2 of Chapter 4, we want to control all the system's modes until almost 30Hz. Therefore, we chose the low frequency spectrum $[0 \dots 50]$Hz for the perturbation, which is large enough in order to influence all the modes.

One can imagine many ways of modeling a frequency spectrum using filters. First, the order of the filter has to be selected. Second, depending on the frequency band we want to cover, we can choose different types of filters (low pass, high pass, band pass). In our case, since we want to cover the low frequencies band, the spectrum is modeled by a first order low pass filter. Indeed, since the perturbation has not a very complicated shape, we consider that a first order is sufficient to make a good approximation. Moreover, the cut off frequency of the filter is 50Hz. Under these considerations, the transfer function of the filter at the input of the perturbations, is:

$$H_1(s) = \frac{100\pi}{s + 100\pi}. \tag{3.19}$$

We also have to take into account the uncertainties related to the neglected modes. As stated earlier in the model presentation (see Section 2.2.3 for the plate and Section 2.3.4.1 for the tank with liquid, in Chapter 2), we neglected the higher order modes, thus the influence of their dynamic on the total dynamic of the system. The problem that may appear is an inherent and very important one in the control of infinite dimension systems: the spillover (the controller influence on the neglected high frequency modes). This issue is well analyzed in [15] or [16]. Moreover, it was proven that spillover is function of the actuator - sensor location and their effect on the neglected modes. The idea behind this is to see if the controller computed for some modes, does not destabilize the neglected ones. It is also well known that the

most likely mode to be destabilized is the first neglected mode [64].

Solutions to overcome the spillover are numerous. Let us mention a few of them: prefiltering the system output (prefiltering the piezoelectric sensor for us) [15], redesign of the structure and/or the controller [16] or placing the piezoelectric actuators and sensors where the spillover effect of the uncontrolled modes is small [66] (although this will diminish considerably the controllability and the observability of the system [15]).

The core idea of our reasoning, is to choose a low pass filter [125], which will introduce a roll-off specification in the controller synthesis, with a cut-off frequency fairly lower than the natural frequency of the first neglected mode [69]. This, on the other hand, will unavoidably worsen the control of the last considered mode [69]. As an example, one can check the work [88] concerning the implementation of the low pass roll-off filter on a flexible rectangular clamped-free-free-free paddle, similar to our plate.

Moreover, due to the closeness of the natural frequencies, the low pass filter has to have a sharp cut between the frequency of the last mode under consideration and the first neglected one. Thus, we choose more than 60dB/dec attenuation for the filter. There are different shapes of filters with different behavior in the low pass frequencies domain (see [133]). In our case we choose the roll-off filter with the transfer function:

$$H_2(s) = \left(\frac{1 + \frac{s}{\omega_1}}{1 + \frac{s}{\omega_2}} \right)^n \tag{3.20}$$

where ω_1 is the angular frequency of the cut-off while ω_2 is the angular frequency from which the high frequency attenuation gain is constant. Moreover, n is the order of the filter, that gives also the attenuation slope desired. Since we want at least 60dB/dec attenuation, the order is $n \geq 3$.

In order to use this filter in the robust analysis, we add it on the control signal u as it can be noticed on Figure 3.4. The H_1 filter modeling the perturbation is also added in the input of the system on the perturbation channel.

When considering the "to-be-controlled" output z, a more careful analysis needs to be carried out. First of all, as said earlier, we must monitor the amplitude of the control u since we do not want to reach the saturation levels of the piezoelectric actuators. Therefore, one component of the z vector will be necessarily the control u. Since we also want to attenuate the structure vibrations, we also need a variable that can quantify this.

In order to quantify the structure's vibrations we have two types of measures at

our disposal: the measures given by the piezoelectric sensors and the measures given by some mobile accelerometers. Both have the advantage of having a wide and regular band pass. The second measure is easier to use in the control problem since after two successive integrations we can find directly the position of the structure. This comes with a great drawback which is the noise level. Even though both measures are related to a charge amplifier (see Section 1.1 of Chapter 1), which is intended to reduce the noise level in the measurements, we notice that the measure given by the accelerometers is more noisy since they are more sensitive to the electric environmental field. This sensitivity coupled with the two integrations leads to very noisy measures at the end. This last issue lead us to use the data given by the piezoelectric sensors.

The whole robust synthesis, put under the shape of a standard H_∞ problem, is depicted in Figure 3.4.

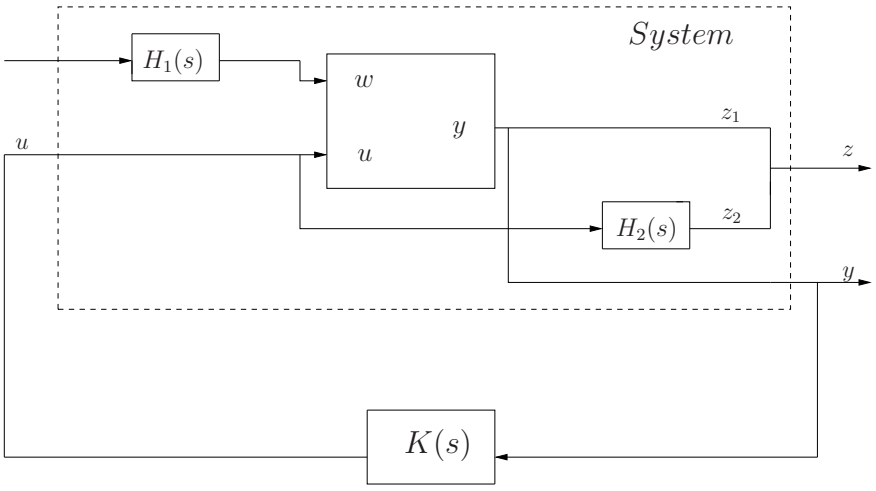

Figure 3.4: Standard H_∞ problem

3.4 Conclusion of the chapter

This chapter details the theory behind the tests of the next chapter. First, a theoretical basis for analyzing the experimental setup in terms of energy was given in the beginning of this chapter. Then, some theoretical details concerning the pole placement control and the robust H_∞ control are also presented.

Details about the computation of the most energetic modes of the system will be given in Section 4.2 while the controllers will be implemented and tested in Sec-

tions 4.4 and 4.5 of Chapter 4.

Chapter 4

Experimental results

In this final chapter the theory depicted earlier is implemented on the experimental device described in Chapter 1. This chapter will be constructed as follows: we first choose a suitable amount of modes for the finite dimensional approximation and second, for each mode, we make a very precise determination of its natural frequency and of the value of its damping. Using the theory described in Section 3.2 of Chapter 3, we propose a pole placement controller that will attenuate the plate vibrations. Then, using the framework of Section 3.3, we compute an H_∞ robust controller that, besides attenuating the plate vibrations, makes the system robust to some external perturbations. We will compare the results of both methods in Section 4.6 below.

4.1 Influence of the actuator dynamics

First of all we think that it is of great importance to test, wether or not the dynamics of the actuators has an influence on the dynamics of the model. As presented in Section 1.3.3 of Chapter 1, the response time of the piezoelectric patch is greater than the one of the voltage amplifier. Moreover, the speed limit of the voltage amplifier is greater than the normal frequency at which the system works (which is, as it will be proven later in Section 4.2, of a few Hertz). Based on these issues we infer that the actuator dynamics will not influence at all the dynamics of the system since it has a much larger bandwidth than the frequencies we consider.

Before proceeding to further tests, this issue is verified for numerical simulations. Therefore, we compute our model for a great amount of modes and for a fixed tank filling level of 0.9. We use 13 modes in this case, the first 3 for the liquid sloshing and the first 10 for the plate bending. These modes cover a natural frequency range between 0 Hz and 200 Hz and their amplitude and natural frequency are identical to

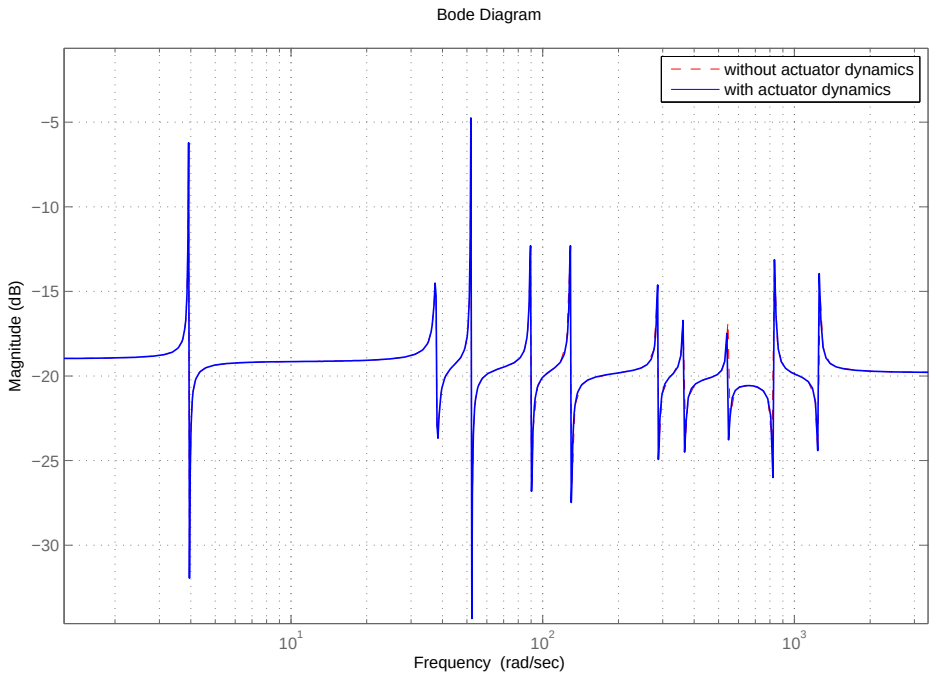

Figure 4.1: Bode plot of the system with and without considering the actuator dynamics, tank fill level of 0.9

the ones retrieved experimentally (see Figure 4.2 for an experimental Bode plot).

The Bode plots are given in Figure 4.1, for the case when the actuator dynamic is considered or not. As it can be seen, the two Bode plots are exactly the same which prove, as we expected, that the dynamic of the actuator does not influence the overall dynamic of the system for this frequency range.

Therefore, in the final system's model, the dynamic of the actuator will be modeled only by a unitary gain.

Remark: As it was proven in Section 2.2.3.1 of Chapter 2, the damping of the plate is computed from the quality factor Q_k using equation (2.42). Since the quality factor depends on the voltage applied to the structure, the damping of each mode will also depend on the voltage. Therefore, from now on, all the experimental tests are done using the same voltage of 2.5V amplitude at the input of the structure.

4.2 Choice of the suitable amount of modes

Before computing different controllers for our system and calculating the state-space representation of the experimental set-up (see Section 2.2.3 where the procedure is detailed), we need to determine the number of plate and sloshing modes we are going to consider for this finite dimensional approximation. The computed controller will then be simulated on a larger model. This is done in particular in order to test the existence or not of the spillover effect.

Several issues need to be kept in mind before fixing the number of modes.

One first issue concerns the frequency of the control signals generated by the pilot of the airplane. These commands are at low frequency (see [111], [129]), independently on the flight control of the airplane being fly-by-wire (the electronic control signals are transmitted by the pilot through wires to computers which determine how to move each actuator in order to have the desired response [4]) or fly-by-cable (the pilot himself has a physical connection to the flight control actuators which give the desired response to the airplane). Therefore, we should be aware of considering, in the model state-space approximation, especially low frequency modes since only these mode will interact with the control frequencies of the signals generated by the pilot (see [120] for an overview about the airplane modeling and flight requirements). The high frequency plate and sloshing modes, that are not in the range of control frequencies, can be easily dealt with (even removed) using a low-pass filter. Since they are not excited by the control frequencies, they are also prevented for getting to resonance.

Moreover, we would like to consider besides the inherent flexion modes, at least the first torsion mode of the plate, in order to see how the controller reacts to both types of plate movements.

In addition to all this, the main issue is that we must control the most energetic modes of the system. Using the energy approach detailed in Section 3.1 of Chapter 3, we compute the energetic contribution ratio of each mode to the total energy of the system. The choice of the modes will then be done by studying their energetic contribution.

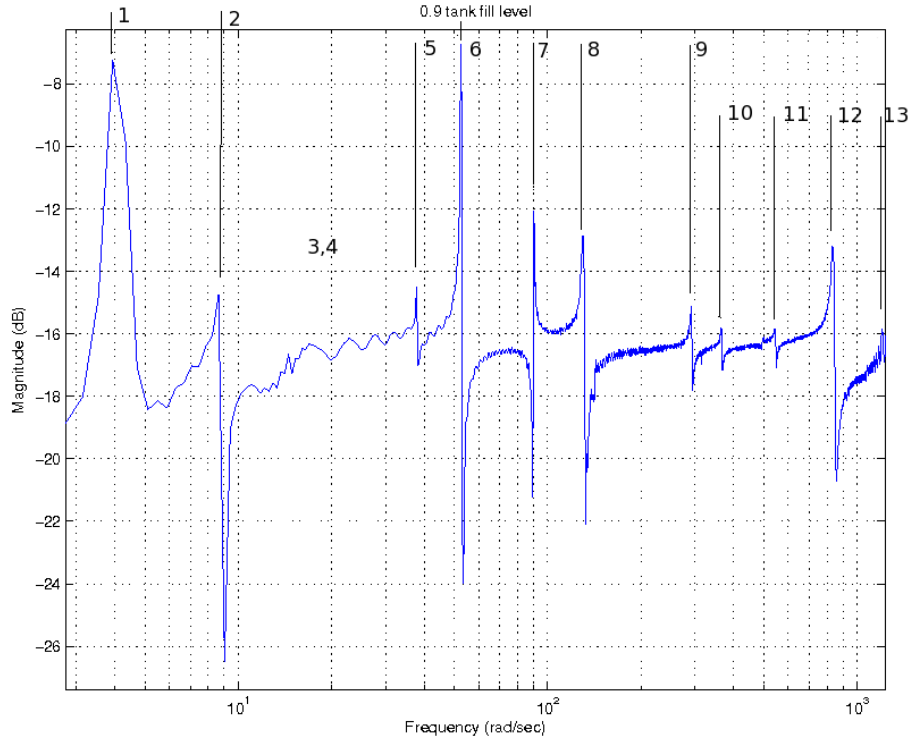

Figure 4.2: Experimental Bode plot for a tank fill level of 0.9 in the frequency range $[0, 200]$Hz. #1 is the first flexion mode of the plate, #2 is the first sloshing mode of the liquid, #3 and #4 are the second and third sloshing mode of the liquid (they are almost invisible due to their very small amplitude), #5 is the first torsion mode of the plate, #6 is the second flexion mode of the plate, #7 is the third flexion mode of the plate, #8 is the forth flexion mode of the plate, #9 is the fifth flexion mode of the plate, #10 is the sixth flexion mode of the plate, #11 is the second torsion mode of the plate, #12 is the seventh flexion mode of the plate, #13 is the eight flexion mode of the plate

We first start with a Bode plot of the experimental set-up in the case where the tank fill level is $\frac{h_s}{2R} = 0.9$ (see Section 2.3.2). The plot is depicted in Figure 4.2 for frequencies ranging from 0 Hz to 200 Hz. Based on this Bode plot we are able to compute the mode energy. The plot is obtained using a spectrum analyzer. Giving the input voltage and the range of frequencies, the spectrum analyzer generates a chirp signal, records the output of the device and generates the Bode plot. The advantage of employing the spectrum analyzer is the speed and simplicity of the method while the drawback is the finite number of points that the spectrum analyzer

can record. Therefore, a large frequency range implies a large distance between the recorded points. To overcome this issue, the Bode plot from Figure 4.2 was done as a superposition of several Bode plots. Using this approach, as the frequency range decreases and the maximum number of recorded points is constant, the distance between two consecutive recorded points decreases. Another advantage is that, since we have a small frequency range, each mode (especially the low frequency ones) passes the settling state and is thus recorded in the steady state.

Remark: Although we are aware that the experimental Bode plot may be used to find directly the state-space representation of the system, this is not our purpose here. If this would have been the case, we could have modeled the experimental device from the beginning using the finite element method. As explained in the introduction of Chapter 2, during the modeling phase we want to stay as close as possible to the physical meaning of the device and we do not want to see the plate and the cylinder just as a system with no physical interpretation. Using the system identification, or finite element method, we would obtain a system in which we can not differentiate the plate parameters from the liquid parameters. In this case it would be impossible, for example, to control only one parameter of the plate (like for example the first flexion mode) or only one parameter of the liquid (the first sloshing mode for example).

Mode	Characteristic	Natural freq.	Energetic contribution rate %	Total %
1^{st} mode	flexion	0.6238Hz	62.9542	62.9542
2^{nd} mode	sloshing	1.1556Hz	7.3177×10^{-7}	∼62.9542
3^{rd} mode	sloshing	2.1454Hz	0.0010	62.9552
4^{th} mode	sloshing	2.7929Hz	3.7632×10^{-4}	62.9556
5^{rd} mode	torsion	5.9977Hz	0.0220	62.9776
6^{rd} mode	flexion	8.2508Hz	9.1247	72.1023
7^{rd} mode	flexion	14.2495Hz	10.0202	82.1225
8^{rd} mode	flexion	21.0321Hz	13.5014	95.6239
9^{rd} mode	flexion	46.2245Hz	1.6166	
10^{rd} mode	flexion	58.0139Hz	2.3702	
11^{rd} mode	torsion	86.7584Hz	0.3873	
12^{rd} mode	flexion	132.6601Hz	0.0012	
13^{rd} mode	flexion	199.9073Hz	0.0752	

Table 4.1: Modal energetic contribution rate of each mode

As seen in Section 2.3.2, in order to apply the energy approach method, it is compulsory for the structure model to be in the diagonal form. Since initially the model is not diagonal due to tank/plate couplings, we use a system transformation which will put the model into a diagonal form. The natural frequency of the modes along with the results of the method are given in Table 4.1.

As it can be seen from Table 4.1, the first 8 modes of the system, with frequencies up to 21 Hz, contain 95% of the total energy of the system. One should notice that in this case all the constraints detailed earlier are respected: the considered modes are the most energetic ones, at least one torsion mode of the plate is present and the mode frequency is low enough so that it can interfere with the natural frequency of the airplane controls.

Therefore, from now on, for all the controller computations, we consider $M = 3$ modes for the liquid sloshing and $N = 5$ modes for the plate bending. The modal energetic contribution is computed for a fixed tank fill level. Concerning other tank fill levels, the energetic contribution of the modes is similar, the only difference being that, as the fill level decreases, the influence of the first flexion mode of the plate decreases. In spite of this issue, we consider that the first 8 modes still represent the main part of the energy of the total plate.

4.3 Model adjustments

Before performing the tests on the experimental set-up, some model computations need to be made. As presented, in Section 2.4 of Chapter 2, we write the complete model of the system: the rectangular plate coupled with the tank filled with liquid up to an arbitrary depth. This model, which is computed in the infinite dimension, is approximated by the state-space representation (2.134). We are recalling here this representation:

$$\begin{cases} \dot{X} = \begin{pmatrix} A_p & A_{\theta p} \\ A_{p\theta} & A_\theta \end{pmatrix} X + \begin{pmatrix} B_p \\ B_{p\theta} \end{pmatrix} u \\ y = \begin{pmatrix} C_p & \mathbf{0} \end{pmatrix} X, \end{cases} \tag{4.1}$$

where the state-space vector $X = \begin{pmatrix} X_p \\ X_\theta \end{pmatrix}$ is a combination of the state-space vector of the plate X_p and of the tank with liquid X_θ.

In order to have an accurate model of the device, some analytical calculus correlated with measurements on the experimental setup need to be done. This takes three steps: the first two steps can be seen as a preparation in order to implement the set of equations (4.1), while the third one consists of a matching between the analytical model and the experimental set-up. They are detailed below:

- Step 1: As it can be seen from equation (2.134), the normal frequencies of the plate and of the liquid sloshing have to be calculated. First they are computed analytically, using equation (2.36) for the plate and using the experimental curves depicted in Figure 2.9 for the liquid sloshing, and then are compared with the values measured on the device. The method is detailed below in Section 4.3.1;
- Step 2: After the frequency computation, the inherent damping corresponding of each mode also needs to be found. This is done by direct measures on the device. More details are given below in Section 4.3.2;
- Step 3: Once the model is computed, we make a comparison for different filling levels between the analytical model and the experimental setup. Since we notice a discrepancy between the analytical model and the data collected by experiments, a trial and error method is employed in order to diminish this discrepancy. The method is implemented and the results are shown in Section 4.3.3.

4.3.1 Computation of the natural frequency

It is important to establish the natural frequencies of each mode with great accuracy in order to have a model as close as possible to the experimental device.

4.3.1.1 Computation of plate natural frequencies

As detailed in Section 2.2.1 of Chapter 2, the plate model is based on the model of two orthogonal beams (see equation (2.32) for the approximation of plate deformation). The modal deformations of the beam give the modal deformation of each mode of the plate by a simple multiplication operation.

Beam natural frequency computation

We first compute the natural frequencies of the two beams since they are needed in order to compute the modal displacements. They cannot be measured experimentally,

thus they are only analytically computed for the case of a clamped-free beam and of a free-free beam. In the case of the clamped-free beam, the natural frequency of the i^{th} mode ω_i^L (in Hz) is computed by replacing equation (2.11) into (2.15). For the free-free beam, the natural frequency of the j^{th} mode, denoted respectively ω_j^l, is again found by solving equation (2.22) coupled with (2.23). The value of the frequencies for both beams is detailed below:

Clamped-free beam			
Mode 1	Mode 2	Mode 3	Mode4
2.3244Hz	14.5679Hz	40.7920Hz	79.8557Hz
Free-free beam			
Mode 1	Mode 2	Mode 3	Mode 4
0Hz	0Hz	1.0687kHz	2.9461kHz

Table 4.2: Natural frequencies of the beams associated to the plate

For each beam, the first modal displacements (mode shapes) are drawn below in Figures 4.3 and 4.4. The lengths of the beam are taken from Table 1.1, Chapter 1, and represent the length $L = 1.36m$ and the width $l = 0.16m$ of the plate.

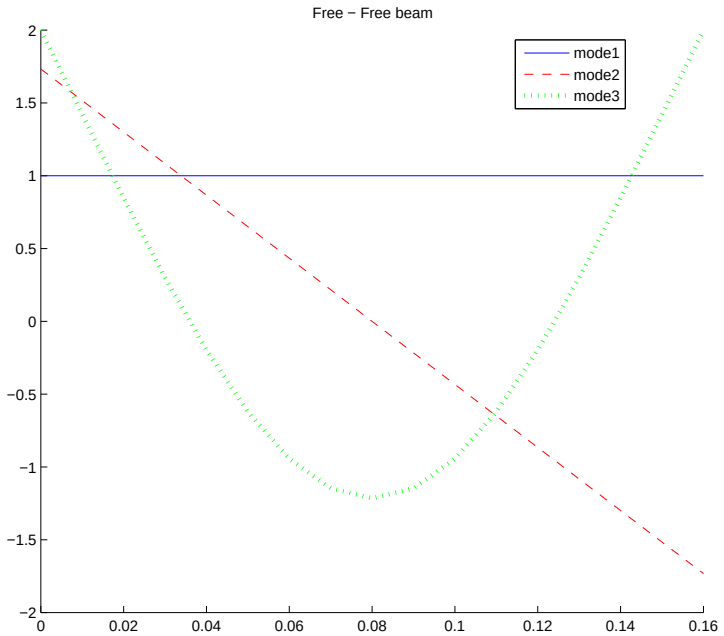

Figure 4.3: First three modal displacements of the free-free beam

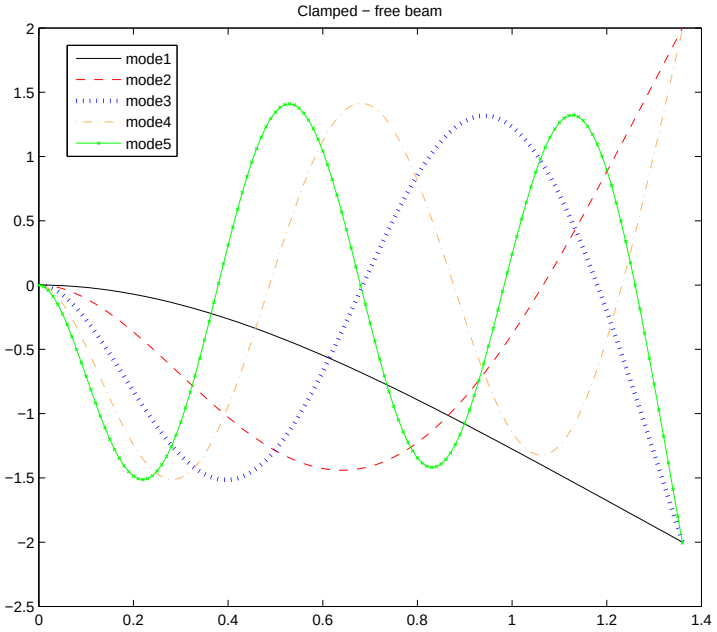

Figure 4.4: First five modal displacements of the clamped-free beam

In the case of the free-free beam we can notice (see Figure 4.3) the presence of the two rigid modes with natural frequency of 0 Hz, as predicted in Section 2.2.1 of Chapter 2. The deformation of the first two modes implies that we can move the position of the beam without deforming the beam at all. We remind to the reader that the calculus of all the modal displacements was detailed in Section 2.2.1 and is given for the clamped-free beam by equation (2.13) and for the free-free beam by equation (2.20), coupled with (2.24) and (2.25) for the two rigid modes.

We now compute the natural frequency and mode shape for each mode of the plate based on the beam theory. We detail below several methods that we used to determine each frequency. These methods rely either on calculus (analytical or numerical) or on experimental measurements.

Plate natural frequencies calculation - analytical method

The analytical calculus of the plate natural frequencies is done using the methodology presented in Section 2.2.3.1 of Chapter 2. Therefore, the plate frequencies are directly found by implementing the equation (2.36). Using the characteristics of the plate depicted in Chapter 1 (which are presented in Table 1.1), the natural frequencies can be computed. After the calculus, the frequency of the modes and their modal characteristics (type of mode) are given in Table 4.3.

Mode	Natural frequency	Type
1^{st} mode	2.301Hz	1^{st} flexion
2^{nd} mode	14.413Hz	2^{nd} flexion
3^{rd} mode	40.3583Hz	3^{rd} flexion
4^{th} mode	49.2027Hz	1^{st} torsion

Table 4.3: Natural frequencies of plate modes - analytical calculus

Here below, the modal displacements of the plate, are presented for the case when a flexion movement and a torsion movement are observed. The order in which the modes appear is according to the plate natural frequency computed earlier and detailed in Table 4.3. We recall that the modal displacements of the plate are obtained just by multiplying the modal displacements of the perpendicular beams, as demonstrated in Section 2.2.3 and given by (2.32).

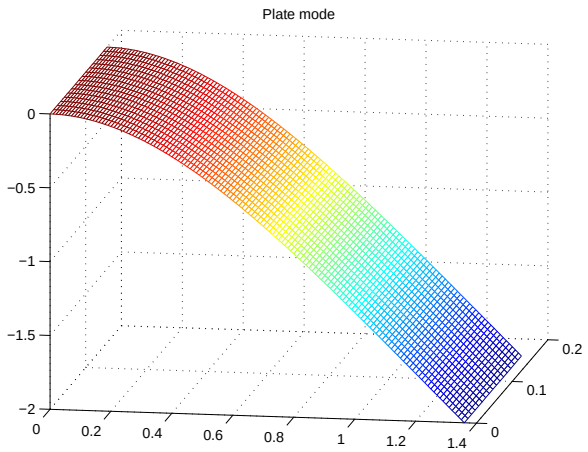

Figure 4.5: Plate first flexion mode at 2.301 Hz, $\eta_1(y,z) = Y_1(y)Z_1(z)$

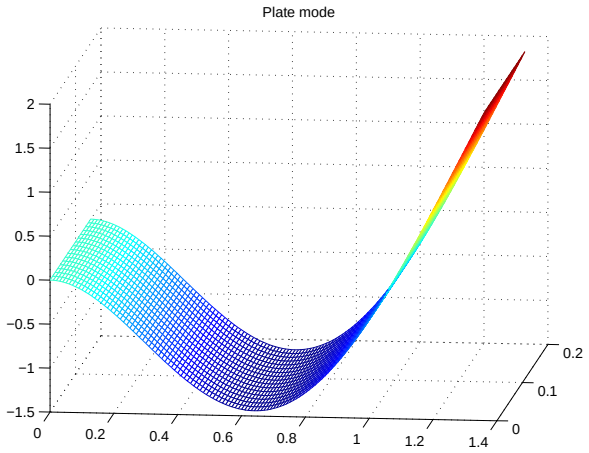

Figure 4.6: Plate second flexion mode at 14.413 Hz, $\eta_2(y,z) = Y_2(y)Z_1(z)$

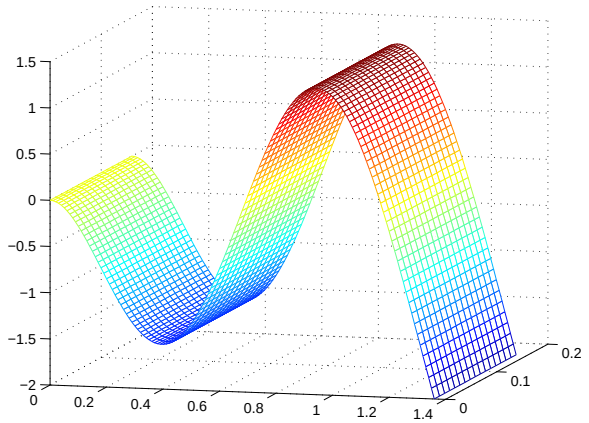

Figure 4.7: Plate third flexion mode at 40.3583 Hz, $\eta_3(y,z) = Y_3(y)Z_1(z)$

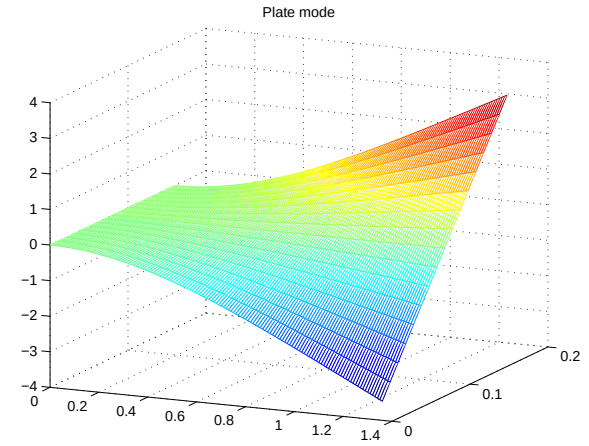

Figure 4.8: Plate first torsion mode at 49.2027 Hz, $\eta_4(y,z) = Y_1(y)Z_2(z)$

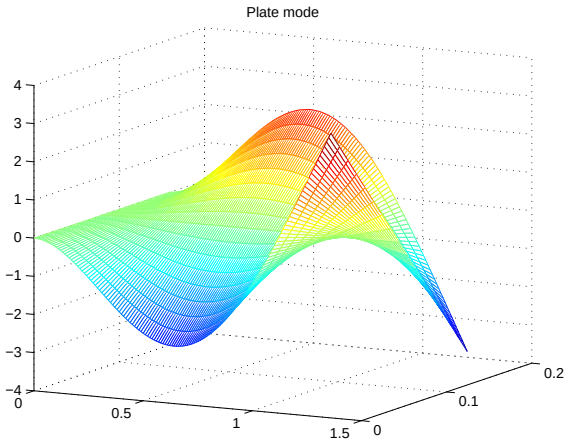

Figure 4.9: Plate second torsion mode, $\eta_8(y,z) = Y_3(y)Z_2(z)$ (not taken into account during the modeling phase)

Since there is an infinity of modal displacements of the beam, we suggest a numerical method in order to check if the ones we choose for expressing the modal displacements of the plate are correct or not. Since, as we stated in Section 2.2.3 of Chapter 2, the Ritz basis of the plate is orthogonal, we suggest to effectively check this orthogonality between the modal displacements of the two beams. Therefore, for each plate mode, we compute the scalar product of the corresponding beam deformation [42]. In our case, the scalar product is not exactly 0 but ranges from 10^{-4} to 10^{-17} depending on the modes. Based on these results, we conclude that the modal displacements of the two beams are well chosen and thus the modal displacements of the plate are well constructed.

One important thing to notice is that all the computations done in the analytical case impose the plate to be homogeneous. Thus, we cannot take into consideration some structure discrepancies like the hole in the plate created for the tank attachment or the mass non homogeneity caused by the presence of actuators and sensors.

Plate natural frequency calculation - numerical method

In order to verify the analytical calculus of the plate natural frequencies (Table 4.3), we propose a check-up method using the numerical finite elements analysis and ANSYS© program. After starting the numerical routine, one can see a close approximation between the natural frequencies found by the analytical calculus in Table 4.3 and those found by the numerical calculus in Table 4.4, especially for the flexion modes.

Mode	With piezo. actuators	Without piezo. actuators	Type
1^{st} mode	2.3992 Hz	2.4983 Hz	1^{st} flexion
2^{nd} mode	14.678 Hz	15.104 Hz	2^{nd} flexion
3^{rd} mode	37.326 Hz	38.073 Hz	1^{st} torsion
4^{th} mode	40.242 Hz	41.056 Hz	3^{rd} flexion

Table 4.4: Natural frequency of plate modes when the tank hole is taken into account - numerical calculus

Moreover, this numerical method allows us to consider issues that were neglected earlier and that make the plate non homogeneous: the piezoelectric actuator patches or the circular cavity where the cylindrical tank is attached.

Afterward, we plan to conduct some numerical simulations in order to measure the influence of the neglected phenomena (actuators and tank presence) on the plate natural frequencies. The results clearly demonstrate the prediction on the plate natural frequencies: the simple introduction of the piezoelectric actuators (translated into a small change of plate mass and a change in plate mass center) shifts the natural frequencies and changes the damping of the plate. This difference can not be proved on the experimental device, since the actuators and sensors are glued on the plate, neither can be taken into account by the analytic calculus. In reverse, it can be studied using the numeric method of calculus.

The mode shapes of the first four modes, computed using ANSYS©, are depicted in Figure 4.10.

Moreover, we proved in [115] that the presence of the empty cylindrical tank diminishes even more the natural frequencies of the modes and increases the action of the torsion modes.

Plate natural frequency - experimental measurements

Finally, after the computation of the natural frequencies using the analytical method and after shortly comparing with the results from the numerical method, we measure the values directly on the experimental setup. As explained in Chapter 1, we can measure the natural frequencies of the plate only in the case when the piezoelectric actuators/sensors and the hole for the cylinder attachment are present (see Figure 1.9 and Figure 1.10 for an actuator/sensor view and Figure 1.4 for a plate view without the cylindrical tank). Consequently, the measured frequencies will be closer to the ones from Table 4.4, for the case when the actuators are considered, than to the

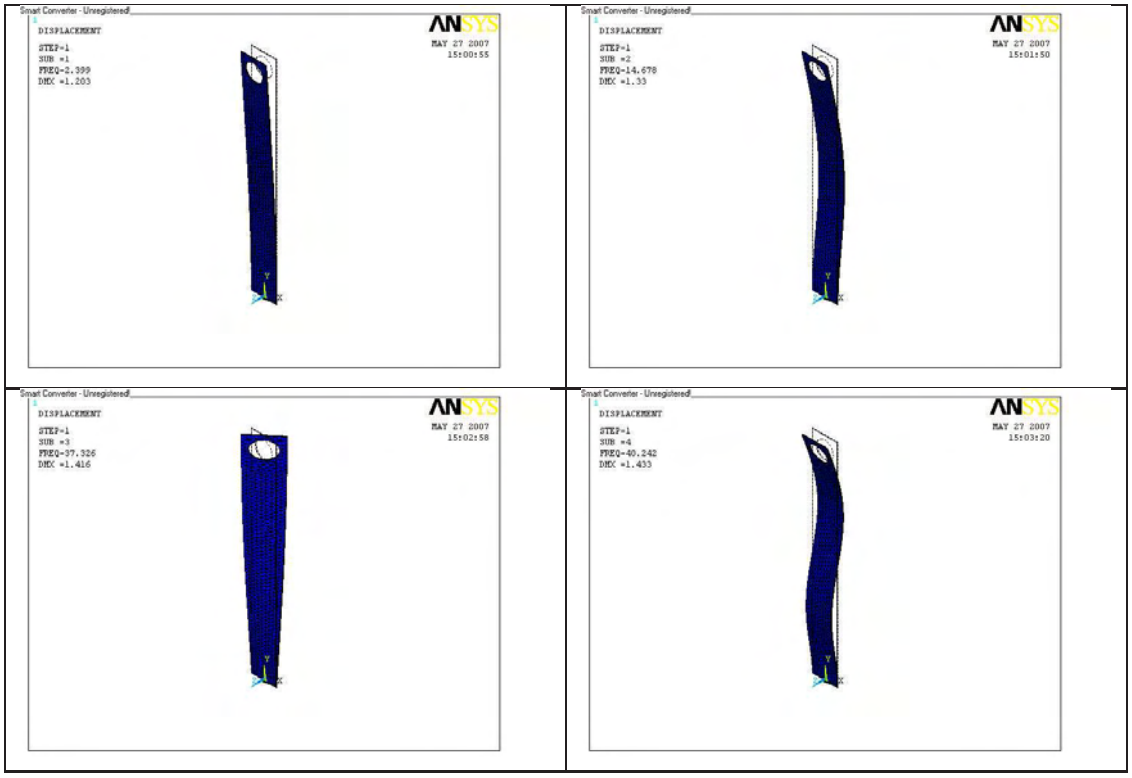

Figure 4.10: First 4 modal displacements of the plate

ones from Table 4.3, computed with the analytical method (since, in the analytical method, the plate is considered homogeneous).

Let us describe the procedure we followed to make the experimental measurements. We first restrict ourselves on the frequency band of $[0, 50]$Hz since it is the range where the first modes are concentrated. Then, using a spectrum analyzer, we identify the natural frequencies of the modes. We first obtain a rough Bode plot with an estimation of the natural frequencies and then, based on this, we search in the neighborhood of the estimated frequencies to obtain the real natural frequency of each mode. Since finding the natural frequency of a mode is equivalent with finding the frequency for which the mode is at resonance, we check on an oscilloscope the amplitude of the output signal and when this amplitude is maximum then the exact value of the natural frequency is reached.

In order to know the natural frequencies of the plate, we use a Bode plot of the system given by a spectrum analyzer device. It generates an input signal using the specifications we impose: a sinusoidal chirp signal of constant amplitude of $5V$ and with a frequency varying between 0 Hz and 50 Hz. Concerning the output signal, we have two types of sensors that can give us some information about the plate deformation: piezoelectric sensors and accelerometers. We know that in theory, the

Mode	Natural freq. 1 actuator	Natural freq. 2 actuators
1^{st} mode	2.37Hz	2.375Hz
2^{nd} mode	14.41Hz	14.438Hz
3^{rd} mode	39.18Hz	39.25Hz
4^{th} mode	43.40Hz	43.875Hz

Table 4.5: Comparison between the natural frequencies in the case where one or two actuators are used

measures given by the piezoelectric sensors are more accurate than the ones given by the accelerometers which are more influenced by the environmental inherent noise.

This last issue is well presented in [115], thus, it will not be detailed here. We only repeat the conclusion: the frequencies given by the piezoelectric sensor are closer to the real natural frequencies and the Bode plot. Moreover the Bode plot obtained with accelerometer sensors, is more noisy. Therefore, from now on we consider for our measurements only the piezoelectric sensors, the accelerometers being only used for deciding about the mode type (flexion or torsion) as detailed in [115] or below.

We remind that our purpose is to attenuate the system vibrations but also to make the system robust to external perturbations. One way for applying perturbations is to send a voltage to one of the piezoelectric actuators. Since applying the same voltage to both actuators does not seem to change the frequency of the modes nor to accentuate their influence (see Table 4.5 for a comparison of the frequencies and [115] for more details regarding this issue), we intend to use one of the actuators as an external exterior perturbations entry to the system.

Consequently, from now on, we consider the plate natural frequencies from Table 4.5, for the case where only one actuator is used.

Experimental determination of mode type

The natural frequency of the first modes can be measured or computed using the theory described above. Besides this, the determination of the mode type is of great importance in order to be sure that at least one torsion mode of the plate is considered. This issue was also well detailed in our previous work [115], thus, only brief results are presented below.

The mode characteristic can be found using an easy method based on two accelerometer sensors. The two accelerometers are placed on the free end of the plate on vertical extremities. The analog signal delivered by the sensors is viewed on an oscilloscope when the plate vibrates. If the two signals are on phase then the vibration

has a flexion movement. At In the same time, if the two signals have a phase difference of π (phase opposition) then we have a torsion movement of the plate. Using this intuitive method we are able to determine the characteristic of each mode.

After analyzing the accelerometer signals, the results are briefly presented here. One can found more details in [115].

- The 1^{st} mode with a frequency around 2.37 Hz is a flexion mode. The shape of the mode is the same as in Figure 4.5;
- The 2^{nd} mode with a frequency around 14.4 Hz is also a flexion mode and his shape is the one from Figure 4.6;
- The 3^{rd} mode has a predicted numerical frequency around $37 - 38$ Hz (see Table 4.4) or around 49 Hz (see Table 4.3). Moreover, the mode shape is the one from Figure 4.8. We say on purpose, a "predicted" natural frequency since it is invisible on the experimental set-up. A possible explanation of this might be the closeness between his natural frequency and the natural frequency of the flexion mode right next to him. Another reason might also be the plate configuration which makes difficult the excitation of the torsion movement by just one piezoelectric actuator;
- The 4^{th} mode with a natural frequency around 43.4 Hz is also a flexion mode and his shape is the one from Figure 4.7.

As a conclusion, we can summarize in the following Table 4.6 the results concerning the natural frequencies of the plate:

Mode	Measured freq.	Analytical freq.	ANSYS freq.	Mode type
1^{st} mode	2.37Hz	2.301Hz	2.399Hz	flexion
2^{nd} mode	14.41Hz	14.413Hz	14.678Hz	flexion
3^{rd} mode	39.18Hz	49.202Hz	37.326Hz	torsion/invisible
4^{th} mode	43.40Hz	40.358Hz	40.242Hz	flexion

Table 4.6: Natural frequency and the mode description for the first 4 plate modes

4.3.1.2 Computation of the natural frequencies of sloshing modes

Concerning the natural frequencies of the sloshing waves, they are computed using the methodology detailed in Section 2.3.1 of Chapter 2 and given by Figure 2.9.

Since, as explained in Section 2.3.2, there are no theoretical results for the longitudinal liquid sloshing of the cylindrical horizontal tank, we made a tank approximation by keeping unchanged the natural frequencies of the sloshing modes. After the "virtual" rectangular tank is calculated, the natural sloshing frequencies can easily be computed using equation (2.88) from Section 2.3.3.

In order to approximate the cylindrical tank we proposed three different methods, each method being well detailed before in Section 2.3.2. In Table 4.7, we give the comparison between the sloshing frequencies delivered by each approximation method and the natural sloshing frequencies computed from the experimental curves (see Figure 2.9).

Mode	1^{st} method	2^{nd} method	3^{rd} method	Empirical curves [48]
1^{st} mode	0.7848 Hz	3.6175 Hz	0.7891 Hz	0.7869 Hz
2^{nd} mode	2.0304 Hz	12.7347 Hz	1.9982 Hz	2.1177 Hz
3^{rd} mode	2.7647 Hz	24.1601 Hz	2.7521 Hz	2.7907 Hz

Table 4.7: Comparison of the sloshing frequencies obtained from the experimental curves and with different approximation methods. Tank fill level $\frac{h_s}{2R} = 0.7$. For other tank fill levels, the results respect the same pattern.

The method we suggest for tank approximation is the third method tested above since it gives sloshing frequencies close to the experimental ones. Moreover, even though the sloshing frequencies obtained using the first method are closer to the experimental ones, the implementation of this method is very tedious as explained in Section 2.3.2.

The exact measurement of the sloshing frequencies on the experimental set-up was not done since we did not find a suitable device to do this. This is due to the impossibility of studying the sloshing of the liquid in the tank alone, without any connection to the plate. Even though this measurement was done in the literature, (see [105] where sensors were constructed for this specific issue or [50, Chapter 42] where the laser Doppler anemometry method is described for measuring fluid parameters), our purpose here was not to measure explicitly these values but to control the motion of the plate and the sloshing. Moreover, we will consider that the controller we compute will be robust enough to take this issue into account.

Despite the impossibility to exactly measure the value of the frequency, using a recording video camera, we still managed to see the shape of the liquid sloshing. We

observed that for the first three antisymmetric modes, the mode shape is exactly as the one from Figure 2.14.

4.3.1.3 Natural frequencies of the complete system: plate and tank

Until here we computed the plate natural frequencies and the liquid natural sloshing frequencies separately. The liquid sloshing frequencies were computed in order to validate the geometric approximation approach we are using, thus the validity of the considered rectangular tank. Concerning the plate natural frequencies, they were first computed in order to demonstrate their variation when the plate configuration changes and second in order to have a rough approximation of their values. The next logical step now is the study of the natural frequencies when the plate and the tank with liquid are coupled. The last issue is of critical importance if we want a model close to the reality depicted in Figure 4.2.

Our purpose in this study is to control the system vibrations for different tank filling levels. Therefore, we consider two different tank filling levels: in the first case, the tank filling is equal to 0.7, that is to say $\frac{h_s}{2R} = 0.7$ and in the second case it is equal to 0.9, (see Section 2.3.2 for further details). Moreover, as from [114], for this experimental device, the cases for which the tank fill level tends to 1 are the most difficult to control.

Using a spectrum analyzer we first obtain a Bode plot for each level. The two plots are depicted in Figure 4.11 and in Figure 4.12 (Figure 4.12 being the same as Figure 4.2 for the $[0 \cdots 50]$Hz band).

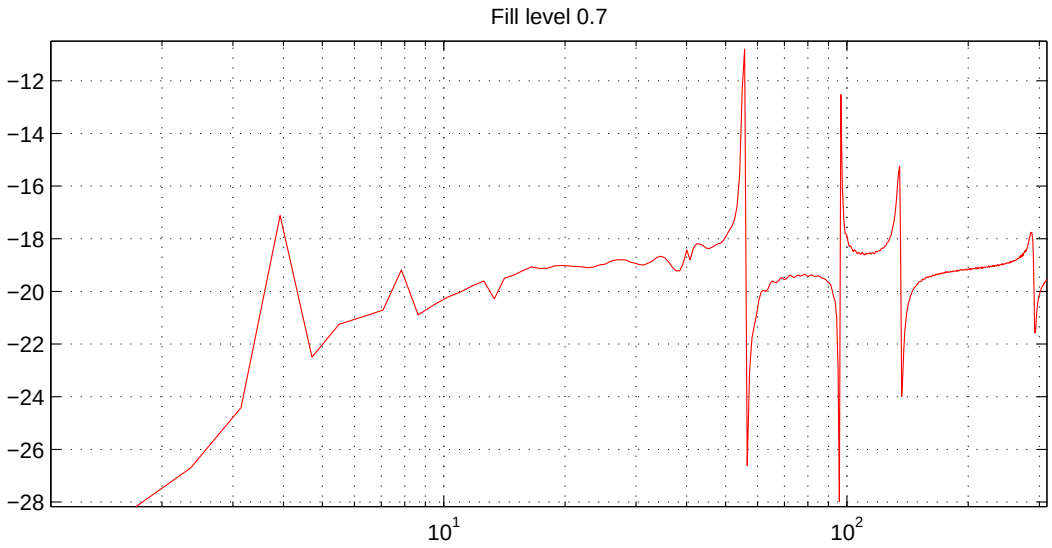

Figure 4.11: Experimental Bode plot for the plate and a tank fill level of 0.7

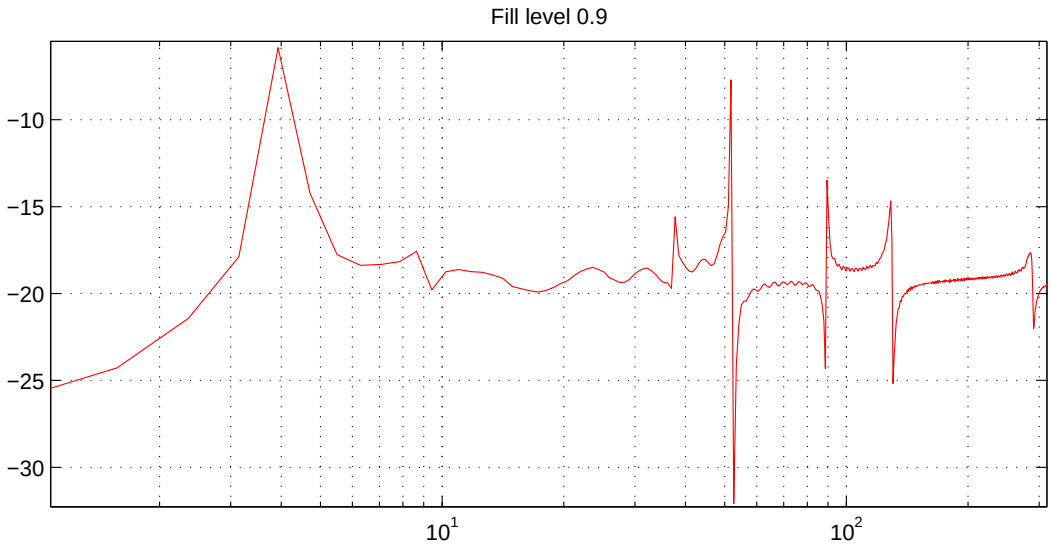

Figure 4.12: Experimental Bode plot the plate and a tank fill level of 0.9

Then, using a frequency generator, we search around each peak value of the Bode plot in order to find the exact natural frequencies of each mode. The calculus is very tedious since we want to find the most precise values. The results are given below in Table 4.8 for the plate and liquid sloshing:

Mode	Description	Tank fill level of 0.7	Tank fill level of 0.9	Plate alone
1^{st} mode	1^{st} flexion	0.6249Hz	0.6237Hz	2.37Hz
2^{nd} mode	2^{nd} flexion	8.8777Hz	8.2509Hz	14.41Hz
3^{rd} mode	1^{st} torsion	6.3753Hz	5.9979Hz	39.18Hz
4^{th} mode	3^{rd} flexion	15.3755Hz	14.2498Hz	43.40Hz
5^{th} mode	4^{th} flexion	21.4996Hz	21.0321Hz	55Hz
6^{th} mode	1^{st} sloshing	1.2655Hz	1.4149Hz	-
7^{th} mode	2^{nd} sloshing	1.9977Hz	2.1480Hz	-
8^{th} mode	3^{rd} sloshing	2.7510Hz	2.7940Hz	-

Table 4.8: The measured natural frequencies for the complete system (plate and liquid) when the tank is filled up to some arbitrary depths

When comparing Table 4.8 for a tank fill of 0.7, with the previous Table 4.7, where the sloshing frequencies are computed for the free tank without any external interaction, one can notice a slight shift of the frequencies. This is not because of some errors in the computation process. On the contrary, this proves, as we expected,

that the sloshing frequencies of the liquid also change when the coupling between the tank and the plate is considered.

Moreover, since we are doing a mass-pendulum approximation, we also need to determine, for the coupled system, the parameters of the mass-pendulum systems as detailed in Section 2.3.4.2. These parameters are presented here for the two different tank filling levels:

Mode \ Pendulum	Length	Mass	Hinge location	Measured freq.
1^{st} sloshing	0.1550m	2.4780kg	0.3659m	1.2655Hz
2^{nd} sloshing	0.0622m	0.1961kg	0.0363m	1.9977Hz
3^{rd} sloshing	0.0328m	0.0482kg	0.0165m	2.7510Hz

Table 4.9: Characteristics of the mass-pendulum systems for tank fill level 0.7

Mode \ Pendulum	Length	Mass	Hinge location	Measured freq.
1^{st} sloshing	0.1240m	2.7404kg	0.1777m	1.4149Hz
2^{nd} sloshing	0.0538m	0.1483kg	0.0296m	2.1480Hz
3^{rd} sloshing	0.0318m	0.0325kg	0.0354m	2.7940Hz

Table 4.10: Characteristics of the mass-pendulum systems for tank fill level 0.9

Two important things need to be noticed from Table 4.8. The first one is that, now, the torsion mode is visible on the experimental set-up, that is to say we found a configuration that will finally excite the torsion mode. Moreover, comparing the frequency values of the modes, the position of the torsion mode has changed. It is now right after the first flexion mode of the plate, that is to say the third peak of Figures 4.11 and 4.12. The second thing is that, due to the addition of liquid in the tank (the weight difference between the two tank fillings is 0.8671kg), the total mass of the plate increases and the natural frequency of each plate mode shift a lot towards zero. This shift is more prominent when more liquid is added in the tank, that is to say for a fill level of 0.9. [1]

[1]The mass of the plate alone, without the tank, is 3.2313kg while the mass of the liquid, alone, when the tank fill level is 0.7 equals 3.2371kg and the mass of the liquid when the tank fill level is 0.9 equals 4.1042kg.

4.3.2 Computation of modal damping

The modal damping is, along with the natural frequency, another important parameter that need to be well calculated. Concerning the computing of the plate modal damping, we used the approach detailed in Section 2.2.3.1 of Chapter 2.

As explained there, the damping of each mode Q_k is expressed using equation (2.38) detailed here:

$$Q_k = \frac{\omega_k}{\omega_{k2} - \omega_{k1}},$$

where ω_k is the natural angular frequency of the mode. The angular frequencies ω_{k1} and ω_{k2} are computed in order to have the amplitude of the mode attenuated by 3dB.

The plate natural frequencies are the ones from Table 4.8. After checking on an oscilloscope the amplitude of the resonance signal, we divide this amplitude by $\sqrt{2}$ (equal to 3dB attenuation) in order to find the two frequencies ω_{k1} and ω_{k2}. Using the above equation we obtain the damping for the first five modes of the plate. The results are given in Table 4.11.

Mode	Natural freq. 0.7	Damping 0.7		Natural freq. 0.9	Damping 0.9
1^{st} mode	0.6249Hz	0.0019		0.6237Hz	0.0020
2^{nd} mode	6.3753Hz	0.0015		5.9979Hz	0.0015
3^{rd} mode	8.8777Hz	0.0083		8.2509Hz	0.0083
4^{th} mode	15.3755Hz	0.0039		14.2498Hz	0.0039
5^{th} mode	21.4996Hz	0.0030		20.4675Hz	0.0030

Table 4.11: Measurement of the damping of each vibration mode

The measure of the liquid damping is difficult since it has to be done by the bias of the plate. The measuring procedure is, in theory, the same as in the case of the plate. Since, at resonance, the amplitude of the sloshing is very difficult to analyze on the oscilloscope, we choose the damping of the sloshing modes to be constant, equal to 0.001 which is the viscous coefficient of the water at normal temperature of $\sim 20°C$ [76].

4.3.3 Model matching problem

The complete system model, described by the equation set (2.134), was first validated in [116] by a comparison of a time-response for a given initial deformation of the plate. However, in order to obtain a model which provides a good match of

the measured frequency response, some adjustments are required by considering the Bode plots. These adjustments are done following a trial-and-error method (first the frequencies are matched and then is the damping). Other methods are possible for flexible structures (see for example [119] and references therein).

This model matching is necessary since some mechanical elements are not well known and have not been taken into account in the analytical modeling of the structure. These elements include the circular ring used to attach the tank on the plate (see Figure 1.1), the non-homogeneity of the plate and the weight of the tank.

As a first step of the model matching, the frequencies of the plate are adjusted. A second step of the model matching is the adding of a static gain that corresponds to the high frequency modes neglected during the model reduction static correction [121]. This allows to get a more realistic model at low frequencies. The comparison of the Bode plots for $e = 0.7$ and $e = 0.9$ on Figures 4.13 and 4.14 shows that the model, for $e = 0.7$ is quite accurate with respect to the real data while there is some discrepancy in the amplitude of the first sloshing mode for $e = 0.9$.

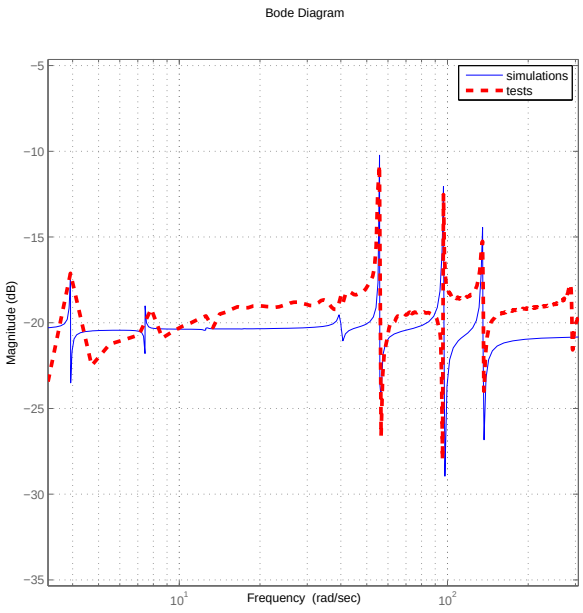

Figure 4.13: Frequency matching for the tank filling level $e = 0.7$ (numerical model - plain line and experimental set-up - dotted line)

In the two figures, the first peak corresponds to the first flexion mode of the plate (0.625 Hz) and the second peak to the first sloshing mode (1.2655 Hz for $e = 0.7$ and 1.4149 Hz for $e = 0.9$) in the tank. The next four peaks are respectively representing: the first torsional mode (the third peak) (6.38 Hz) and the second (8.75 Hz), third

(14.45 Hz) and forth (21.50 Hz) flexion modes of the plate. The second and third modes of the liquid sloshing cannot be identified on the Bode plots due to their very small amplitude.

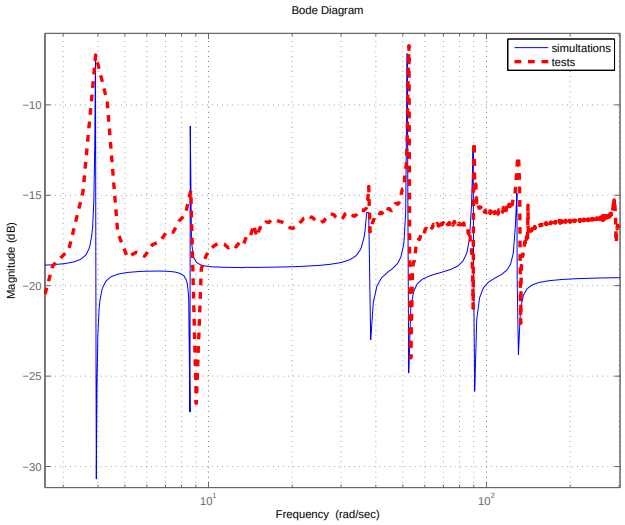

Figure 4.14: Frequency matching for the tank filling level $e = 0.9$ (numerical model - plain line and experimental set-up -dotted line)

Conclusion: In this section, we established an initial model of the structure based on computation and measurements of all natural frequencies and damping. Then we did a model matching in order to tackle the mismatch due to some neglected physical phenomena. In the following, we are considering the controller synthesis on these new matched models.

4.4 Pole placement controller

This section aims at computing a controller attenuating the plate vibrations. We are using here a state feedback strategy coupled with a Luenberger full state observer, since all the state-space vector of the system is unknown. Furthermore, based on the theory detailed in Section 3.2 of Chapter 3, we use a pole placement method in order to specify the closed-loop poles and the observer poles. Furthermore, the control scheme we are following is the one depicted in Figure 4.15, where the matrices to be determined are K and G.

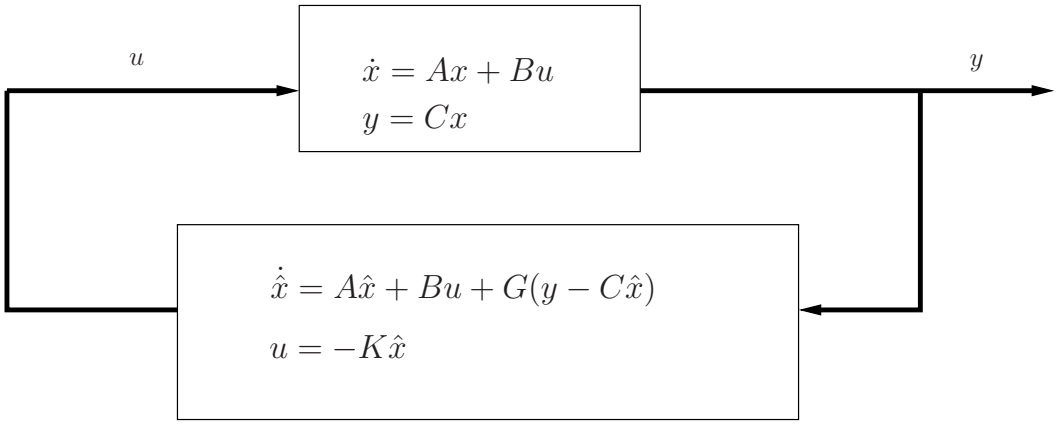

Figure 4.15: Feedback control law and observer

First, we compute the observability and controllability test matrices in order to be sure that all the system states are controllable and observable. Once this is set, we impose the dynamic of the state feedback law and of the observer. The poles which will specify the dynamic of the closed-loop system are chosen by selecting the poles of $A - BK$ while the ones for the observer dynamics are given by the poles of $A - GC$.

When choosing the poles one has to be very careful. In general the observer poles need to be faster than the closed-loop poles, since we want that the use of the observer does not decrease too much the performance with respect to the state feedback controller. We observed in practice that the fact of imposing very rapid poles for the observer leads to a noise amplification, thus a possible excitation of the high frequency system modes. This fact is presented in [41]. Consequently this will create a spillover effect (see Section 3.3), since the measurement noise is amplified. The same considerations are done for the closed-loop poles. Very fast closed-loop poles imply that: first, the voltage delivered by the controller might exceed the actuator limits of $\pm 100V$, thus possibly destabilizing the closed-loop system; second, the generated voltage might oscillate too fast in order to control the system. Thus, if the oscillating frequency is very high, the noise will be amplified, making the measurement impossible. One solution to this last issue is to select slower closed-loop poles but this will unavoidably lead to slower closed-loop response. We see therefore that a middle path needs to be found between the response time and the noise amplification.

By checking the open-loop system poles we find 8 complex conjugate poles (3 for the liquid sloshing and 5 for the plate), all of them having their real part negative. Thus the open-loop system is stable. The position of the open-loop poles can be seen in Figure 4.16, while their value is presented in Table 4.12 below.

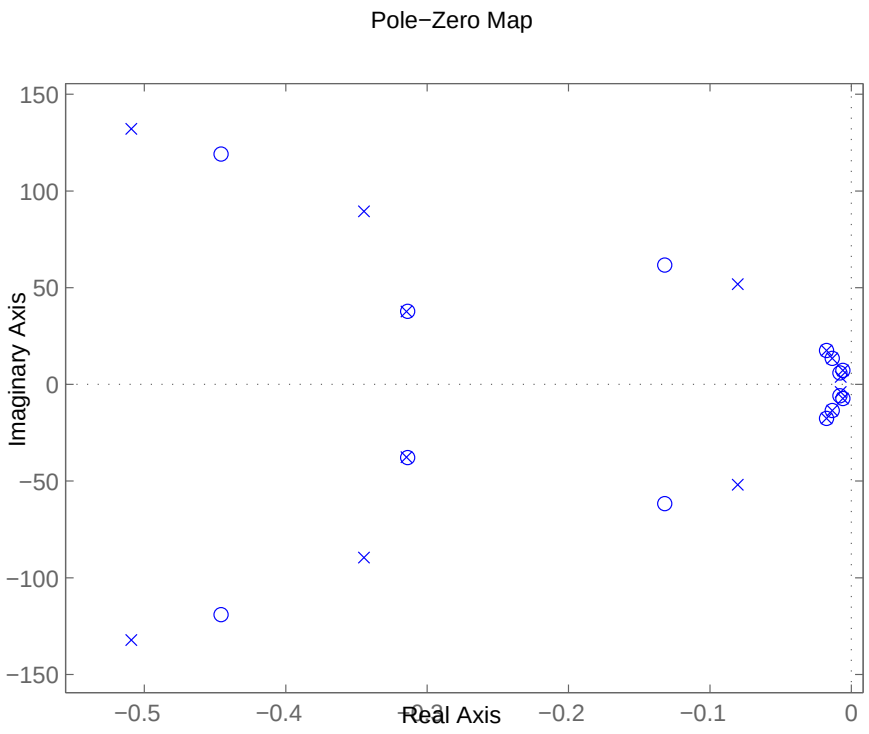

Figure 4.16: Pole/zero map of the open-loop system ($\times$ for the poles, $\circ$ for the zeros)

Since the procedure for the controller synthesis is identical for all the tank filling levels, details are given here only for the case when the tank fill level is 0.9. Let us first consider the choice of the pole placement controller K from Figure 4.15.

Open-loop poles	Closed-loop poles
-0.5093 ± 132.14i	-0.5093 ± 132.14i
-0.3447 ± 89.53i	-0.3447 ± 89.53i
-0.0803 ± 51.84i	-0.0803 ± 51.84i
-0.3146 ± 37.68i	-0.3146 ± 37.68i
-0.0175 ± 17.55i	-0.0325 ± 17.55i
-0.0135 ± 13.48i	-0.0384 ± 13.48i
-0.0059 ± 7.26i	-0.0333 ± 7.26i
-0.0074 ± 3.92i	-0.0324 ± 3.92i

Table 4.12: Closed-loop poles with the pole placement controller, tank fill level 0.9

The choice of the closed-loop poles is very difficult. The best solution is to change only the real part of the dominant poles. In this case, the best closed-loop poles are

given in Table 4.12. Concerning all the observer poles, their real part is three times bigger than the real part of the closed-loop poles.

The pole placement controller is tested on the experimental set-up for a plate displacement of 10cm at the free end. The controller response in attenuating the vibrations is presented in Figure 4.17, while the voltage delivered by the controller to make this attenuation is depicted in Figure 4.18.

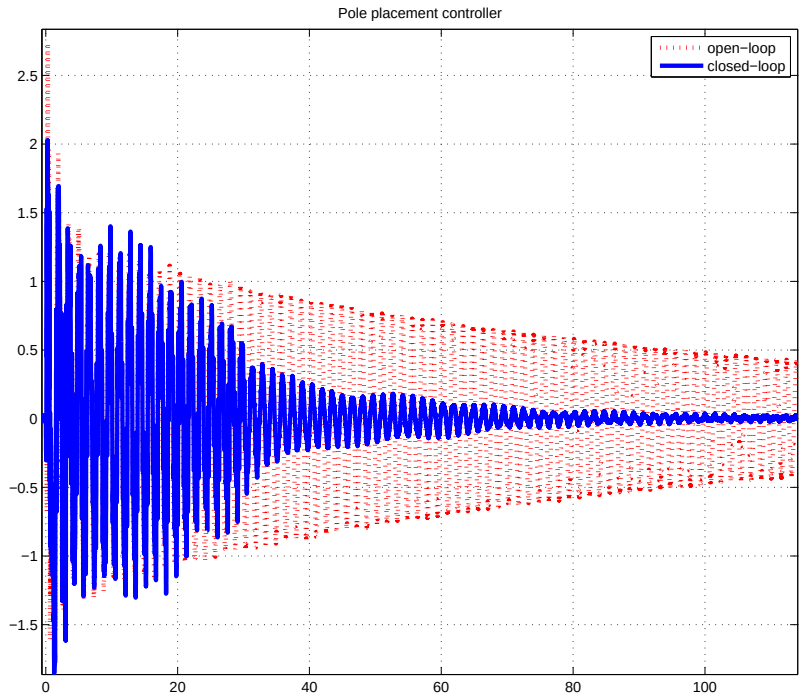

Figure 4.17: Experimental output of the of open-loop (dotted line) and closed-loop (plain line) systems using a pole placement controller with a tank fill level of 0.9

It is important to notice that since the voltage delivered by the controller exceeds the maximum value of the voltage amplifier $\pm 100V$, the real voltage delivered to the plate in the interval $0 \ldots 30$ seconds is actually between -100V and $+100$V.

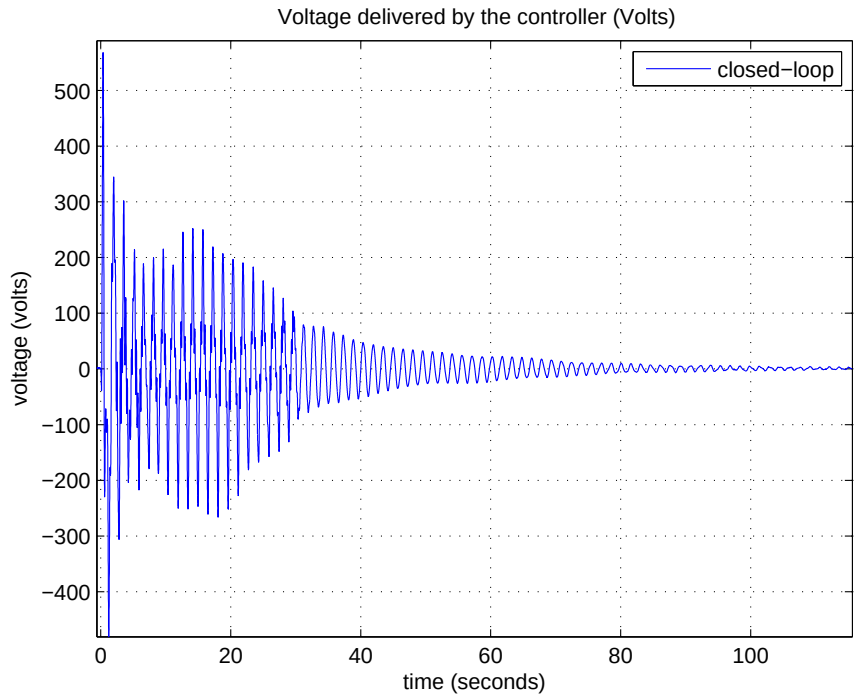

Figure 4.18: Voltage delivered by the pole placement controller during experiments, tank fill level of 0.9

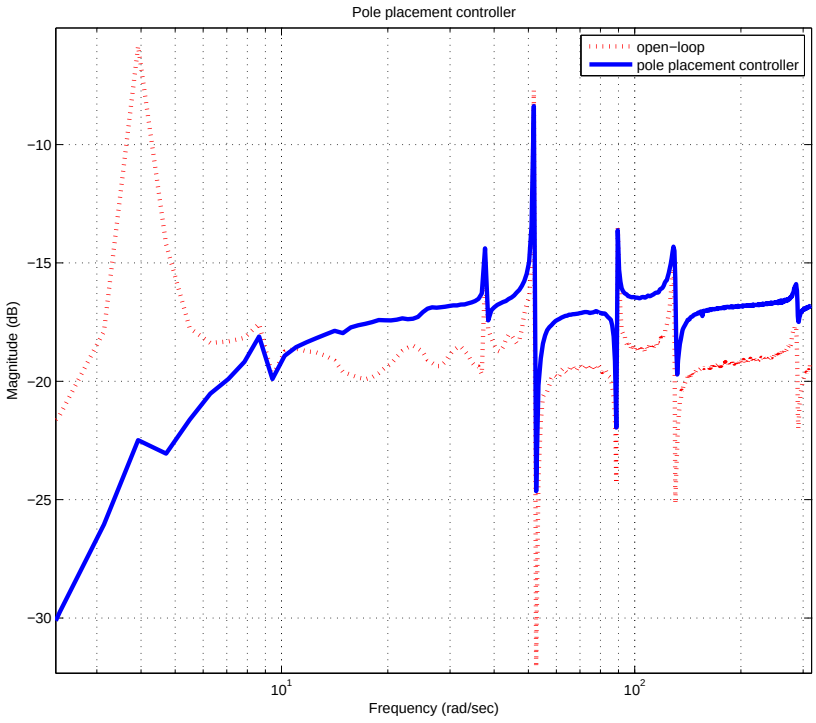

Figure 4.19: Frequency response of the pole placement controller, tank fill level of 0.9

The frequency response of the system in closed-loop with the feedback controller previously computed is presented in Figure 4.19. We can notice that the first mode is well attenuated and also the second mode (the 1st sloshing mode). We expected this to happen since the dominant poles, corresponding to the first mode of the plate and the first sloshing mode, are the ones that were mostly diminished. The other poles that were changed are corresponding to the other sloshing modes but their effect is not visible on the Bode plot. This might be due to their very small energetic contribution (see Table 4.1 in Section 4.2).

It is also interesting to notice that the 2nd flexion mode also experiences a small attenuation, even though the corresponding poles have not been changed. This might be an influence of the other poles that have been shifted.

At the same time, we notice that the peaks corresponding to the torsion mode and to the other flexion modes have a larger amplitude. This means that testing the controller for a high frequency input would not give the best results since the controller is not computed to attenuate the large frequency values.

Conclusion: In this section a pole placement controller coupled with a full-state observer have been constructed. The choice of the closed-loop poles is very tricky. After changing only the dominant poles, the computed controller can be tested on the experimental set-up. Temporal and frequency tests show that the controller is effective especially in attenuating the first flexion mode of the plate. In the next section we will compute a H_∞ controller. Finally, in Section 4.6 both controllers will be compared.

4.5 H_∞ robust controller

In this section a robust controller is computed and some experiments are performed. The controller is calculated using the theory detailed in Section 3.3 of Chapter 3.

In order to solve the robust control problem we write our system in the standard form given by Figure 4.20 where the following notation is used:

- u - system input (the voltage delivered by the H_∞ controller);
- y - measured system output (voltage delivered by the piezoelectric sensor);
- w - the perturbation of the system;
- z - the controlled outputs of the system.

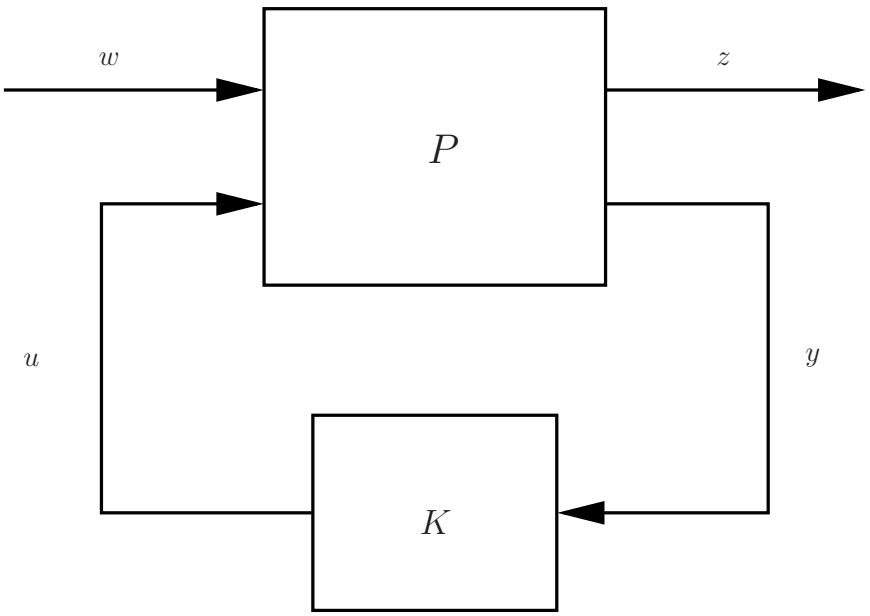

Figure 4.20: Standard H_∞ problem

We want to minimize the influence of the perturbation, stacked in the vector w, on the controlled outputs, gathered in the vector z.

During our tests we observed that care should be taken when choosing the outputs to be controlled. In our case, the controlled outputs stacked in the z vector are the position of the plate given by the piezoelectric sensor and the control generated by the robust controller K. The amplitude of the control is limited since the piezoelectric actuators have a $\pm 100V$ limitation in amplitude (their frequency limitation is not taken into account since they respond much faster than the system does). The

perturbation w will be a sinusoidal voltage sent to the second piezoelectric actuator patch glued on the plate.

We compute the H_∞ controller, with $M = 3$ modes of liquid sloshing and $N = 5$ plate's modes (see Section 4.2). The system is tested on the experimental set-up described in Chapter 1. The ability of the controller, under external perturbations, to suppress the system vibrations but also to eliminate the spillover effect when it appears, will demonstrate the validity of the controller.

Therefore, we followed two approaches in order to solve the robust control problem. These approaches lead to two types of models:

- model without filters. In this case, using a gain, we balance the control output delivered by the controller in order to have a maximum voltage of $\pm 100V$;
- model with filters (in particular to suppress the spillover effect).

4.5.1 Synthesis of a H_∞ controller without filters

Here, the H_∞ standard problem is applied to our problem. The complete state-space representation of the system and controller, is given by the equation set:

$$\left\{\begin{array}{rcl} \dot{x}(t) &=& Ax(t) + B_1 w(t) + B_2 u(t) \\ z(t) &=& C_1 x(t) + D_{12} u(t) \\ y(t) &=& C_2 x(t) + D_{22} u(t) \end{array}\right. \tag{4.2}$$

where $A \in \mathbb{R}^{16\times 16}$, $B_2 \in \mathbb{R}^{16\times 1}$, $C_2 \in \mathbb{R}^{1\times 16}$ and $D_{22} \in \mathbb{R}^{1\times 1}$ (the feedforward matrix is different from zero due to the model matching of Section 4.3.3). The system is perturbed by the mean of the matrix $B_1 \in \mathbb{R}^{16\times 1}$, similar in construction as the control matrix of the plate (see Proposition 2.2.2) except for the position of patch corners.

The to-be-controlled output z is composed of the plate position and the voltage delivered by the H_∞ controller. In order to assure that this voltage remains in the amplitude limits $\pm 100V$, we use a weighting under the shape of the matrix $D_{12} \in \mathbb{R}^{17\times 1}$:

$$D_{12} = \begin{pmatrix} 0 \\ \vdots \\ 0 \\ d_{12} \end{pmatrix}.$$

Moreover, the matrix $C_1 \in \mathbb{R}^{17\times 16}$ has the shape:

$$C_1 = \begin{pmatrix} C_2 \\ 0 \end{pmatrix}.$$

Other choices for the to-be-controlled output are of course still possible. Besides the plate position and the voltage delivered by the controller, we also made tests with the position of the first pendulum-mass system in the to-be-controlled output. This was done in order to better control the sloshing modes but, since the results are not satisfactory they are not recalled here. Preliminary tests are in progress by considering, in the to-be-controlled output, the state-space vector of the model instead of y, see [43].

Furthermore, for computation we use the Matlab© Robust Control Toolbox, and the controller we obtain is first tested in numerical simulation and then on the experimental setup.

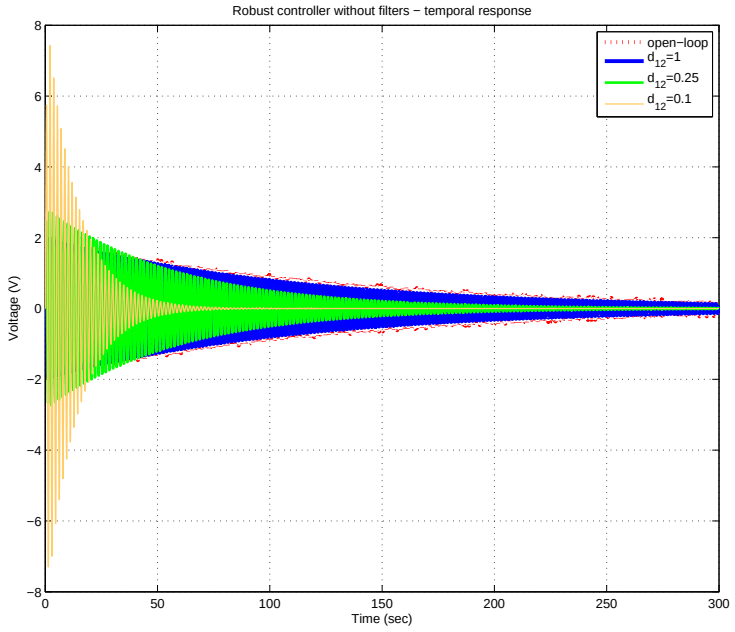

Figure 4.21: Temporal response for robust controllers using Robust Control Toolbox, without filters; simulations on a system with the same amount of modes; tank fill level equal 0.9. Thin line is obtained with $d_{12} = 0.1$, plain line with $d_{12} = 0.25$ and bold line with $d_{12} = 1$

First the value of d_{12} is equal to 1, in which case the controller needs to minimize u as much as possible. The controller is computed and is numerically simulated on a

system of the same dimension. The results are shown in Figure 4.21 and correspond to an initial condition of the system when the liquid is motionless and the plate free end undergoes a 10cm displacement from the equilibrium position. The voltage delivered by the controller is depicted in Figure 4.22. As it can be noticed the maximum voltage delivered is ± 12.75V which is far away from the actuator saturation level of ± 100V. Therefore, we decrease the value of the d_{12} coefficient. In this case, the voltage delivered by the controller will increase but in the same time the response time of the closed-loop system will decrease. This yields: $d_{12} = 0.25$ and $d_{12} = 0.1$. The results of the response time, in open-loop and in closed-loop, are given in Figure 4.21 while the voltage delivered by the respective controllers are given in Figure 4.22.

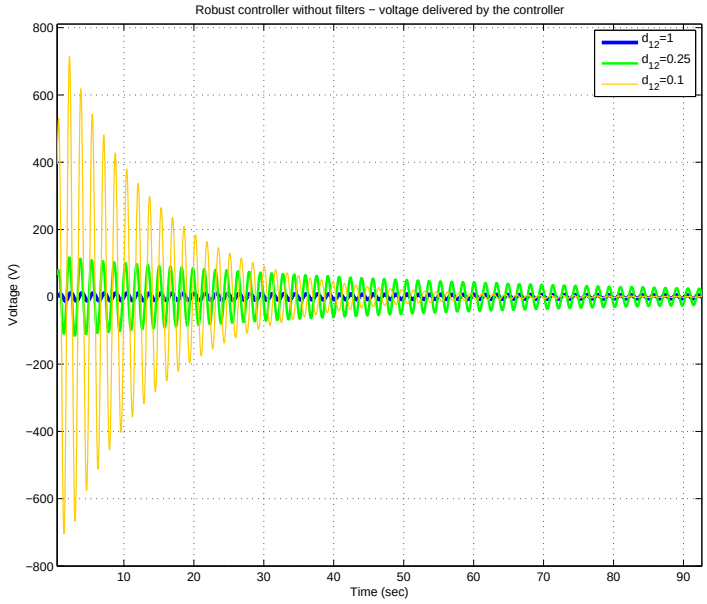

Figure 4.22: Voltage delivered by the robust controllers; tank fill level equal 0.9 with $d_{12} = 0.1$ (thin line), $d_{12} = 0.25$ (plain line) and $d_{12} = 1$ (bold line)

The next step is to numerically simulate these controllers on an augmented system. The main reason is to verify the presence or not of a spillover effect. We therefore consider an augmented system, where one plate mode has been added to the previous system. The frequency responses are shown in Figure 4.23 for all the previously considered controllers. We notice that all the controllers previously computed act strangely on the augmented system. Even though the high frequency modes are attenuated, the magnitude of the first modes (especially the magnitude of the first sloshing mode) is increased. Moreover, to visualize the spillover effect, the temporal response for the case when $d_{12} = 0.1$ is shown in Figure 4.24. The initial condition of

the plant is again equivalent to a free end's plate deformation of 10cm. The spillover existence can be easily noticed due to the signal divergence.

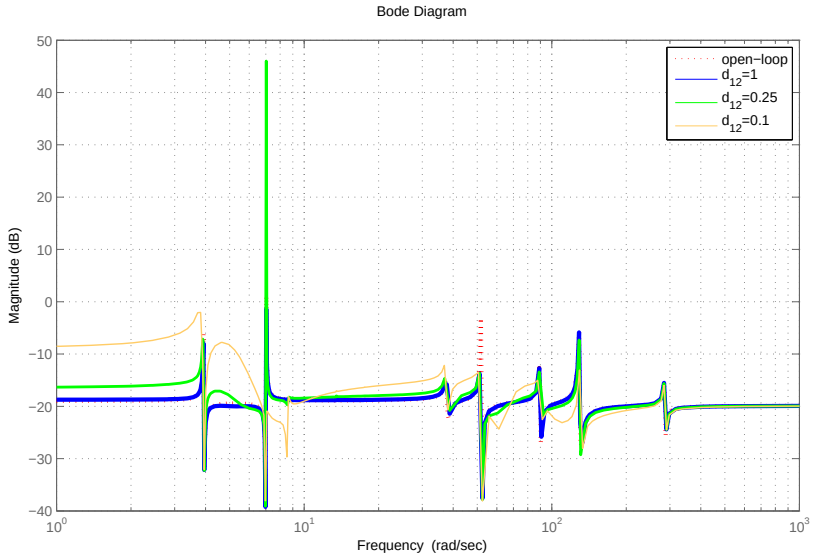

Figure 4.23: Bode plot of the robust controllers simulated on an augmented system; tank fill level equal 0.9. The thin line is for $d_{12} = 0.1$, plain line for $d_{12} = 0.25$ and bold line for $d_{12} = 1$

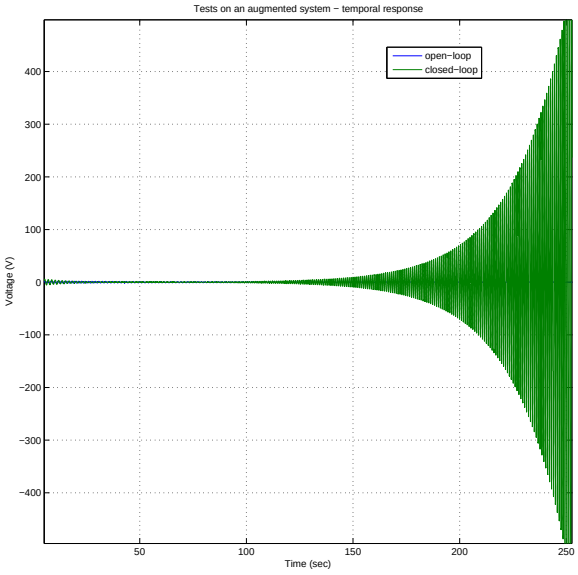

Figure 4.24: Temporal response for robust controllers using Robust Control Toolbox, without filters and with $d_{12} = 0.1$; tests on an augmented system; tank fill level 0.9

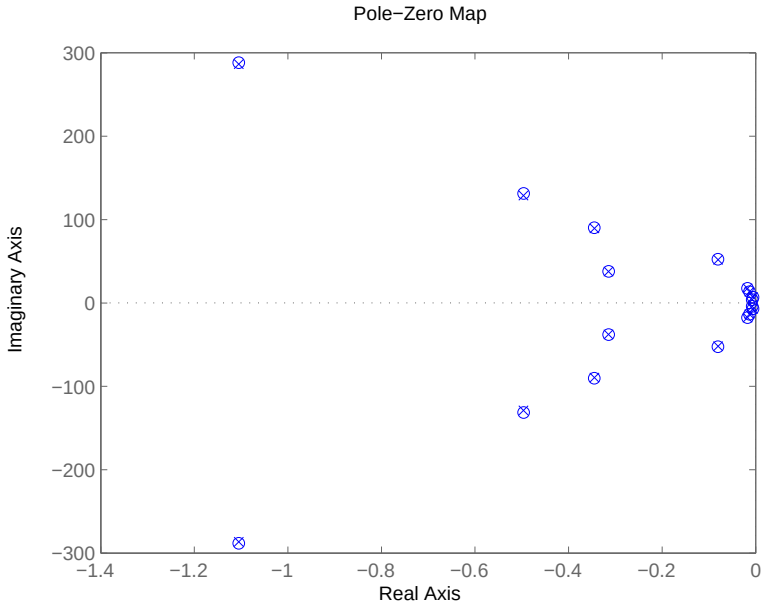

Figure 4.25: Pole/ zero map for the open-loop system augmented with one mode; tank fill level equal 0.9

The position of the poles and zeros, for the closed-loop system, can be seen in Figure 4.26. Some fast poles can be observed, much larger than the open-loop ones (see Figure 4.25) and also larger than the ones we experience earlier for the pole placement problem (see Table 4.12).

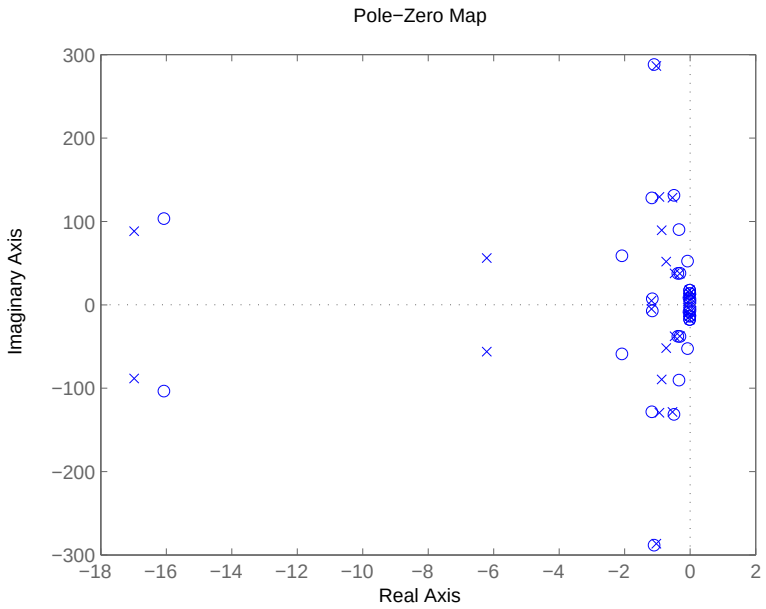

Figure 4.26: Pole/ zero map for the closed-loop system augmented with one mode and with the controller computed with $d_{12} = 0.1$; tank fill level equal 0.9

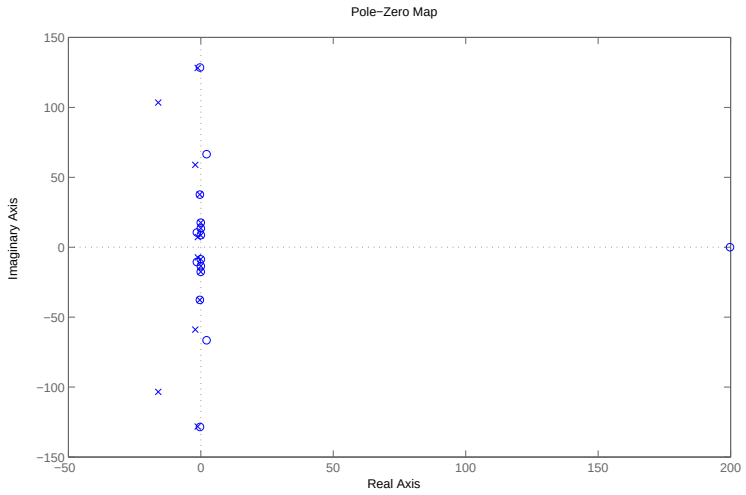

Figure 4.27: Pole/zero map of the previously computed controller, $d_{12} = 0.1$; tank fill level equal 0.9

In spite of all these problems, we tested all the previously computed controllers on the experimental setup. During all the tests we notice a sudden stop in the acquisition process just after the controller introduction. After analyzing the H_∞ controller poles from Figure 4.27, we notice the poles with large real part. We think that these poles are the cause for which the experimental tests are not working. Different manipulations are tried to overcome this issue.

A first idea is to eliminate the fast poles supposing *a priori* that they will not influence the system behavior in the steady state. Therefore, we eliminated the fast poles and we considered only their static gain. Recalculating the controller and testing it in simulation, we obtain a closed-loop settling time identical to the open-loop settling time. From this we draw the conclusion that the new controller is not working and the fast pole have a great influence on the controller behavior.

A second solution that comes to our mind is to select ourselves, in some way, the poles of the computed H_∞ controller. This is done by setting some allowance zones for the controller poles. We can therefore describe these zones using linear matrix inequalities (LMI) (see [39] or [38]). Our purpose is to compute this region so that the closed-loop poles are on the left-hand side of the complex plane and have their real part (in modulus) as big as possible. At the same time, we do not want to keep very fast poles since they might not be implemented on the experimental setup. The region needs to be found by making a compromise between these constraints.

Unfortunately, we did not find the suitable region. We found either regions where the poles are still very fast, thus unimplementable, or regions where the poles are

slow and the closed-loop settling time is identical to the open-loop one.

We thus finally deduce that this method is not implementable on the real system. One can think of a further study consisting in using an acquisition set-up that can handle a bigger sampling frequency. In this way, a clarification may be obtained.

4.5.2 Synthesis of a H_∞ controller with filters

The robust control of a system with filters gave us the best results on the experimental device and will be detailed below. These tests were already briefly presented in [117] and [118] and more details are given in this section.

The choice of the filters is a difficult problem and will have an impact on the controller behavior. Later on, we propose a choice of the filters and then we compute the controller using these filters.

In order to take the disturbances into account, the low-pass filter $H_1(s)$ is included in the design scheme. As explained in Section 3.3, it models the range of frequencies where all the modes of the finite dimensional system are considered (between 0 Hz and 21Hz, see Section 4.2). This perturbation, induced by a frequency generator device, is applied to the piezoelectric actuator that is not used in the control law. The perturbation will be a source of vibrations of the fluid-structure system and is modeled by a low-pass filter of order 1 with a bandwidth of 50 Hz. The filter, placed before the piezoelectric actuator used as a disturbance actuator has therefore a transfer function given by

$$H_1(s) = \frac{100\pi}{s + 100\pi}.$$

The residual modes divergence describing the spillover phenomenon is a common problem when working with a truncation of an infinite-dimensional model (see Section 3.3). In order to avoid this undesirable effect, a high-pass filter $H_2(s)$ of transfer function:

$$H_2(s) = \frac{(1 + \frac{s}{2\pi 27})^3}{(1 + \frac{s}{2\pi 160})^3}$$

is added on the controlled output. This allows to get a 60 dB attenuation above the cut-off frequency of 27 Hz where the cut-off frequency is slightly greater than the frequency of the last considered mode in the controller synthesis. The H_∞ controller is designed and is first tested through simulations and on the experimental set-up afterwards for the two different levels of tank filling (denoted 0.7 and 0.9). The model used for simulations is again a system of larger dimension, in order to test the existence of the spillover effect.

A controller is calculated using the following standard H_∞ problem given in Figure 4.28:

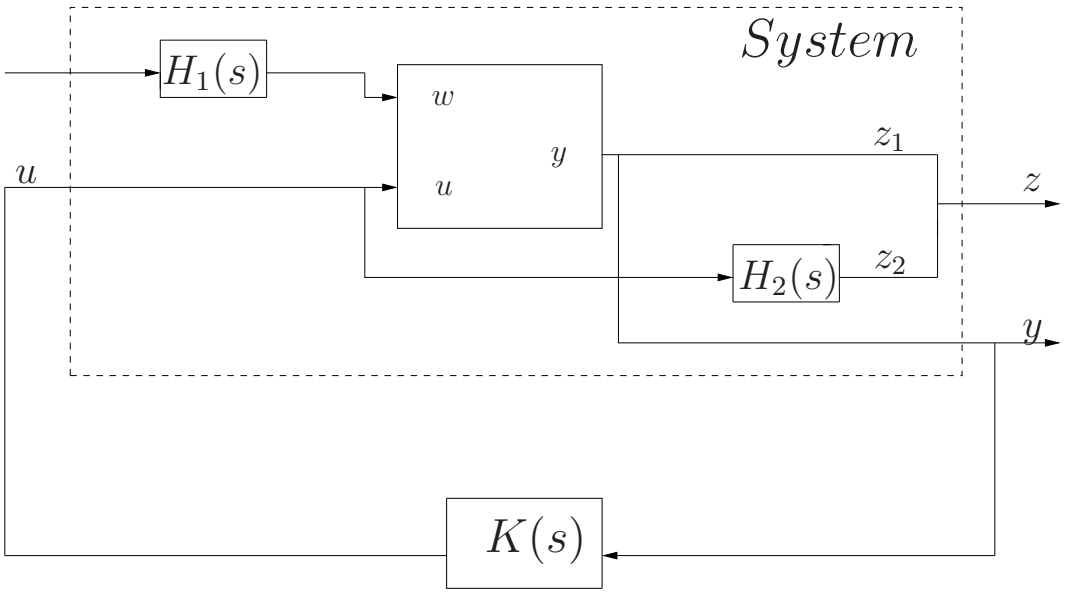

Figure 4.28: Standard H_∞ problem with filters

4.5.2.1 Matlab© Robust Control Toolbox controller

The first attempt to solve this problem is by using the Matlab© Robust Control Toolbox which allows the computation of only full order controllers. Tries are made and due to memory overflow, full order controllers cannot be computed for the system with $X_p \in \mathbb{R}^{10}$ and $X_\theta \in \mathbb{R}^6$ and both filters. This would lead to a full order controller of dimension 20.

One solution to solve this problem would be to reduce the number of modes in the model. After successive tries, we can find a configuration for which a controller can be computed but it contains only the first plate mode and the first liquid mode and no spillover filter. Instead of the filter, a gain is used in order to keep the control voltage in the desired limits. Therefore, in this section only, we consider one mode of the plate and one mode of the liquid: $X_p \in \mathbb{R}^2$ and $X_\theta \in \mathbb{R}^2$.

The results of the controller implementation are tested for only one tank fill level of 0.7. The results are given in Figure 4.29.

We can see that even though the controller attenuates well the first mode, we can not use this technique since it does not allow us to consider a greater number of modes or the roll-off filter in order to prevent spillover. For this simulation only, the

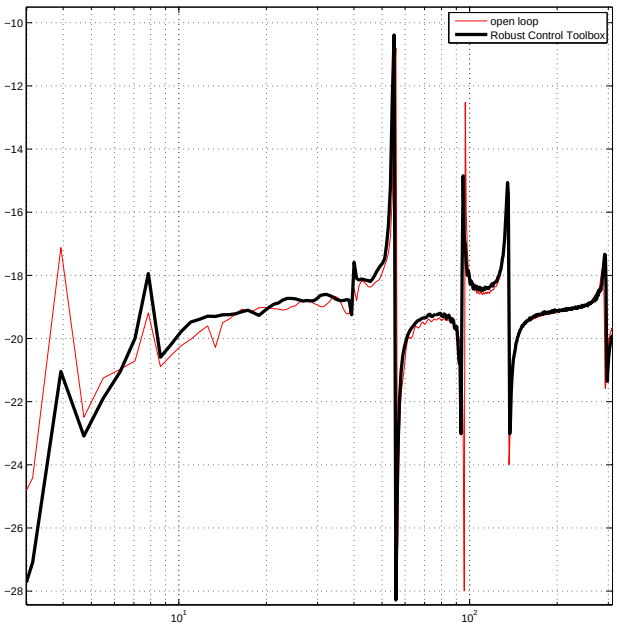

Figure 4.29: Experimental Bode plot of the open-loop system (plain line) and of the closed-loop system (bold line) computed with the Robust controller from Matlab for 2 modes and a fixed tank filling of 0.7

Simulink schema in Figure 4.28 used for the calculus of the controller has the $H_2(s)$ filter replaced by a gain suitably tuned. The roll-off filter is necessary to suppress the spillover phenomenon, thus maintaining the overall stability of the system. When performing numerical simulations, we experienced problems due to the non-desirable spillover (see Figure 4.24). We conclude that we cannot eliminate the roll-off filter from our controller synthesis.

Moreover, when using the Robust Control Toolbox, we select ourselves a suitable weighting function on the controlled output u so that the voltage delivered by the controller stays in the range $\pm 100V$, in this way the actuators do not saturate and the system stability is preserved. On the other hand, the Robust Control Toolbox cannot directly tackle the problem of simultaneous control for different filling levels in the tip-tank.

For all these reasons we decided to consider synthesis algorithms of reduced-order controllers and tackling also the simultaneous H_∞ control problem.

4.5.2.2 HIFOO controller

We will use here the HIFOO package for the controller computation. The algorithm is based on non-smooth optimization issued from [60] and [35] and it computes full order controllers but also reduced order controllers that are less demanding in terms of memory.

Before considering all the plate and liquid sloshing modes, we experiment the HIFOO controller on the previous system in order to compare it with the full order (second order in this case) Matlab© Robust Control Toolbox. Therefore, for this simulation only, the HIFOO controller is computed for a system with only one mode of the plate and one mode of the liquid: $X_p \in \mathbb{R}^2$ and $X_\theta \in \mathbb{R}^2$. Since HIFOO allows us to specify the order of the controller, in this case the resultant controller will be a first order. The comparison is given in Figure 4.30. We notice that, both controllers attenuate the first flexion mode with around 4dB ($\sim$ 7dB for HIFOO) but not the first sloshing mode, which they actually amplify. Moreover, the HIFOO controller amplifies also the torsion mode and the frequency mode at 50Hz, modes that have not been considered in the controller synthesis.

One very important thing to notice is that, while increasing the number of considered modes, HIFOO always finds a suitable controller, in the presence of both filters from Figure 4.28 and by keeping the voltage delivered by the controller in the allowed range.

Some experiments are also performed for a tank fill level of 0.9 in the same configuration (1 mode for the plate and 1 for liquid sloshing). The results are given in Figure 4.31. Since the controller was built with only the first two modes, we notice that only these modes are attenuated, the first mode attenuation being of almost 13 dB. A slight attenuation is also noticed for the second and third flexion modes (2.3 dB and 1 dB respectively) even though those modes were not taken into account for the controller design. We also notice an amplification of the torsion mode (0.5 dB) and of the forth and fifth flexion mode (1 dB and 1.7 dB respectively) comparing to the open-loop case.

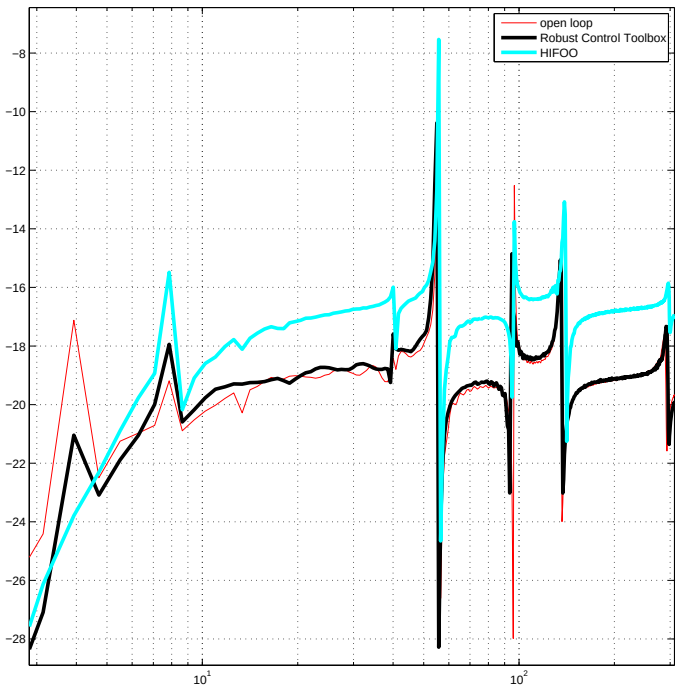

Figure 4.30: Experimental Bode plot of the open-loop system (thin line) and of the closed-loop system using a HIFOO controller and a Robust controller computed with Matlab (2 modes and a fixed tank filling of 0.7)

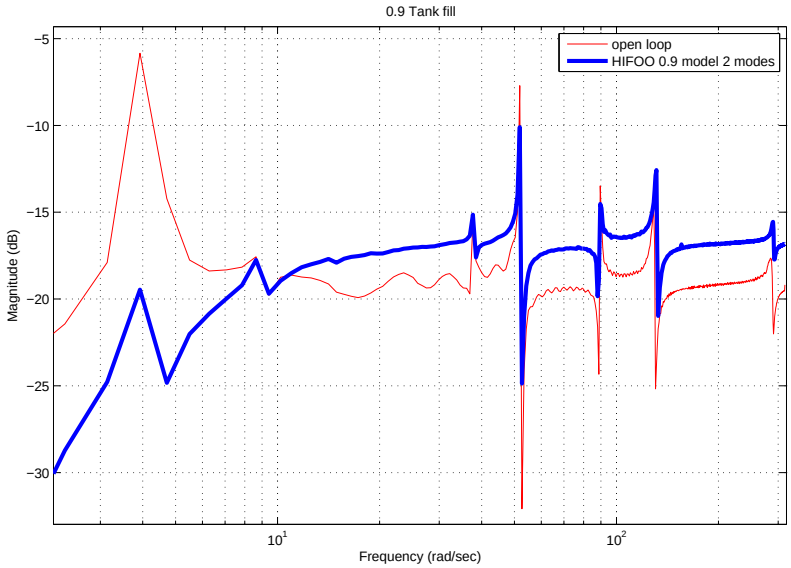

Figure 4.31: Experimental Bode plots of the open-loop system (thin line) and the closed-loop system (bold line) with a HIFOO controller computed for 2 modes and a fixed tank filling of 0.9

Analyzing the figures presented earlier, two conclusions can be drawn. The first is that HIFOO algorithm needs to be chosen instead of the usual Robust Toolbox from Matlab due to the reasons detailed before. Second, a larger number of modes definitely needs to be considered during the controller computation even in the case when HIFOO is used, in order to avoid mode amplification.

From this section on, controllers are computed using the suitable amount of modes needed for the system ($N = 5$, $M = 3$), in agreement with the theory in Section 3.1 of Chapter 3 and implemented in Table 4.1.

We considered one specific controller for each tank filling level. In order to choose the suitable order of these HIFOO controllers, H_∞ controllers of different orders for a fixed tank filling of 0.7 are computed using the standard H_∞ problem from Figure 4.28. The analytic computations show that controllers of order 1 and 4, have almost the same H_∞ norm γ: $\gamma = 4.24$ for a 1^{st} order and $\gamma = 4.28$ for a 4^{th} order.

Consequently, a 4^{th} order controller and a 1^{st} order controller for the same tank filling $e = 0.7$ are tested on the plant. The idea is to see if greater order controllers are really more efficient than a very simple first-order controller.

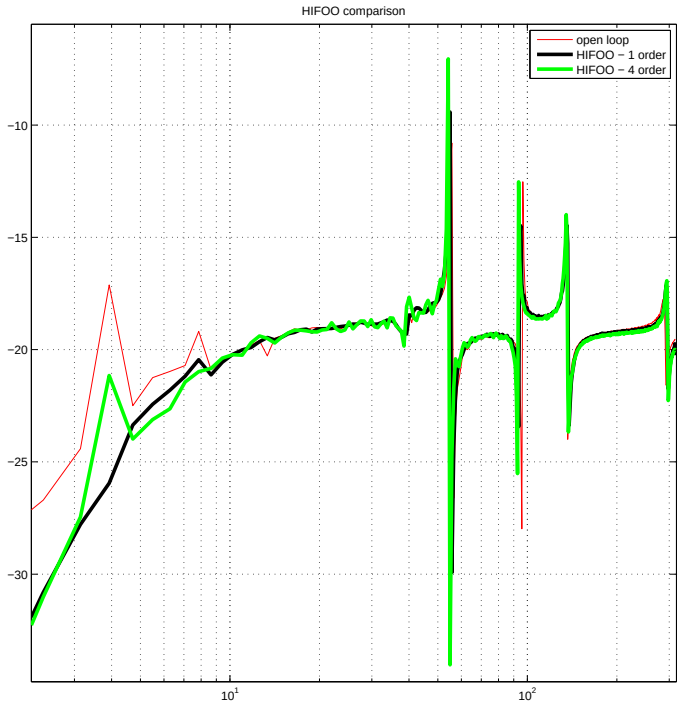

Figure 4.32: Comparison between a 1^{st} and a 4^{th} order HIFOO controller; experimental results for a fixed tank filling $e = 0.7$ and comparison to the open-loop system (thin line)

The experimental results are plotted in Figure 4.32. The Bode plots show the closed-loop attenuation in the case of a 1^{st} order and 4^{th} order controller computed using HIFOO. One can notice a slightly better attenuation for the first sloshing mode in case of the 4^{th} order controller and a better attenuation (almost 4 dB) for the first flexion mode in the case of the 1^{st} order controller.

Consequently, we infer that the complexity of a 4^{th} order controller is not justified. Therefore, from now on, only first-order controllers will be computed with HIFOO.

4.5.2.3 First order HIFOO controller

We compute a first order HIFOO controller for each tank fill level: $e = 0.7$ and $e = 0.9$. Experimental results are given in Figures 4.33 and 4.34 for each case.

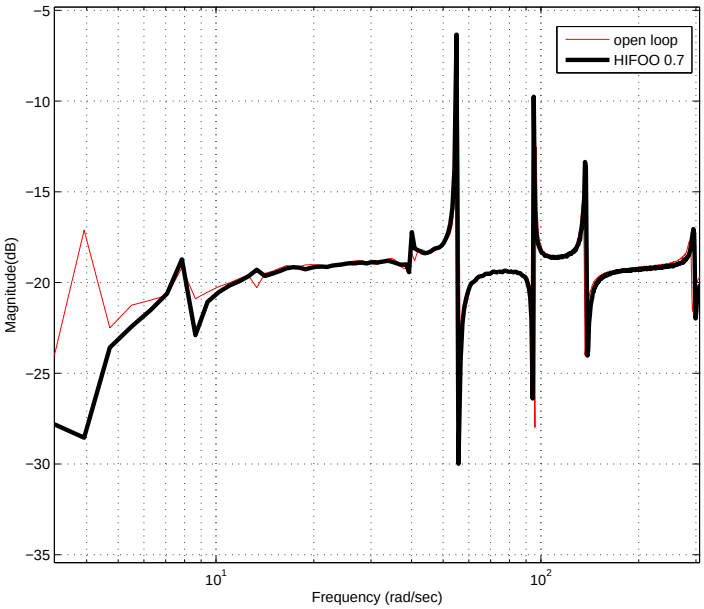

Figure 4.34: Experimental Bode plots for the open-loop system (plain line) and of the closed-loop system (bold line) using HIFOO controller - $e = 0.7$

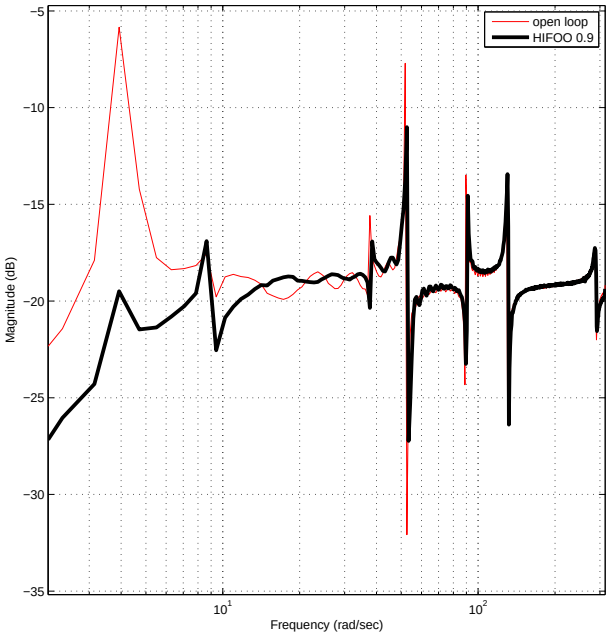

Figure 4.33: Experimental Bode plots for the open-loop system (plain line) and of the closed-loop system (bold line) using HIFOO controller - $e = 0.9$

It may be observed that the first peak is well attenuated for the different considered tank fillings. An attenuation of 14 dB is measured when $e = 0.9$ and of 11.7 dB

when $e = 0.7$. Concerning the first torsion mode (3^{rd} peak on the Bode plots) the attenuation is very small for $e = 0.7$ and quite good for $e = 0.9$ (1.5 dB). For higher order modes, one can see that the controller for $e = 0.9$ is also quite efficient.

Moreover, the HIFOO controller computed earlier, is tested on the experimental setup in the case of a plate displacement of 10cm on the free end. The temporal response of the controller is given in Figure 4.35 and the voltage delivered in Figure 4.36. As it can be seen, the voltage delivered is much lower than the actuator limits.

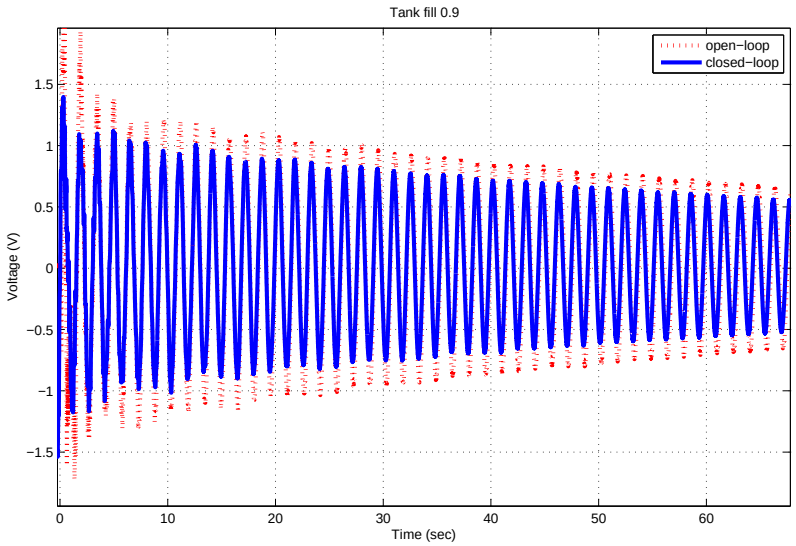

Figure 4.35: Experimental output of the closed-loop controller using HIFOO controller (bold line) and of the open-loop (dotted line); plate deformation of 10cm, $e = 0.9$

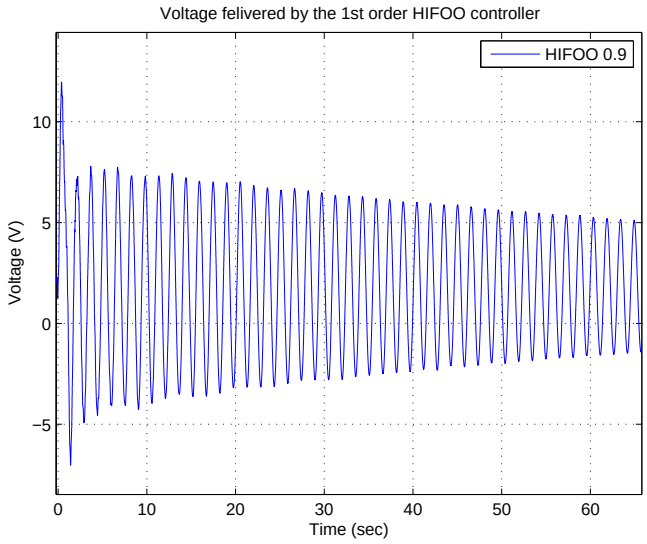

Figure 4.36: Voltage delivered by the HIFOO controller; plate deformation of 10cm, $e = 0.9$

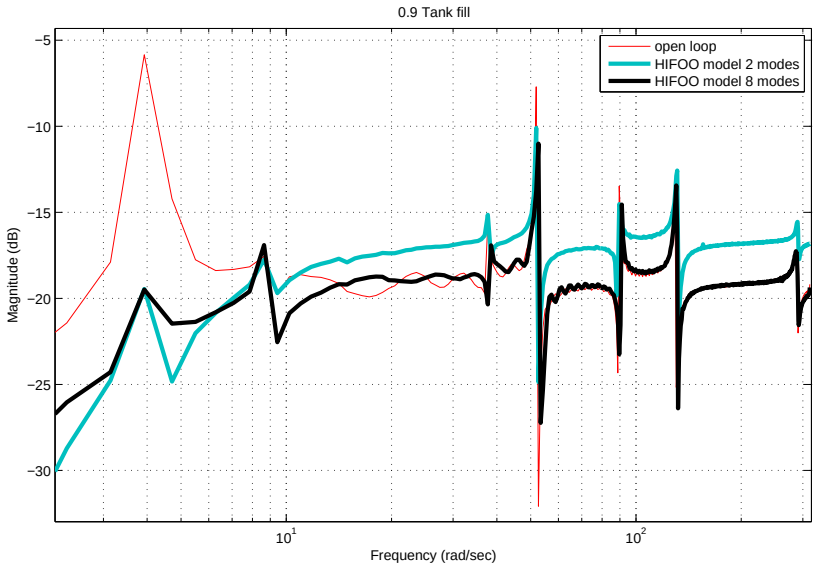

Figure 4.37: Experimental Bode plot, comparison between the open-loop (plain line) and the closed-loop system with HIFOO computed considering 2 or 8 modes of the system; fixed tank filling of 0.9

It is also very interesting to compare this HIFOO controller with the one computed when only 1 plate mode and 1 sloshing mode are considered. This is done in Figure 4.37 for the case of 0.9 tank fill level. As one can see, the results of the controllers are similar on the first two modes, as we expected. On the contrary, for all the other modes, we notice a better attenuation for the HIFOO controller computed with the 8 modes. Moreover, in this case, the torsion and last flexion modes,

which were amplified by the HIFOO controller computed with only 2 modes, are now slightly attenuated.

A conclusion of this part is that the first flexion mode, which is the most important in terms of plate displacement from its equilibrium position as well as in terms of modal energetic contribution (see Table 4.1), is well attenuated for all the cases (2 and 8 modes considered for the controller computation). Moreover, considering a larger amount of modes in the controller synthesis is not only done to match some theoretical criteria (energetic contribution of modes, presence of a torsion mode) but actually shows better results in the implementation on the experimental set-up.

4.5.2.4 Simultaneous reduced-order HIFOO controller

In practice the liquid in the plane tanks is varying during flight. Therefore, one controller must be valid for different fillings.

As a first step we test the 1^{st} order controller previously calculated for the tank 90% filled on a tank 70% filled. The idea behind this is to see if the controller is robust enough concerning such a model change. One can notice from Figure 4.38 that the controller increases the amplitude of the first vibration mode of the plate and does not attenuate the other modes.

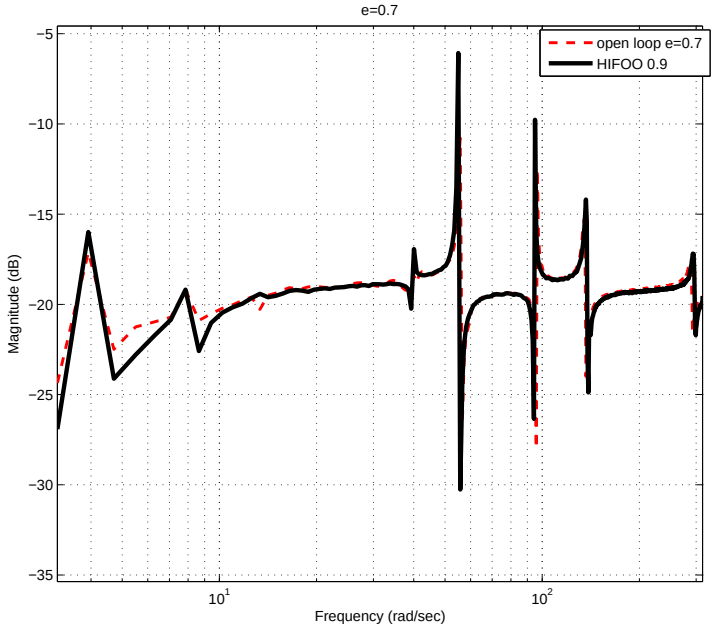

Figure 4.38: HIFOO controller calculated for the tank fill level 0.9 and tested on the tank fill 0.7

Consequently it is normal to consider a simultaneous 1^{st} order robust controller

computed for different levels. This simultaneous analysis is possible using the HIFOO package under Matlab©.

In this case, we also consider also another filling level of the tank: tank half full for which $e = 0.5$. Therefore, the simultaneous controller is computed for three fill levels ($e = 0.5$, $e = 0.7$ and $e = 0.9$). The results are given in Figures 4.39, 4.40 and 4.41. Each figure shows the experimental Bode plot of the open-loop device and the experimental Bode plot of the closed-loop using the same simultaneous HIFOO controller.

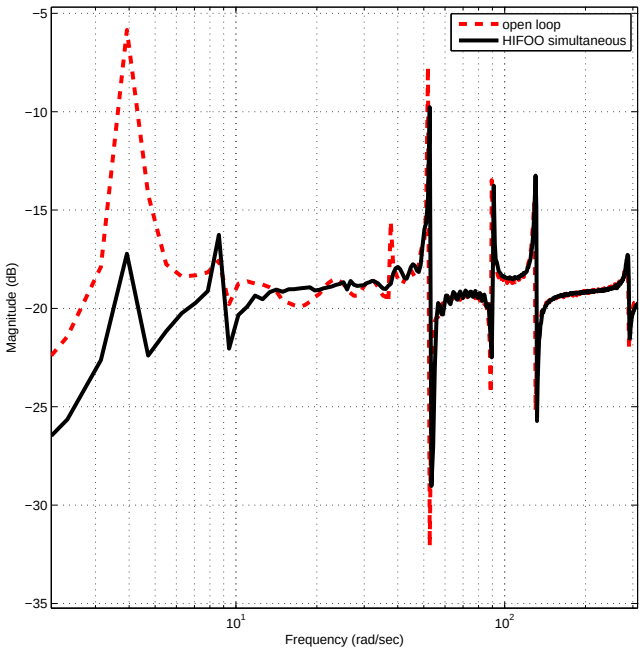

Figure 4.39: Experimental Bode plot of the open-loop system (dotted line) and of the closed-loop system (bold line) using simultaneous HIFOO controller - $e = 0.9$

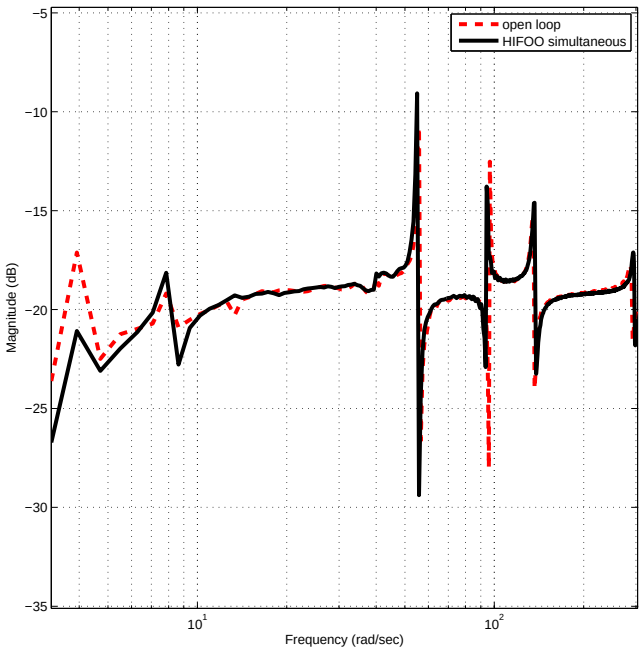

Figure 4.40: Experimental Bode plot of the open-loop system (dotted line) and of the closed-loop system (bold line) using simultaneous HIFOO controller - $e = 0.7$

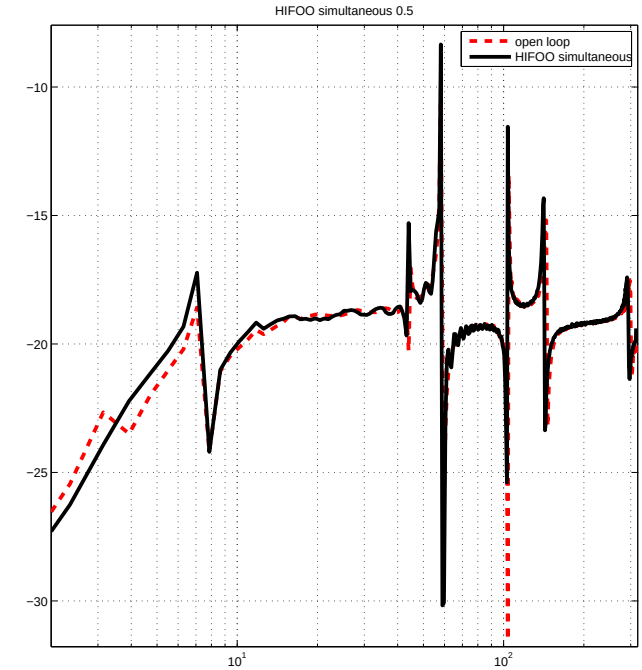

Figure 4.41: Experimental Bode plot of the open-loop system (dotted line) and of the closed-loop system (bold line) using simultaneous HIFOO controller - $e = 0.5$

One can observe that the first mode is very well attenuated for $e = 0.9$ (10dB) and $e = 0.7$ (5.7dB) and only a few for $e = 0.5$ (1.5dB). Regarding the torsion mode and higher order modes, they are also well attenuated especially for $e = 0.9$. Unfortunately, they are not at all attenuated for $e = 0.5$. This issue is normal since the simultaneous controller will create a mean level of attenuation for all the considered cases.

4.6 Comparison of the control methods

This section aims at comparing the two control methods: pole placement feedback controller and H_∞ controller. Two configurations are analyzed: a response to an initial plate deformation and the Bode frequency response.

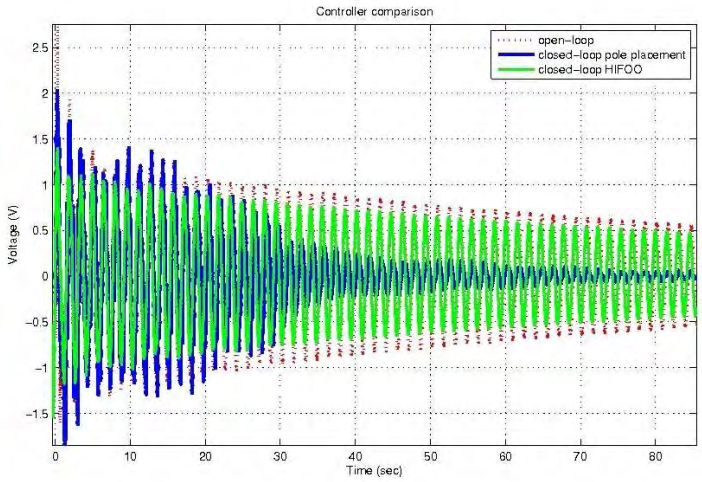

Figure 4.42: Temporal evolution of the experimental output for the closed-loop systems with pole placement controller (plain line) and HIFOO controller (bold line); plate free end deformation of 10cm, $e = 0.9$

First of all, let us consider the case of the plate free end deformation of 10cm. In this case the Figures 4.17 and 4.35 are compared in Figure 4.42. As it can clearly be seen, the pole placement controller attenuates the plate oscillations much better than the HIFOO controller does. This is normal, since the test configuration advantages the pole placement controller. For this controller, the dominant poles, which are corresponding to the first vibration and sloshing modes, were the one mostly changed (see Table 4.12). Also, the robust controller is set to minimize the influence of the perturbations on the voltage generated by the controller. Thus, the voltage generated to control the plate movements, is minimized for the HIFOO case while for the pole

placement case is left free. This is clearly seen when comparing the voltage delivered by both controllers: $\sim$ 500V (see Figure 4.18) for the pole placement controller and only $\sim$ 15V (see Figure 4.36) for the HIFOO controller.

Now, let us consider the Bode plots of the closed-loop systems. In this case, Figures 4.19 and 4.33 are compared on Figure 4.43. It can be easily seen that even though the pole placement controller attenuates more the first flexion mode, as we expected, the HIFOO controller attenuates more the other high frequency modes and even attenuates the modes that were amplified by the former controller.

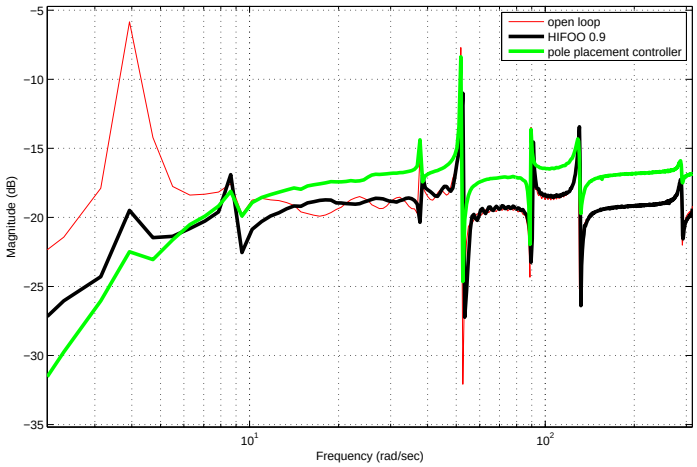

Figure 4.43: Experimental Bode plots for the closed-loop system with pole placement controller (plain line) and HIFOO controller (bold line); frequency response, $e = 0.9$

Until now we can not give a decisive response about the best controller. This depends on the type of problem to be solved. If one knows that the structure will vibrate most of the time along the first flexion mode, then the pole placement controller is the best choice. On the other hand, if we consider that the frequency range in which the plate vibrates is large, we will prefer the HIFOO controller.

However, probably the most important issue also needs to be kept in mind. This is the size of the controller. Actually, until now we compared a full order controller of order 20 with a single order controller of order 1. When the computation time and power are limited this issue is crucial and can be decisive in considering the HIFOO controller.

Conclusion: In this section a controller robust to external perturbations has been computed and tested on the experimental set-up. We employed the Matlab© Robust Control Toolbox and the HIFOO library. Due to memory overflow, the full order

controllers computed using Robust Control Toolbox can not be implemented. Therefore, a first order order controller using HIFOO library is computed and implemented. Finally, again using HIFOO, a unique first order controller that can take into account different fill levels of the tank is computed and tested for different fill levels $e = 0.5$, $e = 0.7$ and $e = 0.9$. Experiments show a good attenuation especially of the most energetic mode of the structure.

4.7 Conclusion of the chapter

In this chapter, tests on the experimental device are conducted. After proving that the influence of actuator dynamics on the system behavior is null for the frequency band we consider, the number of modes for the state-space approximation have been determined. In this case we used the method of modal energetic contribution from Chapter 3 along with some technical aeronautical aspects. Then, we computed the natural frequencies of the plate and the sloshing frequencies of the liquid. For this we first used the analytic method, which was verified by a numerical method, and then we directly measured the frequencies. The damping is then measured and the complete model is determined.

Afterward, we proceeded to the control of the structure. We first realized a pole placement control, that proves to be very effective for the case when the plate is deformed along the first flexion mode. Moreover, since the frequency response of the pole placement is not suitable for high frequencies, we computed a robust controller. Since the Matlab© Robust Control Toolbox fails to do this, the HIFOO algorithm is employed. Using HIFOO, we computed first order controllers that showed their effectiveness during experiments. Moreover, using HIFOO we were also able to make simultaneous control for three different tank fill levels, an impossible thing to do with the Robust Control Toolbox from Matlab© .

General conclusion

Contribution of the manuscript

The device we are working on was described in Chapter 1 and pictured in Figure 1.1. It is composed of a rectangular plate connected to a cylindrical tank filled with liquid up to an arbitrary level. Moreover, as it was already said, it was built to have, in low frequency domain, the same behavior as a real plane wing with liquid.

Therefore, we started the manuscript by presenting this experimental device along with the acquisition chain that connects it to the computer, the purpose of this work being to control the plate vibrations when they occur. Moreover, since the control of the device is done through piezoelectric actuators and sensors, the first chapter ends with a short presentation of the piezoelectric phenomenon.

We computed in Chapter 2 an analytical model of the device. The chapter is divided in three distinctive parts: the first part contains the model of the rectangular plate and the second details the model of the tank with liquid. In order to complete the model of the device, the third part studies the mutual interaction between the vibrations of the plate and the sloshing of the liquid in the tank.

On the one hand, we considered the plate model in Section 2.2. For sake of simplicity, we started from the PDE model of a beam, which represents the plate transposition in a 1-dimensional space. Using the Ritz method, we determined, for each mode of the beam, the expression of its natural frequency and associate deformation. We then considered the PDE model of a rectangular "clamped-free-free-free" plate (2.27). We computed the deformation of the plate based on the deformations of two theoretical perpendicular beams. Since, as it was proved later in Section 4.2 of Chapter 4, the first modes of the plate are the most energetic ones, we made an approximation of the PDE plate model by considering only the first modes. Based on this, we constructed the dynamic matrix, considering that all the vibration modes are decoupled even in the presence of damping. Then, studying the behavior of the

piezoelectric actuator, we computed the control matrix. We finally obtain the output matrix from the behavior of the piezoelectric sensor.

On the other hand, we studied the modeling of the sloshing of the liquid in the tank. Since there are no analytical results for horizontal cylindrical tank, we made a geometric approximation in Section 2.3. Therefore, we constructed a "virtual" rectangular tank for which the sloshing frequencies of the liquid are exactly the same as the one of the cylindrical tank. Then, we computed the PDE model of the liquid in the rectangular tank (see equations (2.67) and (2.68)). In order to develop a finite dimensional approximation, we made an analogy with a mass-pendulum mechanical system. Therefore, considering one mass-pendulum system for each liquid mode, the parameters of the mechanical systems were computed to develop the same force and moment of force as the liquid does. Once the parameters of the mass-pendulum systems were set, the computation of the corresponding dynamic, control and output matrices was straightforward from the pendulum equation.

We finally studied in Section 2.4 the influence of the plate vibration on the liquid sloshing and vice-versa. The plate senses the liquid sloshing as an external moment that bends the plate along with the piezoelectric actuators. At the same time, the liquid senses the plate influence as an external acceleration that amplifies the sloshing effect. Therefore, we first coupled both PDE models and second we detailed the finite dimensional approximation coupling. The complete model of the experimental device, under the shape of a state-space representation, was finally given by equation (2.134).

Chapter 3 has mainly a theoretical interest. We proposed first in Section 3.1 a method that allows to compute the finite dimensional approximation by studying the energetic contribution of each mode of the structure. Then, we detailed in Section 3.2 the theory of pole placement controller coupled with a full state observer. Since we were planning to implement controllers robust to external perturbations, we also briefly presented the robust H_∞ framework in Section 3.3.

Tests on the experimental device are illustrated and analyzed in Chapter 4. After checking the influence of the actuator dynamic on the plate vibrations in Section 4.1, we applied the energetic method detailed in the previous chapter to determine in Section 4.2 the number of modes for the finite dimensional approximation of the PDE model. Then, an analytic calculus, coupled with some numerical verifications and experimental measurements, is done in order to compute the natural frequencies and damping of each system mode. Moreover, we also proved by experimental measure-

ments that the presence of the extra weight of the tank filled with liquid decreases the plate natural vibration frequencies while the plate presence decreases the sloshing frequencies when connected. Since we observed minor differences between the frequency response of the computed model and the experimental set-up, we performed a model matching in order to diminish these mismatches.

In Section 4.4, we computed and tested the pole placement controller. Tests on the experimental device show a good attenuation of the plate vibrations when the plate is initially deformed along the first vibration mode. This can be easily explained, since the closed-loop poles corresponding to the first vibration modes are the ones that changed their position. However, on the Bode plot, we notice an amplification of some high frequency modes, a sign that the controller response in high frequencies will not be as good as in low frequencies.

Furthermore, in Section 4.5, we computed a controller robust to external perturbations and which attenuates a higher range of frequencies. Two distinct cases were considered. First, no filters were used to simulate the perturbations or to counter the spill-over effect that may occur. The controller was computed using the Matlab© Robust Control Toolbox. Simulations on a system with the same amount of modes showed a good attenuation of the plate vibrations while tests on an augmented system showed that the system diverges. This is due to the spill-over effect and thus the presence of the filter on the system input u is necessary. Moreover, tests on the experimental device could not be performed, probably due to the controller poles which were too fast. Therefore, in the second set of tests, filters were used. The first surprise was to notice that Matlab© Robust Control Toolbox fails to compute a controller when the filters plus a large amount of system modes are considered. An alternative had to be found and the HIFOO algorithm was considered. In contrast with Robust Control Toolbox which computes only full order controllers, HIFOO computes also reduced order ones. Using HIFOO, we computed 1^{st} order controllers for two different tank fill levels: 0.9 and 0.7. Experimental Bode plots showed a good attenuation especially for the first vibration modes. Tests for a plate deformation along the first vibration mode showed also good results. Finally, using again HIFOO, we tackled the problem of simultaneous control of the system for different filling levels. We computed a 1^{st} order controller that simultaneously attenuates the vibrations for three tank fill levels: 0.9, 0.7 and 0.5. Here also, attenuation is obtained, especially for the first vibration mode.

Finally, Section 4.6 contains the comparison of the different control methods we employed. As expected, pole placement controller showed a better result when the

plate is deformed along the first vibration mode while HIFOO controller showed better results when a large frequency spectrum is considered. Finally, based on the controller size (full order pole placement controller versus the 1st order HIFOO controller) the HIFOO controller was considered the most suitable.

Perspectives and Open questions

There are still many points that may be considered. Some of them concern the model construction while others concern the vibration control or the perturbation design. Let us detail some of them here below.

As stated in the introduction of Chapter 2, there are two different approaches for the computation of the model: analytical (the approach we followed in this manuscript) and numerical. One of the main reasons for which we choose the analytical approach was the possibility to model the sloshing of the liquid. However, we found that some recent toolboxes from a FEM software can also solve this. Therefore, this issue could also be exploited in order to compare a numerical model using this approach with the analytical one obtained here. Concerning the analytical model, some model improvements could be worked on if we consider the nonlinear dynamics of the actuators and sensors. In particular, it is well known that piezoelectric actuators and sensors have a limited deformation [94] or [131].

Concerning the control of vibrations, there are issues that require further attention. For example the choice of weighting functions for the robust H_∞ control. We know, from the literature [145, Chapter 6.3], that the choice of the weighting functions is extremely important for the results we obtain. The choice of the to-be-controlled outputs could also be addressed differently. Tests are in progress using the system state X in the controlled outputs [43] instead of the measured output y as we did. Preliminary results show a better attenuation (than the one we experienced with HIFOO) when a large spectral frequency is considered but a smaller attenuation, for the first mode, than the one we observed with the pole placement controller. Another interesting issue should be to study the interest of a mixed synthesis H_2/H_∞. Moreover, methods that better control the liquid sloshing or the twisting modes of the plate could also be of great interest.

Concerning the perturbations, until now we used a random chirp of constant amplitude. A more sophisticated perturbation, that uses a vibrating device connected to the clamped side of the plate, could be considered. Besides, a more sophisticated device that excites more the torsion of the plate or the sloshing modes may be used. In any case, paths for further research on this device are numerous, some of them (probably the most interesting ones!) are still to be discovered ...

Bibliography

[1] *PI Ceramic*. PI Ceramic GmbH, Lindenstrasse, 07589 Lederhose Germany. http://www.piceramic.de/pdf/KATALOG_english.pdf.

[2] H.N. Abramson. The dynamic behavior of liquids in moving containers, with application to space vehicle technology. Technical Report NASA SP-106, NASA, Washington, DC. USA, 1966.

[3] M.J. Abzug. Fuel slosh in skewed tanks. *Journal of Guidance, Control and Dynamics*, 19(5):1172–1178, 1996.

[4] M.J. Abzug and E.E. Larrabee. *Airplane Stability and Control: a history of the technologies that made aviation possible, second edition*. Cambridge University Press, 2002.

[5] S.S. Ahmad, J.S. Lew, and L.H. Keel. Robust control of flexible structures against structural damage. In *Proceedings of the American Control Conference*, Philadelphia, PA. USA, June 1998.

[6] M. Amabili. Free vibrations of partially filled cylindrical shells. *Journal of Sound and Vibration*, 191(5):757–780, 1996.

[7] M. Amabili and G. Dalpiaz. Breathing vibrations of a horizontal circular cylindrical tank shell, partially filled with liquid. *Journal of Vibration and Acoustics*, 117(2):187–191, 1995.

[8] K. Ammari, A. Henrot, and M. Tucsnak. Asymptotic behavior of the solutions and optimal location of the actuator for the pointwise stabilization of a string. *Journal of Asymptotic Analysis*, 28:215–240, 2001.

[9] P.J. Antsaklis and A.N. Michel. *Linear systems*. Birkhäuser, 2006.

[10] APEX Microtechnology Corporation. *APEX PB 58 datasheet*. http://www.datasheetcatalog.org/datasheet/ApexMicrotechnologyCorporation/mXsrwxz.p

[11] B.P. Baillargeon and S.S. Vel. Active vibration suppression of sandwich beams using piezoelectric shear actuators: Experiments and numerical simulations. *Journal of Intelligent Material Systems and Structures*, 16(6):517–530, 2005.

[12] G.J. Balas. *Robust control of flexible structures, theory and experiments*. PhD thesis, California Institute of Technology, CA. USA, 1990.

[13] G.J. Balas. Flight control law design: An industry perspective. *European Journal of Control*, 9(2-3):207–226, 2003.

[14] G.J. Balas and J.C. Doyle. Robustness and performance trade-offs in control design for flexible structures. *IEEE Transactions on Control System Technology*, 2:352–361, December 1994.

[15] M.J. Balas. Active control of flexible systems. *Journal of Optimization Theory and Applications*, 25(3):415–436, 1978.

[16] M.J. Balas. Trends in large space structure control theory: fondest hopes, wildest dreams. *IEEE Transactions on Automatic Control*, 27(3):522–535, 1982.

[17] M.J. Balas. Stable feedback control of linear distributed parameter systems: time and frequency domain conditions. *Journal of Mathematical Analysis and Applications*, 225:144–167, 1998.

[18] H.F. Bauer. Fluid oscillations in the containers of a space vehicle and their influence upon stability. Technical report, NASA - George C. Marshall Space Flight Center, Huntsville, AL. USA, 1964.

[19] H.F. Bauer and W. Eidel. Free oscillations and response of a viscous liquid in a rigid circular cylindrical tank. *Journal of Aerospace Science and Technology*, 3:495–512, 1999.

[20] H.F. Bauer and W. Eidel. Frictionless liquid sloshing in circular cylindrical container configurations. *Journal of Aerospace Science and Technology*, 3(5):301–311, 1999.

[21] H.F. Bauer and K. Komatsu. Coupled frequencies of a frictionless liquid in a circular cylindrical tank with an elastic partial surface cover. *Journal of Sound and Vibration*, 230(5):1147–1163, 2000.

[22] H.F. Bauer, J. Villanueva, and S.S. Chang. Analytical mechanical model for the description of the sloshing motion. Technical report, NASA - George C. Marshall Space Flight Center, Huntsville, AL. USA, 1966.

[23] J. Becker and W.G. Luber. Comparison of piezoelectric systems and aerodynamic systems for aircraft vibration alleviation. In *Smart Structures and Materials*, pages 9–18, San Diego, CA. USA, March 1998.

[24] T.B. Benjamin and F. Ursell. The stability of the plane free surface of a liquid in vertical periodic motion. *Royal Society of London. Series A, Mathematical and Physical Sciences*, 225:505–515, 1954.

[25] A. Bermúdez, R. Rodríguez, and D. Santamarina. Finite element method computation of sloshing modes in containers with elastic baffle plates. *International Journal for Numerical Methods in Engineering*, 53:447–467, 2003.

[26] C.W. Bert and V. Birman. Effects of stress and electric field on the coefficients of piezoelectric materials: One-dimensional formulation. *Mechanics Research Communications*, 25(2):165–169, 1998.

[27] C.W. Bert and V. Birman. Stress dependency of the thermoelastic and piezoelectric coefficients, analysis and design issues for modern aerospace vehicles. In *Proceedings of the ASME International mechanical engineering congress and exposition*, pages 265–269, Dallas, TX. USA, Nov. 1997.

[28] R.B. Bhat. Natural frequencies of rectangular plates using characteristic orthogonal polynomials in Rayleigh-Ritz method. *Journal of Sound and Vibration*, 102:493–499, 1985.

[29] B. Bhikkaji, S.O.R. Moheimani, and I.R. Petersen. Multivariable integral control of resonant structures. In *Proceedings of the 47th IEEE Conference on Decision and Control*, pages 3743–3748, Cancun, Mexico, December 2008.

[30] R.D. Blevins. *Formulas for natural frequency and mode shape*. Krieger publishing company, Florida, 1995.

[31] S. Boyd, L. El Ghaoui, E. Feron, and V. Balakrishnan. Linear matrix inequalities in systems and control theory. In *SIAM Studies in Applied Mathematics*, Philadelphia, PA. USA, 1994.

[32] H. Brezis. *Analyze Fonctionnelle: Thèorie et applications*. Collection Sciences Sup, Dunod, 2005.

[33] Brüel and Kjaer. *Brüel & Kjaer catalog*. http://www.bksv.fr/.

[34] B. Budiansky. Sloshing of liquids in circular canals and spherical tanks. Technical report, Lockheed Aircraft Corporation - missile system division, Sunnyvale, CA. USA, 1958.

[35] J.V. Burke, D. Henrion, A.S. Lewis, and M.L. Overton. HIFOO-a Matlab package for fixed-order controller design and h_∞ optimization. In *Proceedings of the 5th IFAC Symposium on Robust Control Design*, Toulouse, France, July 2006.

[36] G.F. Carrier and C.E. Pearson. *Partial differential equations*. Academic Press, San Diego, 1988.

[37] A. Cavallo, G. De Maria, C. Natale, and S. Pirozzi. Robust control of flexible structures with stable band-pass controllers. *Automatica*, 44:1251–1260, 2008.

[38] M. Chilali and P. Gahinet. H_∞ design with pole placement constraints, an LMI approach. *IEEE Transactions on Automatic Control*, 41(3):358–367, 1996.

[39] M. Chilali, P. Gahinet, and P. Apkarian. Robust pole placement in LMI regions. In *Proceedings of the 36th IEEE Conference on Decision and Control*, pages 1291–1296, San Diego, CA. USA, December 1997.

[40] A. Chouaki. *Recalage des modèles dynamiques de structures avec amortissement*. PhD thesis, ENS Cachan, 1997.

[41] S.-K. Chung, J.-H. Lee, J.-S. Ko, and M.-J. Youn. A robust speed control of brushless direct drive motor using integral variable structure control with sliding mode observer. *Industry Applications Society Annual Meeting and IEEE Conference Record of the 1994*, 1:393–400, 1994.

[42] E. Crépeau and C. Prieur. Control of a clamped-free beam by a piezoelectric actuator. *ESAIM: Control, Optimization and Calculus of Variations*, 12:545–563, 2006.

[43] G. Deaconu. Identification/commade aile d'avion. Stage LAAS-CNRS, Toulouse, 2010.

[44] M.A. Demetriou. A numerical algorithm for the optimal placement of actuators and sensors for flexible structures. In *Proceedings of the American Control Conference*, Chicago, IL. USA, June 2000.

[45] K.K. Denoyer and M.K. Kwak. Dynamic modeling and vibration suppression of a swelling structure utilizing piezoelectric sensors and actuators. *Journal of Sound and Vibration*, 189(1):13–31, 1996.

[46] J.J. Deyst. Effects of structural flexibility on entry vehicle control systems. Technical Report NASA SP-8098, Nasa, Space Vehicle Design Criteria, June 1972.

[47] E.K. Dimitriadis, C.R. Fuller, and C.A. Rogers. Piezoelectric actuators for distributed vibration excitation of thin plates. *Journal of Vibration and Acoustics*, 113(1):100–107, 1991.

[48] F.T. Dodge. The new "dynamic behavior of liquids in moving containers". Technical report, Southwest Research Institute, San Antonio, TX. USA, 2000.

[49] F.T. Dodge, D.D. Kana, and H.N. Abramson. Liquid surface oscillations in longitudinally excited rigid cylindrical containers. *AIAA Journal*, 3(4):685–695, 1965.

[50] R.C. Dorf. *The engineering handbook*. CRC Press, 1996.

[51] J.C. Doyle, K. Glover, P.P. Khargonekar, and B.A. Francis. State-space solutions to standard H_2 and H_∞ control problems. *IEEE Transactions on Automatic Control*, 34(8):831–847, 1989.

[52] F. Fahroo and Y. Wang. Optimal location of piezoceramic actuators for vibration suppression of a flexible structure. In *Proceedings of the 36th Conference on Decision and Control*, San Diego, CA. USA, December 1997.

[53] A.J. Fleming and S.O.R. Moheimani. Optimal impedance design for piezoelectric vibration control. In *Proceedings of the 43rd IEEE Conference on Decision and Control*, pages 2596–2601, Atlantis, Bahamas, December 2004.

[54] J.B. Frandsen. Sloshing motion in excited tanks. *Journal of Computational Physics*, 196:53–87, 2004.

[55] P. Gahinet and P. Apkarian. A linear matrix inequality approach to H_∞ control. *International Journal of Robust and Nonlinear Control*, 4:421–448, 1994.

[56] M. Géradin and D. Rixen. *Mechanical Vibrations: theory and application to structural dynamics*. Masson, 1994.

[57] G.C. Godwin, S.F. Graebe, and M.E. Salgado. *Control system design*. Prentice Hall, 2001.

[58] D.T. Greenwood. *Advanced dynamics*. Cambridge University Press, 2003.

[59] D.-W. Gu, P.H. Petkov, and M.M. Konstantinov. *Robust control design with Matlab*. Springer, 2005.

[60] S. Gumussoy, D. Henrion, M. Millstone, and M.L. Overton. Multiobjective robust control with HIFOO 2.0. In *Proceedings of the 6th IFAC Symposium on Robust Control Design*, Haifa, Israel, June 2009.

[61] A. Hac and L. Liu. Sensor and actuator location in motion control of flexible structures. *Journal of Sound and Vibration*, 167:239–261, 1993.

[62] D. Halim and S.O.R. Moheimani. Spatial resonant control of flexible structures - application to a piezoelectric laminate beam. *IEEE Transactions on Control System Technology*, 9(1):37–53, 2001.

[63] D. Halim and S.O.R. Moheimani. An optimization approach to optimal placement of collocated piezoelectric actuators and sensors on a thin plate. *Mechatronics: The Science of Intelligent Machines*, 13:27–47, 2003.

[64] P. Hebrard and A. Henrot. A spillover phenomenon in the optimal location of actuators. *SIAM Journal on Control and Optimization*, 44(1):349–366, 2005.

[65] Q. Hu and G. Ma. Variable structure control and active vibration suppression of flexible spacecraft during attitude maneuver. *Journal of Aerospace Science and Technology*, 9(4):307–317, 2005.

[66] J.K. Hwang, C.-H. Choi, C.K. Song, and J.M. Lee. Robust LQG control of an all-clamped thin plate with piezoelectric actuators/sensors. *IEEE/ASME Transactions on Mechatronics*, 2(3):205–212, 1997.

[67] R.A. Ibrahim. *Liquid sloshing dynamics*. Cambridge University press, 2005.

[68] R.E. Kalman. A new approach to linear filtering and prediction problems. *Transactions of ASME - Journal of Basic Engineering*, 82(D):35–45, 1960.

[69] I.N. Kar, T. Miyakura, and K. Seto. Bending and torsional vibration control of a flexible plate structure using H_∞-based robust control law. *IEEE Transactions on Control System Technology*, 8:545–552, 2000.

[70] S.A. Karamanos, S. Papaspyrou, and D. Valougeorgis. Sloshing effects in half-full horizontal cylindrical vessels under longitudinal excitation. *Journal of Applied Mechanics*, 71:255–265, 2004.

[71] E.M. Kervin. Damping of flexural waves by a constrained viscoelastic layer. *Journal of Acoustical Society of America*, 31(7):952–962, 1959.

[72] R.S. Khandelwal and N.C. Nigam. A mechanical model for liquid sloshing in a rectangular container. *Journal of the Institution of Engineers*, 69:152–156, 1989.

[73] C.S. Kim, P.G. Young, and S.M. Dickinson. On the flexural vibration of rectangular plates approached by using simple polynomials in the Rayleigh-Ritz method. *Journal of Sound and Vibration*, 143:379–394, 1990.

[74] S.J. Kim and J.D. Jones. Influence of piezo-actuator thickness on the active vibration control of a cantilever beam. *Journal of Intelligent Material Systems and Structures*, 6:610–623, 1995.

[75] C. Kittel. *Introduction to solid state physics*. John Wiley & sons, 1996.

[76] L. Korson, W. Drost-Hansen, and F.J. Millero. Viscosity of water at various temperatures. *Journal of Physical Chemistry*, 73(1):34–39, 1969.

[77] B.C. Kuo. *Automatic control systems, second edition*. Prentice-Hall, N.J., 1967.

[78] Sir H. Lamb. *Hydrodynamics*. Cambridge Mathematical Library, 1995.

[79] I. Lasiecka and A. Tuffaha. Boundary feedback control in fluid-structure interactions. In *Proceedings of the 47th IEEE Conference on Decision and Control*, pages 203–208, Cancun, Mexico, December 2008.

[80] A.W. Leissa. The free vibration of rectangular plates. *Journal of Sound and Vibration*, 31:257–293, 1973.

[81] S. Leleu. *Amortissement actif des vibrations d'une structure flexible de type plaque à l'aide de transducteurs poézoélectriques*. PhD thesis, ENS Cachan, 2002.

[82] K.B. Lim, P.G. Maghami, and S.M. Joshi. Comparison of controller design for an experimental flexible structure. *IEEE Control Systems Magazine*, 12:108–118, 1992.

[83] G.R. Liu. *Meshfree methods: moving beyond the finite element method, second edition*. C.R.C. Press, 2010.

[84] D.G. Luenberger. Observing the state of a linear system. *IEEE Transactions on Military Electronics*, 8(2):74–80, 1964.

[85] U. Mackenroth. *Robust control studies: theory and case studies*. Springer, 2004.

[86] B. Madeleine. *Détermination d'un modèle dynamique pertinent pour la commande: de la réduction à la construction*. PhD thesis, ISAE Supaero, Toulouse, 1998.

[87] F.J.R. Martinez. Développement d'un modèle pour l'estimation des amplitudes des vibrations sur des structures intelligentes. Technical report, ISAE - ENSICA, 2008.

[88] F. Matsuno, M. Hatayama, H. Senda, T. Ishibe, and Y. Sakawa. Modeling and control of a flexible solar array paddle as a clamped-free-free-free rectangular plate. *Automatica*, 32:49–58, 1995.

[89] F. Matsuno, T. Ohno, and Y.V. Orlov. Proportional derivative and strain (dps) boundary feedback control of a flexile space structure with a closed-loop chain mechanism. *Automatica*, 38(7):1201–1211, 2002.

[90] P. McIver. Sloshing frequencies for cylindrical and spherical containers filled to an arbitrary depth. *Journal of Fluid Mechanics*, 201:243–257, 1989.

[91] P. McIver and M. McIver. Sloshing frequencies of longitudinal mode for a liquid container in a trough. *Journal of Fluid Mechanics*, 252:525–541, 1993.

[92] K.F. Merten and B.H. Stephenson. Some dynamic effects of fuel motion in simplified model tip tank on suddenly excited bending oscillations. Technical report, NASA - Langley Aeronautical Laboratory, Langley Field, VA. USA, 1952.

[93] L.M. Milne-Thomson. *Theoretical hydrodynamics*. Dover publications, INC., 5 edition, 1968.

[94] S.O.R. Moheimani and A.J. Fleming. *Piezoelectric transducers for vibration control and damping*. Advances in industrial control. Springer, 1968.

[95] S.O.R. Moheimani, D. Halim, and A.J. Fleming. *Spatial control of vibrations: theory and experiments*, volume 10 of *A*. World Scientific, 2003.

[96] S.O.R. Moheimani and W.P. Heath. Model correction for a class of spatio-temporal systems. *Automatica*, 38(1):147–155, 2002.

[97] H. Morand and R. Ohayon. *Fluid structure interactions*. John Wiley & sons, 1995.

[98] S. Mottelet. Controllability and stabilization of liquid vibration in a container during transportation. In *Proceedings of the 39th IEEE Conference on Decision and Control*, pages 4641–4646, Sydney, NSW. Australia, December 2000.

[99] A.G.O. Mutambara. *Design and analysis of the control systems*. CRC Press, 1999.

[100] J.F. Nye. *Physical properties of crystals: their representation by tensors and matrices*. Clarendon press Oxford, 1995.

[101] K. Ogata. *Modern control engineering, fourth edition*. Prentice Hall, New Jersey, 2002.

[102] H. Ohanessian and P. Gonnard. Influence d'une polarisation de réorientation sur l'anisotropie des céramiques piézoélectriques et leur stabilité. *Revue Physique Appliquée*, 22:47–53, 1987.

[103] R. Ohayon. *Fluid - structure interaction problems*, volume 2. John Wiley & sons, encyclopedia of computational mechanics edition, 2004.

[104] H. Özbay. *Introduction to feedback control theory*. CRC Press, 2000.

[105] N.C. Pal, S.K. Bhattacharyya, and P.K. Sinha. Experimental investigation of slosh dynamics of liquid-filled containers. *Journal of Experimental Mechanics*, 41(1):63–69, 2001.

[106] J.P. Pérez, R. Carles, and R.Fleckinger. *Electromagnétisme*. Masson, 1996.

[107] I.R. Petersen and H.R. Pota. Minimax LQG optimal control of a flexible beam. *Control Engineering Practice*, 11:1273–1287, 2003.

[108] V. Pommier-Budinger, M. Budinger, P. Lever, J. Richelot, and J. Bordeneuve-Guibé. FEM design of a piezoelectric active control structure. Application to an aircraft wing model. In *Proceedings of the International Conference on Noise and Vibration Engineering*, Leuven, Belgium, September 2004.

[109] V. Pommier-Budinger, Y. Janat, D. Nelson-Gruel, P. Lanusse, and A. Oustaloup. Fractional robust control with iso-damping property. In *Proceedings of the American Control Conference*, pages 4954–4959, Seattle, WA. USA, June 2008.

[110] V. Pommier-Budinger, J. Richelot, and J. Bordeneuve-Guibé. Active control of a structure with sloshing phenomena. In *Proceedings of the IFAC Conference on Mechatronic Systems*, Heidelberg, Germany, 2006.

[111] R.W. Pratt. *Flight control systems: practical issues in design and implementation.* TJ International, Padstow, Cornwall, 2000.

[112] A. V. Rao. *Dynamics of particles and rigid bodies, a systematic approach.* Cambridge University Press, 2006.

[113] H. Reinbard. *Equations aux dérivées partielles: fondements et applications.* Dunod Université, Paris, 1987.

[114] J. Richelot. *Contrôle actif des structures flexibles par commande prédictive généralisée.* PhD thesis, ISAE - ENSICA, 2005.

[115] B. Robu. Contrôle actif du ballottement dans une aile d'avion. Mémoire de stage, Master 2, LAAS - CNRS, Toulouse, 2007.

[116] B. Robu, L. Baudouin, and C. Prieur. A controlled distributed parameter model for a fluid-flexible structure system: numerical simulations and experiment validations. In *Proceedings of the 48th IEEE Conference on Decision and Control and 28th Chinese Control Conference*, pages 5532–5537, Shanghai, P.R. China, December 2009.

[117] B. Robu, L. Baudouin, C. Prieur, and D. Arzelier. Simultaneous H_∞ vibration control of a fluid/plate system via reduced-order controller. *Conditionally accepted in IEEE Transactions on Control Systems Technology*, 2010.

[118] B. Robu, V. Budinger, L. Baudouin, C. Prieur, and D. Arzelier. Simultaneous H_∞ vibration control of a fluid/plate system via reduced-order controller. In

Proceedings of the 49th IEEE Conference on Decision and Control, Atlanta, GE. USA, December 2010.

[119] C. Roos. Generation of flexible aircraft LFT models for robustness analysis. In *Proceedings of the 6th IFAC Symposium on Robust Control Design*, pages 349–354, Haifa, Israel, June 2009.

[120] J. Roskam. *Airplane flight dynamics and automatic flight controls*, volume 1. Design, Analysis and Research Corporation, 2003.

[121] S. Rubin. Improved component-mode representation for structural dynamic analysis. *AIAA Journal*, 13(8):995–1006, 1975.

[122] I.L. Ryhming. *Dynamique des fluides*. Presses polytechniques et universitaires romandes, Lausanne, 1991.

[123] J.-S. Schotté and R. Ohayon. Various modeling levels to represent internal liquid behavior in the vibration analysis of complex structures. *Journal of Computation Methods Applied Mechanics Engineering*, 198:1913–1925, 2009.

[124] A.A. Schy. A theoretical analysis of the effects of fuel motion on airplane dynamics. Technical report, NASA - Langley Aeronautical Laboratory, Langley Field, VA. USA, 1952.

[125] K. Seto. A structural control method of the vibration of flexible buildings in response to large earthquakes and strong winds. In *Proceedings of the 35th Conference on Decision and Control*, Kobe, Japan, December 1996.

[126] K. Seto and I.N. Kar. A comparative study on H-infinity based vibration controller of flexible structure system. In *Proceedings of the American Control Conference*, Chicago, IL. USA, June 2000.

[127] W.C. Siebert. *Circuits, Signals, and Systems*. The MIT Press, 1998.

[128] A. Sinha. *Linear systems, optimal and robust control*. CRC Press, 2007.

[129] R.F. Stengel. *Flight dynamics*. Princeton University Press, 2004.

[130] D.G. Stephens and H.W. Leonard. The coupled dynamic response of a tank partially filled with liquid and undergoing free and forced planar oscillations. Technical report, NASA - Langley Research Center, Hampton, VA. USA, 1963.

[131] S. Tarbouriech, C. Prieur, and J.M. Gomes da Silva Jr. An anti-windup strategy for a flexible cantilever beam. In *Proceedings of the IFAC World Congress on Automatic Control*, Praha, Czech Republic, 2005.

[132] T. Terasawa, C. Sakai, H. Ohmori, and A. Sano. Adaptive identification of MR damper for vibration control. In *Proceedings of the 43rd IEEE Conference on Decision and Control*, pages 2297–2303, Atlantis, Bahamas, December 2004.

[133] S. Tliba. *Contrôle actif des vibrations dans des structures mécaniques minces instrumentées de transducteurs piézoélectriques*. PhD thesis, ENS Cachan, 2004.

[134] S. Tliba and H. Abou-Kandil. H_∞ control design for active vibration damping of flexible structure using piezoelectric transducers. In *Proceedings of the 4th IFAC Symposium on Robust Control Design*, Milan, Italy, June 2003.

[135] S. Tliba, H. Abou-Kandil, and C. Prieur. Active vibration damping of a smart flexible structure using piezoelectric transducers: H_∞ design and experimental results. In *IFAC World Congress on Automatic Control*, Praha, Czech Republic, July 2005.

[136] E.E. Ungar. Loss factor of viscoelastically damped beam structures. *Journal of Acoustical Society of America*, 34(4):1082–1089, 1962.

[137] D. Voracek, E. Pendleton, E. Reichenbach, K. Griffin, and L. Welch. The active aeroelastic wing phase I flight research through January 2003. Technical Report NASA TM-210741, Nasa, Dryden Flight Research Center, Edwards, CA. USA, April 2003.

[138] J.P.B. Vreeburg and D.J. Chato. Models for liquid impact onboard Sloshsat FLEVO. In *Proceedings of the AIAA Space Conference*, Long Beach, CA. USA, 2000.

[139] L.C. Westphal. *Handbook of control system engineering, 2nd edition*. Kluwer Academic Publisher, 2001.

[140] K. Yamada, H. Matsuhisa, H. Utsuno, and J.G. Park. Hybrid vibration suppression of multiple vibration modes of flexible structures using piezoelectric elements and analog circuit. *Journal of Environment and Engineering*, 3(2):424–435, 2008.

[141] S.M. Yang and Y.J. Lee. Vibration suppression with optimal sensor/actuator location and feedback gain. *Journal of Smart Materials and Structures*, 2(4):232–247, 1993.

[142] D. Young. Vibration of the rectangular plate by Ritz method. *Journal of Applied Mechanics*, 17:448–453, 1950.

[143] L.A. Zadeh and C.A. Desoer. *Linear system theory, the state space approach.* McGraw Hill Book Company, New York, 1963.

[144] J. Zhang, L. He, E. Wang, and R. Gao. Active vibration control of flexible structures using piezoelectric materials. In *Proceedings of the International Conference on Advanced Computer Control*, pages 540–545, Shenyang, P.R. China, January 2009.

[145] K. Zhou and J.C. Doyle. *Essentials of robust control.* Prentice Hall, N.J., 1999.

[146] K. Zhou, J.C. Doyle, and K. Glover. *Robust and optimal control.* Prentice Hall, N.J., 1996.

[147] O.C. Zienkiewicz. *The Finite Element Method.* McGraw Hill Book Company, London, 1977.